Me 144

ACTA POLYTECHNICA SCANDINAVICA

MECHANICAL ENGINEERING SERIES No. 144

Simulation of the Flow Past a Long-Range Artillery Projectile

PETRI KAURINKOSKI

Helsinki University of Technology
Department of Mechanical Engineering
Laboratory of Aerodynamics
FIN-02015 HUT
Finland

Dissertation for the degree of Doctor of Science in Technology to be presented with due permission of the Department of Mechanical Engineering, for public examination and debate in Auditorium K216 at Helsinki University of Technology (Espoo, Finland) on the 2nd of June, 2000, at 12 noon.

ESPOO 2000

Kaurinkoski, Petri M., **Simulation of the Flow Past a Long-Range Artillery Projectile**. Acta Polytechnica Scandinavica, Mechanical Engineering Series No. 144, Espoo 2000, 114 pages. Published by the Finnish Academies of Technology, ISBN 951–666–536–5, ISSN 0001–687X, UDC 533.6.013.

Keywords: Projectile Aerodynamics, Base Bleed, Computational Fluid Dynamics, Thermodynamics, Combustion

Abstract

In this work, an eddy breakup model for chemical reactions is implemented to an existing multi-block Navier–Stokes solver, which is then used to solve the flow past a supersonic long-range base-bleed projectile. The new scheme is validated by simulating an axisymmetric bluff-body stabilized flame, which has been measured in a wind tunnel and simulated numerically by other work groups.

Comparison of the numerical results for the projectile shows the importance of the chemistry modelling for accurate numerical predictions. The final combustion of the fuel-rich propellant simulated in this work makes a dramatic difference in the predicted aerodynamic drag of the projectile. The drag reduction due to base bleed is more than doubled when the chemical reactions are accounted for, and the drag prediction based on the simulations including chemical reactions is excellent.

Foreword

This thesis is the result of several years of work, sometimes frustrating work, at the Laboratory of Aerodynamics. On several occasions it seemed like this task would never be completed, but fortunately the work was never aborted, only suspended for various reasons.

I want to thank my advisor Professor Seppo Laine for providing me with this opportunity to complete my thesis. I also want to thank him for his critical comments on this work.

There are several other persons who have directly or indirectly supported this work. My colleagues, especially Antti Hellsten, Patrik Rautaheimo and Esa Salminen as well as Professors Timo Siikonen and Raimo Häkkinen, have all helped me in their ways to complete this work for which I am grateful.

I would especially like to thank Professors Eero-Matti Salonen and Kullervo Kuusela for their long-term support of my studies and their invaluable advice on several occasions.

This research project has been mainly funded by MATINE, the Scientific Advisory Board for Defence, and PvMatLE, the Defence Materiel Establishment of the Finnish Defence Forces. Their support for this research is gratefully acknowledged.

Last but not least, I want to thank my wife Mirja and daughter Susanna for their patience and support.

Helsinki, April 6, 2000

Petri Kaurinkoski

Contents

Nomenclature

A, B, C	Jacobian matrices ($\partial \hat{F}/\partial U$ in i, j and k -directions)
A, B, C, D	coefficients in the curve-fit equation for C_p in Eq. (2.84)
C_D	drag coefficient, $D/(\rho_\infty V_\infty^2 S/2)$
C_p	pressure coefficient, $(p - p_\infty)/(\rho_\infty V_\infty^2/2)$; also molar heat capacity
$CD_{k\omega}$	cross-diffusion term in the $\rho\omega$-equation
D	drag force [N]; diameter of the bluff body [m]; diameter of the projectile [m]; Jacobian matrix of the source term Q, $(\partial Q/\partial U)$
$\mathcal{D}_{i\mathrm{m}}$	multicomponent diffusion coefficient of species i [m^2/s]
E	specific total internal energy [J/kg]
F, G, H	flux vectors in x, y and z-directions
F_1, F_2, F_3, F_4	functions in the $k - \omega$ model
$\vec{F}$	flux vector in a curvilinear coordinate system
$\hat{F}$	flux in a given direction in space
H	specific total enthalpy [J/kg]
I	identity matrix
Kn	Knudsen number
L	characteristic length scale of the flow case [m]
$\mathcal{M}$	molecular weight [g/mol]
Ma	Mach number
N	number of particles
N_i	number of particles of species i; also a shape function
Pr	Prandtl number
Q	source term
$\mathcal{R}$	universal gas constant, 8.314 J/(mol K)
R	residual; eigenvector matrix; specific gas constant, $\mathcal{R}/\mathcal{M}$
Re	Reynolds number, $\rho_\infty V_\infty L/\mu_\infty$
S	cell face area [m^2]; reference area [m^2]
S_x, S_y, S_z	cell face area components in x, y and z-directions [m^2]
S_{ij}	strain-rate tensor [1/s]
S_R	non-dimensional coefficient related to surface roughness
T	temperature [K]; time-scale; also a rotation matrix
Tu	turbulence level, $\sqrt{\overline{u_i'' u_i''}/3V^2} = \sqrt{2k/3V^2}$
U	vector of the conservative variables
V	cell volume [m^3]; velocity [m/s]
W	weight function

X	mole fraction N_i/N
a_1	constant coefficient in Bradshaw's assumption in Eq. (2.68)
c_f	local skin friction coefficient, $\tau_\mathrm{w}/(\rho_\infty V_\infty^2/2)$
c_p	specific heat capacity at constant pressure $(\partial h/\partial T)_p$ [J/(kg K)]
c_v	specific heat capacity at constant density $(\partial e/\partial T)_\rho$ [J/(kg K)]
c_1, c_2, c_μ	coefficients involved with the $k-\epsilon$ model
d	cell thickness [m]; distance to the nearest wall point [m]; diameter of the fuel jet [m]
e	internal energy per unit mass, i.e. specific internal energy [J/kg]
h	specific enthalpy [J/kg]
$\vec{i}, \vec{j}, \vec{k}$	unit vectors in Cartesian coordinate system
k	thermal conductivity [W/(K m)]; kinetic energy of turbulence, $\frac{1}{2}\overline{u_i'' u_i''}$ [(m/s)^2]; also specific reaction rate
$\dot{m}$	mass flow rate [kg/s]
$\dot{m}_A$	mass flow rate per unit area [kg/(m^{2}s)]
$\vec{n}$	cell face unit normal vector
p	static pressure [N/m^2]
q	heat flux [W/m^2]
r	distance from the axis of rotation [m]; stoichiometric coefficient
t	time [s]
u, v, w	velocity components in x, y and z-directions [m/s]
u_τ	friction velocity $\sqrt{\tau_\mathrm{w}/\rho_\mathrm{w}}$ [m/s]
x, y, z	Cartesian coordinates [m]
y_n	normal distance from the surface [m]
y^+	non-dimensional normal distance from the surface $y_\mathrm{n} u_\tau/\nu$
Γ, Γ_2	arguments to the blending functions in the $k-\omega$ model
$\vec{\mathbf{\Omega}}$	angular velocity [rad/s]
Ω_{ij}	vorticity tensor [1/s]
α	characteristic variable, angle of attack [°]
β, β^*	model constants in the $k-\omega$ model
γ	ratio of specific heats c_p/c_v
δ_{ij}	Kronecker's delta
ϵ,ε	dissipation of kinetic energy of turbulence, see Eq. (2.53) [m^2/s^3]
κ	constant in the $\rho\omega$ production term
λ	mean free path of molecules [m]; eigenvalue
ρ	density [kg/m^3]
μ	dynamic viscosity [kg/(m s)]
ν	kinematic viscosity μ/ρ [m^2/s]
ξ	conservative scalar
ω	specific dissipation rate of kinetic energy of turbulence, $\varepsilon/(\beta^* k)$ [1/s]
τ	normal or shear stress [N/m^2]; also pseudo-time [s]
ϕ	mass fraction of a species; also a general scalar variable
ψ	length-scale variable for the turbulence equation, i.e. either ϵ or ω
$\sigma_k, \sigma_\epsilon, \sigma_\omega, \sigma_\phi$	Schmidt numbers for k, ϵ, ω and ϕ, respectively

Subscripts

L,T	laminar and turbulent conditions, respectively
b	base-region value
burn	burning surface value
i	index of the gas species
i, j, k	grid coordinate directions
max	maximum value
min	minimum value
st	stoichiometric conditions
v	viscous
w	wall
∞	free-stream value
1,2	first and second cell above the surface

Superscripts

e	explicit change
k	index of inner iteration cycle
(k)	index of the characteristic variable, eigenvector or eigenvalue
mol	molar value
n	index of time-level
l, r	left and right side of the cell face, respectively
$+$	value scaled with wall conditions

1 Introduction

The development of computer technology during the 1980's and 1990's has brought a radical change in the way new products are developed nowadays. Numerical simulations and computer animations are utilized as an integral part of the development cycle, as the desktop computer power seems to increase without end. Also, techniques to utilize clusters of workstations as local massively parallel computers enchance the capacity available at most research institutes. So far, however, all the computing power available has been immediately harnessed to solve more and more complex problems.

The on-going development towards ever increasing complexity in numerical modelling of fluid flow actually started before any computers existed. The first numerical models were intended for manual calculation of boundary layers and straight wings, the latter being based on the lifting line theory and the potential flow assumption. From that point on, the physical realism and the geometrical complexity of numerical simulations have increased, little by little, to reach the current state of the art. On a conceptual level, the product of the complexity of the physical model and the size of the numerical model is a measure for the requirement of computational resources for a given problem. With given computing resources, a balance has to be found between the size of the model and the physical details included in the computation.

This work is focused on numerical simulations of a long-range base-bleed projectile. The whole process of investigating a real-life situation with numerical simulations is described, and the different assumptions made to obtain the numerical model are reviewed. Since the physical model itself is quite complicated, the complexity of the computational domain is reduced by studying only axisymmetric flow cases, although the method is by no means limited to that.

Over the past decades, flows past artillery shells or fin-stabilized projectiles have been studied extensively both numerically [1–7] and experimentally [8, 9]. Most of the work has concentrated on the basic fluid dynamic phenomena occurring near the base of a blunt-based object. Base bleed as a method of reducing aerodynamic drag has been discussed in several papers [10, 11], but little work has concentrated on the effects of chemical reactions in conjunction with base bleed [12, 13].

The increase in the available computer capacity is seen in the employed modelling techniques. In the early work, the simulations were for axisymmetric flow situations, and turbulence was modelled with the algebraic Baldwin–Lomax model [1] or the two-equation $k - \epsilon$ model [2]. Later, 3-D simulations with non-zero angle of attack [3] and simulations of complex geometries [4–7] as well as chemically

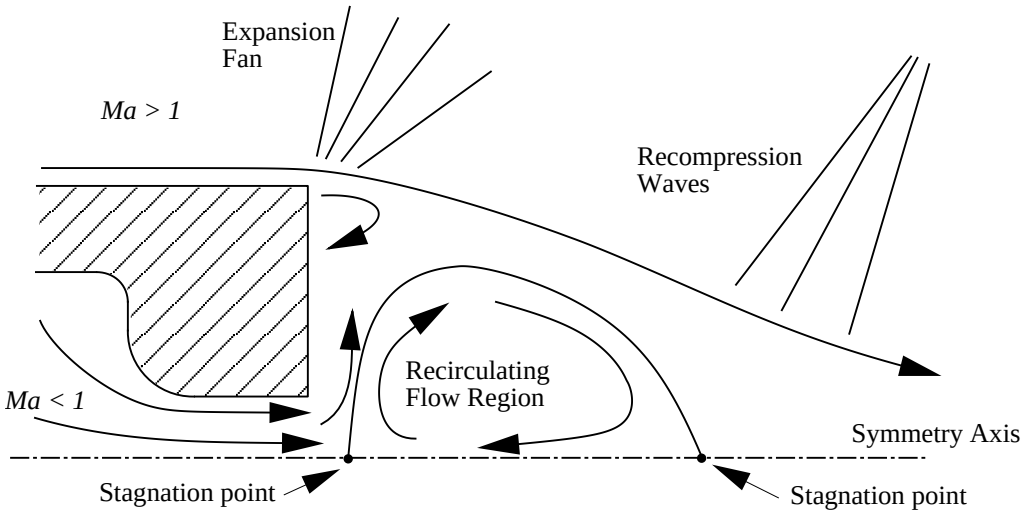

Fig. 1.1: The basic structure of the flow field right behind the base of a base-bleed projectile at a low base-bleed rate.

reacting flow fields [6, 7] could be carried out. Gibeling and Buggeln [12] as well as Nietubicz and Gibeling [13] simulated the afterbody of base-bleed projectiles with chemical reactions in a semi-parabolic manner. In most of these studies, the Baldwin–Lomax model was used exclusively, and in none of them was the projectile rotating.

The idea behind base bleed is to modify the base pressure, and thus the base pressure drag, of a supersonic projectile by injecting small amounts of gas into the flow field behind the base of the projectile. The originally large recirculation zone is split into two halves; one recirculation region remains at the symmetry axis, and the other one right behind the base corner [9]. This situation is illustrated in Figure 1.1. As the mass flow rate is increased, the recirculation zone at the axis is pushed further out, and the other one at the base corner becomes larger. The main flow separates from the base corner, and the wake turns with the expanding flow, and eventually compresses back to be aligned with the axis of symmetry. If the mass flow rate is further increased, the recirculation region near the axis disappears, and the base-bleed flow follows a straight path.

This research effort is a part of a long-term research campaign to develop a flexible flow solver, FINFLO [14–19]. The new feature developed in this work is the ability to simulate reactive flows, and it is a follow-up to several years of work on simulating fin-stabilized projectiles [20, 21] and artillery shells [22].

The eddy breakup model (EBU) implemented in this work was first published by Magnussen [23], and it is based on Spalding's [24] earlier work. Later on, it has become very popular in simulation of turbulent premixed flows [25–28]. Details of the model and its implementation are presented in this work, and the implementation is validated with a case for which both experimental [29] and numerical [30] results exist. Finally, the flow past a long-range artillery projectile is simulated without base bleed, with base bleed, and with reactive base bleed. All of the simulations are carried out for both a rotating and a non-rotating projectile.

Besides enlarging the capability of the employed solver, the simulations in this work demonstrate the dramatic effect the reaction model has on the accuracy of the drag predictions of a long-range base-bleed projectile. So far, the importance of the reactions has not been widely known. Also, the issue of determining the base-bleed inlet conditions is treated by extending the computational domain inside the unit, and thus solving the conditions at the base-bleed nozzle exit instead of specifying them. This allows for determining the effects of rotation on base bleed in a more realistic manner.

2 Modelling of a Reactive Flow Field

2.1 General Thoughts

In any simulation of fluid flow it is essential to identify the approximations associated with the selected models and numerical methods. The underlying physics should be understood in order to have a base knowledge of the phenomenon present in the flow field and to select appropriate modelling schemes for them. It is clear that any assumptions made while modelling the physics, or even before that, when defining the physical environment, will limit the range of applicability of the simulation method.

In this chapter, the procedure of simulating fluid flow is reviewed with emphasis on reactive flows. The various assumptions made are mentioned, and the limitations so introduced are also discussed. Although most of this text is written with a general perspective, some issues related to the present implementation in the flow solver employed in this work are also described in this chapter.

2.2 Basic Physics of Fluid Flow

2.2.1 Continuum Assumption

The common assumption made while simulating fluid flow is to assume the fluid to be a continuum, a continuous medium. This assumption is valid for most aerodynamic flows, since the mean free path λ of molecules in air at standard sea-level conditions is of the order of 0.7×10^{-7} m, which is several orders of magnitude smaller than any characteristic length L in most aerodynamics studies. The ratio of those lengths defines the Knudsen number $Kn = \lambda/L$, which determines whether the continuum assumption holds or not. The limit $Kn < 0.03$ can be used as an upper limit for the standard continuum assumption with no-slip surfaces [31].

2.2.2 Conservation Equations for Mass, Momentum and Energy

The physical modelling of fluid flow is based on a number of conservation equations. The conservation equation for mass, the continuity equation, is written using a tensor notation as

$$\frac{\partial}{\partial t}\rho + \frac{\partial}{\partial x_i}\left(\rho u_i\right) = 0 \tag{2.1}$$

where ρ is the density and u_i is the velocity in the x_i-direction. The conservation equations for momentum, the Navier–Stokes equations, are actually a form of Newton's second law, $\sum F = \mathrm{d}/\mathrm{d}t(mV)$, written for a fluid element travelling with the flow. Ignoring gravity and other body forces, the Navier–Stokes equations are

$$\frac{\partial}{\partial t}\left(\rho u_i\right) + \frac{\partial}{\partial x_j}\left(\rho u_i u_j\right) \;=\; -\frac{\partial}{\partial x_i}p + \frac{\partial}{\partial x_j}\tau_{ij} \tag{2.2}$$

where pressure is denoted with p, and τ is the viscous stress tensor. In these equations, the left-hand side represents the time rate of change of momentum of a fluid element, and the right-hand side is the force imposed on the fluid element. The stress tensor τ is symmetric, which follows from the requirement of finite angular acceleration of a fluid element [32].

The energy equation is again just a balance equation stating that the total energy is conserved, i.e.

$$\frac{\partial}{\partial t}\left(\rho E\right) + \frac{\partial}{\partial x_i}\left(\rho E\, u_i\right) = -\frac{\partial}{\partial x_i}\left(p\, u_i\right) + \frac{\partial}{\partial x_i}\left(u_j\tau_{ij} - q_i\right) \tag{2.3}$$

where ρE denotes the total internal energy per unit volume. Also, q_i represents the energy flux due to diffusion in the x_i-direction.

Eqs. (2.1)–(2.3) are the basic field equations governing the flow of a homogeneous fluid, and nowadays they are often all together called the Navier–Stokes equations. We should note here that, in the form presented above, we have neither assumed anything about the viscous stress tensor τ nor the heat flux q. For the stress tensor, a common assumption is to adopt the linear stress–strain relationship together with Stokes' assumption, and the expression for the viscous stress tensor is

$$\tau_{ij} = \mu\left[2S_{ij} - \frac{2}{3}\delta_{ij}\frac{\partial u_k}{\partial x_k}\right] \tag{2.4}$$

where S_{ij} is the strain-rate tensor

$$S_{ij} = \frac{1}{2}\left(\frac{\partial u_i}{\partial x_j} + \frac{\partial u_j}{\partial x_i}\right) \tag{2.5}$$

In Eq. (2.4), μ is the viscosity of the fluid, and δ_{ij} is Kronecker's delta. The heat flux is usually approximated with Fourier's gradient diffusion formula

$$q_i = -k\frac{\partial}{\partial x_i}T \tag{2.6}$$

where k is the thermal conductivity of the fluid. In the above, p, T, μ and k are assumed to be known functions of two state variables, e.g. specific internal energy

e and density ρ. The specific internal energy is also a state variable, i.e. formally $e = e(\rho, p) = e(p, T)$, and the connection between ρE and e is

$$\rho E = \rho e + \frac{1}{2}\rho u_i u_i \tag{2.7}$$

The majority of fluid flow problems studied in aerodynamics is governed by the equations given above. The expressions for p, T, μ and k in terms of ρ and e are not given here, since they involve modelling assumptions and are not fundamental in that sense.

If the fluid consists of several species, conservation equations must be written for all the components. Defining $\phi_i = \rho_i/\rho$ as the mass fraction of species i, we may write for each species

$$\begin{aligned} \frac{\partial}{\partial t}\rho_i + \frac{\partial}{\partial x_j}\left(\rho_i u_j\right) &= \\ \frac{\partial}{\partial t}\left(\rho\phi_i\right) + \frac{\partial}{\partial x_j}\left(\rho\phi_i u_j\right) &= \frac{\partial}{\partial x_j}\left(\rho\mathcal{D}_{i\mathrm{m}}\frac{\partial}{\partial x_j}\phi_i\right) + Q_i \end{aligned} \tag{2.8}$$

where $\mathcal{D}_{i\mathrm{m}}$ is the multicomponent diffusion coefficient of species i and Q_i denotes the production or destruction of species i due to chemical reactions. Since the total mass is the sum of the masses of the species, we may write for a mixture of n species

$$\sum_{i=1}^{n}\rho_i = \rho \tag{2.9}$$

or

$$\sum_{i=1}^{n}\phi_i = 1 \tag{2.10}$$

which can be used to eliminate the n:th species continuity equation. We might note here that the species continuity equation (2.8) has a diffusion term, which is not present in the equation for total mass. If the different species have different thermodynamic properties, the energy equation has to be completed with a term representing the diffusion of energy due to diffusion of mass

$$q_{\phi_j} = -\rho h_k \mathcal{D}_{k\mathrm{m}}\frac{\partial}{\partial x_j}\phi_k = -h_k\frac{\mu}{\sigma_{\phi_k}}\frac{\partial}{\partial x_j}\phi_k \tag{2.11}$$

where h_k is the specific enthalpy of species k, and $\sigma_{\phi_k} = \mu/(\rho\mathcal{D}_{k\mathrm{m}})$ is the Schmidt number of species k. The mass fractions ϕ_i introduced in Eq. (2.8) also have to be accounted for when formulating the thermodynamic relationships for T and p, as well as for μ and k.

2.2.3 Equations for Turbulent Flow

Although Eqs. (2.1)–(2.3) together with Eq. (2.8) are general and valid for all kinds of aerodynamic flows, they are not suitable for turbulent flows — unless, of course, direct numerical simulation is carried out. The reason is simply that many flows are turbulent in nature, which means they include unsteady details with very small time-scales. Therefore, for the simulation of turbulent flows, it is customary to express the flow variables as a sum of their time-averaged value and fluctuating value. The standard procedure leading to Reynolds-averaged Navier–Stokes equations for incompressible flows involves ordinary time-averaging as

$$u_i = \bar{u}_i + u_i' \qquad \bar{u}_i = \frac{1}{T}\int_t^{t+T} u_i(\tau)\mathrm{d}\tau \tag{2.12}$$

where the Reynolds-averaged value is denoted by an overbar. For compressible flows this treatment is cumbersome, since the equations contain several terms involving products of three decomposed variables. A better approach is to utilize density-weighted [33] averaging suggested by Favre. Introducing Favre-averages defined by

$$u_i = \tilde{u}_i + u_i'' \qquad \tilde{u}_i = \frac{1}{\bar{\rho}\,T}\int_t^{t+T} \rho(\tau)u_i(\tau)\mathrm{d}\tau \tag{2.13}$$

where the Favre-averaged value is denoted by a tilde. The advantage of the Favre-average is that the time-average of the product of density and any other variable is the product of the average density and the Favre-averaged variable. Therefore, the following equation holds

$$\overline{\rho u_i} = \bar{\rho}\bar{u}_i + \overline{\rho' u_i'} \;\; = \;\; \bar{\rho}\tilde{u}_i + \overline{\rho u_i''} = \bar{\rho}\tilde{u}_i \tag{2.14}$$

$$\tag{2.15}$$

In other words, the time-average of $\rho u_i''$ is identically zero. This follows from the definition of the Favre-average in Eq. (2.13). The employed decompositions are then

$$\rho = \bar{\rho}+\rho' \qquad p = \bar{p}+p' \qquad q_i = \bar{q}_i+q_i' \qquad u_i = \tilde{u}_i+u_i'' \qquad E = \tilde{E}+E'' \tag{2.16}$$

where, for example, $\tilde{u}_i$ and u_i'' are the Favre-average and fluctuating value of u_i, respectively. Replacing the variables with the above decompositions and taking a time-average of the equations, we arrive at equations resembling the original equations, but some extra terms have also been formed, since in a general case the average value of the product of two fluctuating values is not identically zero. The Favre-averaged Navier–Stokes equations [34] are

$$\frac{\partial}{\partial t}\bar{\rho} + \frac{\partial}{\partial x_i}\left(\bar{\rho}\tilde{u}_i\right) = 0 \tag{2.17}$$

$$\frac{\partial}{\partial t}\left(\bar{\rho}\tilde{u}_i\right) + \frac{\partial}{\partial x_j}\left(\bar{\rho}\tilde{u}_i\tilde{u}_j\right) = -\frac{\partial}{\partial x_i}\bar{p} + \frac{\partial}{\partial x_j}\left(\bar{\tau}_{ij} - \overline{\rho u_i'' u_j''}\right) \tag{2.18}$$

$$\frac{\partial}{\partial t}\left[\bar{\rho}\tilde{E} + \frac{1}{2}\overline{\rho u_i'' u_i''}\right] + \frac{\partial}{\partial x_j}\left[\left(\bar{\rho}\tilde{E} + \bar{p}\right)\tilde{u}_j + \tilde{u}_j\frac{1}{2}\overline{\rho u_i'' u_i''}\right] = \tag{2.19}$$
$$\frac{\partial}{\partial x_j}\left[-\bar{q}_j - \bar{q}_{\phi_j} - \overline{\rho u_j'' h''} + \overline{\tau_{ji}u_i''} - \overline{\rho u_j''\frac{1}{2}u_i'' u_i''} + \tilde{u}_i\left(\bar{\tau}_{ij} - \overline{\rho u_i'' u_j''}\right)\right]$$

$$\frac{\partial}{\partial t}\left(\bar{\rho}\tilde{\phi}_i\right) + \frac{\partial}{\partial x_j}\left(\bar{\rho}\tilde{\phi}_i\tilde{u}_j\right) = \frac{\partial}{\partial x_j}\left(\bar{\rho}\mathcal{D}_{\mathrm{im}}\frac{\partial}{\partial x_j}\tilde{\phi}_i - \overline{\rho\phi_i'' u_j''}\right) + \tilde{Q}_i \tag{2.20}$$

These equations are similar in form to the original conservation equations (2.1)–(2.3) and (2.8), but there are some new terms, averages of products of fluctuations which cannot be assumed to vanish. The continuity equation retains its original form, but the momentum equation has a new term, the Favre-averaged Reynolds-stress tensor $-\overline{\rho u_i'' u_j''}$. It represents turbulent momentum transport, and appears in the equations as an additive term for the viscous stresses. The same term appears also in the energy equation, and again as an apparent turbulent shear stress.

Also the energy equation contains some new terms, which can be interpreted in a similar manner to the Reynolds-stress tensor. The term $(1/2)\overline{\rho u_i'' u_i''}$ represents the turbulent kinetic energy per unit volume, and is usually denoted by $\bar{\rho}k$. The term $\overline{\rho u_j'' h''}$ is the turbulent conduction of heat, and $\overline{\tau_{ij}u_i''}$ is the turbulent work of molecular stresses. The term $\overline{\rho u_j''\frac{1}{2}u_i'' u_i''}$ represents the turbulent transport of turbulent kinetic energy. The term $\bar{q}_{\phi_j}$ represents the diffusion of energy due to diffusion of mass, and it is used to denote the contributions of both the molecular and turbulent diffusion of mass.

So far, the operations performed on the conservation equations have been purely mathematical. Equations (2.17)–(2.20) are basically filtered versions of the original ones, with all fluctuations with a period less than T filtered out, as is obvious from Eqs. (2.12) and (2.13). The problem is that the correlations mentioned above have to be modelled with a turbulence model.

There is another fundamental problem with both Reynolds-averaging and Favre-averaging: the time-scale T employed in the averaging is present only in the derivation procedure, but so far the majority of all the existing turbulence models are independent of T. The idea behind the the time-averaging is, however, that a time-scale larger than the turbulent time-scales but smaller than the mean flow time-scales would exist, thus justifying the filtering procedure. Unfortunately, there is no law forcing this to happen. In addition, most models carry out this filtering by diffusive damping, and therefore the simulation of time-dependent flows with Reynolds-averaged or Favre-averaged equations is a little bit questionable. Since this is currently the only practical method available, the so introduced errors are hoped to be small.

2.2.4 Thermodynamics of a Mixture of Gases

When dealing with thermodynamics, this text will consider only perfect gases, i.e. gases where intermolecular forces are negligible. This is a good approximation for gases at low pressures ($p < 1000$ bar) and all but low temperatures ($T > 30$ K), which is the case in most aerodynamic flows [31]. For a perfect gas, the equation of state is

$$p = \rho R T \tag{2.21}$$

Here, however, the specific gas constant R is a function of the chemical composition of the mixture, which in turn is a function of the solution of the flow field. For a mixture, R is calculated from

$$R = \mathcal{R}/\mathcal{M} \tag{2.22}$$

where $\mathcal{R}$ is the universal gas constant 8.314 J/mol K and $\mathcal{M}$ is the molecular weight of the mixture.

The thermodynamic properties of a mixture of gases can be determined by analyzing the thermodynamics of the components of the mixture. Each component in turn is a thermally perfect gas, and we can write for each species i

$$\begin{aligned}
R_i &= \mathcal{R}/\mathcal{M}_i && (2.23)\\
p_i &= \rho_i R_i T && (2.24)\\
\mathrm{d}e_i &= c_{v_i}\,\mathrm{d}T && (2.25)\\
\mathrm{d}h_i &= c_{p_i}\,\mathrm{d}T && (2.26)\\
c_{v_i} &= c_{p_i} - R_i && (2.27)
\end{aligned}$$

where p_i is the partial pressure and R_i is the specific gas constant of species i. c_{v_i} and c_{p_i} are the specific heats of species i at constant density and pressure, respectively. For a mixture of n species we have

$$\begin{aligned}
p &= \sum_i p_i && (2.28)\\
R &= \sum_i \phi_i\, R_i && (2.29)\\
e &= \sum_i \phi_i\, e_i && (2.30)\\
h &= \sum_i \phi_i\, h_i && (2.31)\\
\mathcal{M} &= \frac{1}{\sum_i \phi_i/\mathcal{M}_i} && (2.32)
\end{aligned}$$

For a calorically perfect gas, the specific heat capacity c_v is constant, which is a valid approximation for air up to 800 K [31, p. 373]. When the temperature is increased

enough, the gas becomes vibrationally excited and some of its internal energy is occupied by the vibrational energy of the molecules. Therefore, the specific heat capacity c_v is not constant but a function of T, and the gas is by definition thermally perfect. From quantum mechanics [31, pp. 435–440], we have for the vibrational energy of a single species e_{vib} the result

$$e_{vib} = \frac{h\nu/kT}{e^{h\nu/kT} - 1} RT \tag{2.33}$$

where h denotes Planck's constant, k is the Boltzmann constant, and ν is the fundamental vibrational frequency of the molecule. This equation is tricky to solve for T and therefore it is not straightforward to apply to computations — not to mention a mixture of several species.

In light of the above, for a given gas composition, the internal energy $e = f(T)$ and enthalpy $h = g(T)$ of the gas are functions of temperature T only. Due to the complicated form of the expression for vibrational energy in Eq. (2.33), some approximate expressions are usually employed for c_{v_i} and c_{p_i} to facilitate streamlined computation of the functional relationships $T = f^{-1}(e) = g^{-1}(h)$.

2.2.5 Transport Properties of a Mixture

The transport properties of a mixture are determined employing Sutherland's formula for viscosity and thermal conductivity for each species, and the mixture properties are obtained with Wilke's rule [35]

$$\mu_{\text{mix}} = \sum_{i=1}^{n} \frac{X_i \mu_i}{\sum_{j=1}^{n} X_j \Phi_{ij}} \tag{2.34}$$

where

$$\Phi_{ij} = \frac{\left(1 + \sqrt{\mu_i/\mu_j \sqrt{\mathcal{M}_j/\mathcal{M}_i}}\right)^2}{\sqrt{8 + 8\,\mathcal{M}_i/\mathcal{M}_j}} \tag{2.35}$$

$$X_i = \phi_i \frac{\mathcal{M}}{\mathcal{M}_i} = \frac{N_i}{N} = \frac{p_i}{p} \tag{2.36}$$

In Eq. (2.36) X_i and N_i are the mole fraction and the number of particles, respectively, of species i in a given system. An exactly similar formula holds for thermal conductivity. Each occurrence of μ_i is simply replaced by k_i.

2.2.6 Chemical Reactions in a Mixture of Gases

Under suitable conditions, chemical reactions may take place and the chemical composition of the gas mixture is changed. These reactions may be unidirectional,

where reactions only take place in one direction, or bidirectional, when a backward reaction may also occur.

A unidirectional reaction is one in which, from a macroscopic point of view, a fuel and an oxidant react and produce some product. For example, in the following schematic reaction, A and B will produce C

$$A + B \rightarrow C \tag{2.37}$$

The reaction takes place as long as there is enough fuel and oxidant present and some other conditions are fulfilled, e.g. the temperature is high enough.

A bidirectional reaction consists of two elementary reactions in which the reaction products may react in a backward direction and produce more of the original reactants. An elementary reaction is such that takes place in a single step. One example of such a reaction is the dissociation–recombination of oxygen

$$\mathrm{O}_2 + M \rightleftarrows 2\mathrm{O} + M \tag{2.38}$$

where M is a collision partner. The forward and backward specific reaction rates are denoted by k_f and k_b, respectively, both of which are functions of temperature only. The rates of production and consumption of O_2 and O are functions of the respective concentrations, and in equilibrium production and consumption balance each other. This type of equation is one which tries to reach an equilibrium state, and, for given initial concentrations, the equilibrium concentrations of the components are functions of temperature only.

In reality, many reactions, which may seem to be elementary reactions, actually consist of several elementary reactions, which, from a macroscopic point of view, are reacting all together in one single step. Strictly speaking, the previous formalism about reaction rates applies only to elementary reactions [31, p. 495].

Another thing associated with reactions is the concept of heat of reaction. When a reaction proceeds, a certain amount of heat may be released (exothermic reaction) or consumed (endothermic reaction). The dissociation reaction described above is endothermic because it takes energy to dissociate an O_2 molecule. Consequently, the recombination reaction is exothermic since then the same amount of energy is released as is required for the dissociation reaction to take place.

2.3 Modelling of the Physics of Fluid Flow

Some theoretical aspects of the underlying physics of fluid flow were described in the previous section. Many details remained open in the sense that an equation could not be derived from first principles, or the resulting system of equations would become far too complex to solve for any practical flow case. To overcome these problems, simplified models are employed to close the system of equations.

2.3.1 Turbulence Modelling

Reynolds Stress Modelling

The main problem with turbulence modelling is to obtain expressions for the new terms in Eqs. (2.17)–(2.20) produced by time-averaging, above all the Reynolds stresses $-\overline{\rho u_i'' u_j''}$. Differential equations for the Reynolds stresses can be derived, but they involve a number of new terms, which again require modelling. However, if this kind of a modelling is conducted, the turbulence-modelling approach is called Reynolds stress modelling (RSM). The main problem in that particular area is to generate satisfactory models for the unknown source terms appearing in the equations for the Reynolds stresses.

The class of Reynolds stress models includes a simplifying sub-class, the Algebraic Reynolds stress models (ARSM), in which a two-equation model, like the $k-\epsilon$ or $k-\omega$ model, is combined with a model for the anisotropies of the Reynolds stresses. The convection and diffusion terms of the differential equations for the anisotropies are assumed to be negligible in comparison with the source terms. As a result, a set of implicit nonlinear algebraic equations for the stresses is obtained. A further simplification is to express the individual stresses as explicit algebraic functions of the flow properties. This allows for straightforward calculation of the stresses without limiting assumptions about the properties of the turbulent fluctuations. These types of models are called Explicit Algebraic Reynolds Stress models (EARSM), and because the ARSM and EARSM models are normally combined with a two-equation turbulence model, they are also called nonlinear two-equation models.

Two-Equation Turbulence Models

In two-equation turbulence models, the equations for the Reynolds stresses are replaced with two transport equations for the turbulent kinetic energy k and a length-scale variable ψ, like ϵ or ω. The Reynolds stresses are then obtained with some assumed relationship between $-\overline{\rho u_i'' u_j''}$, k, ψ and the mean flow strain-rate tensor. Usually, the Boussinesq's approximation is employed as

$$-\overline{\rho u_i'' u_j''} = \mu_T \left[2S_{ij} - \frac{2}{3}\delta_{ij}\frac{\partial u_k}{\partial x_k} \right] - \frac{2}{3}\delta_{ij}\rho k \tag{2.39}$$

where μ_T is a turbulent viscosity coefficient obtained from k and ψ. The basic equations for k and ψ written in conservative form are

$$\frac{\partial}{\partial t}(\rho k) + \frac{\partial}{\partial x_j}(\rho k\, u_j) = \frac{\partial}{\partial x_j}\left(\mu_k \frac{\partial}{\partial x_j} k \right) + Q_k \tag{2.40}$$

$$\frac{\partial}{\partial t}(\rho \psi) + \frac{\partial}{\partial x_j}(\rho \psi\, u_j) = \frac{\partial}{\partial x_j}\left(\mu_\psi \frac{\partial}{\partial x_j} \psi \right) + Q_\psi \tag{2.41}$$

where Q_k and Q_ψ are the source terms for ρk and $\rho\psi$, respectively. μ_k and μ_ψ are the corresponding viscosities often approximated with

$$\mu_k = \mu + \frac{\mu_T}{\sigma_k} \qquad \mu_\psi = \mu + \frac{\mu_T}{\sigma_\psi} \tag{2.42}$$

where σ_k and σ_ψ are the appropriate Schmidt numbers for k and ψ, respectively. Although not required, σ_k and σ_ψ are usually assumed to have constant values. With the above equations, we have implicitly assumed the gradient-diffusion model to be valid for k and ψ.

The two-equation models are classed based on the choice of the turbulence variables to be solved. In this text, only $k-\epsilon$ and $k-\omega$ models are considered.

$k-\epsilon$ Turbulence Models The source terms for the $k-\epsilon$ model are

$$Q_{\rho k} = P - \rho\epsilon \tag{2.43}$$

$$Q_{\rho\epsilon} = c_1\frac{\epsilon}{k}P - c_2\frac{\rho\epsilon^2}{k} \tag{2.44}$$

where $c_1 = 1.44$ and $c_2 = 1.92$ are model constants. P is the production of turbulent kinetic energy, which, employing Boussinesq approximation, is written as

$$\begin{aligned} P &\equiv -\overline{\rho u_i'' u_j''}\frac{\partial u_i}{\partial x_j} \\ &= \left[\mu_T\left(2S_{ij} - \frac{2}{3}\delta_{ij}\frac{\partial u_k}{\partial x_k}\right) - \frac{2}{3}\delta_{ij}\rho k\right]\frac{\partial u_i}{\partial x_j} \end{aligned} \tag{2.45}$$

In the $k-\epsilon$ model the turbulent viscosity is calculated from

$$\mu_T = c_\mu\frac{\rho k^2}{\epsilon} \tag{2.46}$$

where $c_\mu = 0.09$ is a constant. Also, $\sigma_k = 1.0$ and $\sigma_\epsilon = 1.3$ are kept as constants. As such, the $k-\epsilon$ model is not suitable for boundary layer calculations due to the lack of sufficient viscous damping in the near-wall region. There are two different approaches for using the $k-\epsilon$ model in such cases. One can either use the wall-function approach, or one can use a low-Reynolds number $k-\epsilon$ model. The subsequent effects are described below.

When using a wall-function approach, the solution of all the conservation equations is not extended to the wall. Instead, the grid point closest to the wall is located into the log-law layer. The region between the first point and the wall is modelled by fitting the log-law velocity profile to the solution at the first point and solving for the friction velocity $u_\tau = \sqrt{\tau_w/\rho}$, where τ_w is the shear stress on the wall. Boundary values for k and ϵ are obtained as functions of u_τ and y.

In a low-Reynolds number model, viscous damping is enchanced with additional wall-damping functions, and the standard solution procedure is extended to the wall. The wall-damping functions are usually functions of some of the following parameters

$$y^+ = \frac{\rho y_\mathrm{n} u_\tau}{\mu} \qquad Re_T = \frac{\rho k^2}{\epsilon\mu} \qquad Re_y = \frac{\rho y_\mathrm{n}\sqrt{k}}{\mu} \tag{2.47}$$

where y_n is the normal distance from the wall. For example, the low-Reynolds number model of Chien [36] has source terms with the following form

$$Q_{\rho k} = P - \rho\epsilon - 2\mu\frac{k}{y_\mathrm{n}^2} \tag{2.48}$$

$$Q_{\rho\epsilon} = c_1\frac{\epsilon}{k}P - c_2\frac{\rho\epsilon^2}{k} - 2\mu\frac{\epsilon}{y_\mathrm{n}^2}e^{-y^+/2} \tag{2.49}$$

with definitions

$$c_1 = 1.44 \tag{2.50}$$

$$c_2 = 1.92(1 - 0.22e^{-Re_T^2/36}) \tag{2.51}$$

$$c_\mu = 0.09(1 - e^{-0.0115y^+}) \tag{2.52}$$

We might note here that Chien's original model has slightly different constant coefficients in the expressions for c_1 and c_2, namely 1.35 and 1.80. In the present implementation [17], however, the coefficients from the standard model are used in Eqs. (2.50)–(2.52).

The dissipation of ρk has an extra term, $2\mu k/y_\mathrm{n}^2$, which, in effect, redefines ϵ in Chien's model. Likewise, the dissipation of $\rho\epsilon$ also has an additional term, $2\mu\epsilon/y_\mathrm{n}^2 e^{-y^+/2}$, which is a direct consequence of the redefinition of ϵ. Chien's ϵ is often denoted by $\tilde{\epsilon}$, but from now on in this text, it will be denoted simply by ϵ, and the "standard" dissipation in Eq. (2.44) will be denoted with ε, where necessary. The relation between these is

$$\rho\varepsilon = \rho\epsilon + 2\mu\frac{k}{y_\mathrm{n}^2} \tag{2.53}$$

This type of modelling allows for integration of the equations up to the wall. The boundary values of both ρk and $\rho\epsilon$ are conveniently set to zero. The additional multipliers in the Eqs. (2.50)–(2.52) are supposed to provide sufficient additional damping to model the effects of a solid wall.

The parameter y^+ has an undesirable property in that it depends on the friction velocity u_τ. This may cause severe problems near separation points because at those points $\tau_\mathrm{w} \to 0$ and consequently $u_\tau \to 0$ and $y^+ \to 0$. Also, the presence of $1/y_\mathrm{n}^2$ in the source terms causes some non-uniqueness to the equations in the vicinity of several walls.

In the implementation employed in this work, the expression for y^+ is modified to contain the absolute value of vorticity instead of the velocity gradient on the wall

$$y^+ = y_\mathrm{n}\frac{\rho u_\tau}{\mu} = y_\mathrm{n}\frac{\sqrt{\rho\tau_\mathrm{w}}}{\mu} = y_\mathrm{n}\sqrt{(\rho|\Omega|/\mu)_\mathrm{w}} \tag{2.54}$$

where $|\Omega| = \sqrt{2\Omega_{ij}\Omega_{ij}}$ is the absolute value of vorticity and the vorticity tensor is defined by

$$\Omega_{ij} = \frac{1}{2}\left(\frac{\partial u_i}{\partial x_j} - \frac{\partial u_j}{\partial x_i}\right) \tag{2.55}$$

This way, most of the problems caused by zero friction velocity near separation points are avoided. Also, in the presence of several walls, the contributions of all the walls are summed to obtain the final additional wall damping to the source terms [19]. In a similar manner, the damping terms in Eq. (2.52) are multiplied by each other.

$k-\omega$ Turbulence Models The $k-\omega$ model was first proposed by Kolmogorov in 1942 [34]. Since then, a few scientists have developed the model, but only lately has the model gained wider popularity in the form known as the $k-\omega$ SST model [37, 38].

Wilcox's $k-\omega$ model [39] is the basis for most modern $k-\omega$ models. In Wilcox's model, the source terms for ρk and $\rho\omega$ are

$$Q_{\rho k} = P - \beta^* \rho k \omega \tag{2.56}$$

$$Q_{\rho\omega} = \alpha\frac{\omega}{k}P - \beta\rho\omega^2 \tag{2.57}$$

where $\alpha = 5/9$, $\beta = 0.075$ and $\beta^* = 0.09$ are model constants. The Schmidt numbers have constant values $\sigma_k = 2.0$ and $\sigma_\omega = 2.0$. The production of turbulent kinetic energy P is modelled as in the $k-\epsilon$ model using Eq. (2.45). The turbulent viscosity is obtained from

$$\mu_T = \frac{\rho k}{\omega} \tag{2.58}$$

As is obvious, the formal relationship between ε and ω is

$$\omega = \frac{\varepsilon}{\beta^* k} \tag{2.59}$$

The "standard" $k-\omega$ model presented above is known to be sensitive to the free-stream value of ω [38]. To overcome these problems, Menter decided to blend the $k-\omega$ model and the $k-\epsilon$ model transformed to the $k-\omega$ form so that the model would reduce to the standard $k-\omega$ near solid surfaces, and switch to $k-\epsilon$ elsewhere. A blending function F_1 is employed for mixing the $k-\omega$ and the $k-\epsilon$ models. In Menter's model, known as the new baseline model (BSL), the source terms are

$$Q_{\rho k} = P - \beta^* \rho k \omega \tag{2.60}$$

$$Q_{\rho\omega} = \frac{\gamma\rho}{\mu_T}P - \beta\rho\omega^2 + (1-F_1)\frac{2\rho}{\sigma_{\omega 2}\omega}\frac{\partial k}{\partial x_j}\frac{\partial \omega}{\partial x_j} \tag{2.61}$$

The new term in the source term for $\rho\omega$ is known as the cross-diffusion term, denoted here with $CD_{k\omega}$. It originates from the transformed $k-\epsilon$ equations, and it is present only when $F_1 < 1$. F_1 is defined by

$$F_1 = \tanh\left(\Gamma^4\right) \tag{2.62}$$

where

$$\Gamma = \min\left(\max\left(\frac{\sqrt{k}}{\beta^*\omega d}; \frac{500\nu}{\omega d^2}\right); \frac{4\rho k}{CD_{k\omega}\sigma_{\omega 2} d^2}\right) \tag{2.63}$$

where d is the distance to the nearest wall point. The model constants are also blended as

$$\left(\sigma_k\ \sigma_\omega\ \beta\right)^T = F_1\left(\sigma_k\ \sigma_\omega\ \beta\right)_1^T + \left(1-F_1\right)\left(\sigma_k\ \sigma_\omega\ \beta\right)_2^T \tag{2.64}$$

where subscripts 1 and 2 refer to constants in Wilcox's model and the transformed $k-\epsilon$ model, respectively. The model constants of the transformed $k-\epsilon$ model are

$$\sigma_{k2} = 1.0 \qquad \sigma_{\omega 2} = 1.168 \qquad \beta_2 = 0.0828 \tag{2.65}$$

and, with $\kappa = 0.41$ kept as constant, γ is defined by

$$\gamma = \frac{\beta}{\beta^*} - \frac{\kappa^2}{\sigma_\omega\sqrt{\beta^*}} \tag{2.66}$$

The above equations describe the $k-\omega$ BSL model. The $k-\omega$ SST model presented by Menter [38] is a further developed version of the $k-\omega$ BSL model. The idea is to set an upper limit for the turbulent shear stress in boundary layers. In the SST model the eddy viscosity μ_T is defined as

$$\mu_T = \frac{a_1\rho k}{\max\left(a_1\omega; |\Omega|F_2\right)} \tag{2.67}$$

where $a_1 = 0.31$. The lower limit of the denominator of Eq. (2.67) is based on Bradshaw's assumption that in boundary-layer flows the principal turbulent shear stress, denoted here by $\overline{\rho u'' v''}$, depends on k as follows

$$\left|\overline{\rho u'' v''}\right| = a_1\rho k \tag{2.68}$$

The conventional Kolmogorov-Prandtl expression in Eq. (2.58) is used as far as it does not exceed the value

$$\mu_T = \frac{\left|\overline{\rho u'' v''}\right|}{|\Omega|} = \frac{a_1\rho k}{|\Omega|} \tag{2.69}$$

This is called the SST limitation for μ_T and it significantly improves the model performance for adverse pressure-gradient boundary layers, since the conventional formulation clearly overestimates μ_T in the presence of adverse pressure gradients [37, 38]. The same values for the model constants apply for both the BSL and the

SST models except that the Schmidt number σ_{k1} has the value of 1.176 in the SST model. The SST limitation is suitable only for wall-bounded flows. The purpose of the function F_2 in Eq. (2.67) is to prevent the activation of the SST limitation in free shear flows. F_2 behaves otherwise like F_1 except that it remains at unity further out in the defect layer and it is given by

$$F_2 = \tanh\left(\Gamma_2^2\right) \tag{2.70}$$

where

$$\Gamma_2 = \max\left(\frac{2\sqrt{k}}{\beta^* \omega d}; \frac{500\nu}{\omega d^2}\right) \tag{2.71}$$

In the implementation employed in the present computations, the SST limitation is further developed by Hellsten [40] from its original form, and μ_T is obtained from

$$\mu_T = \frac{a_1 \rho k}{\max\left(a_1 \omega; |\Omega| F_2 F_3\right)} \tag{2.72}$$

The F_3 function is designed to prevent the SST limitation from being activated in the roughness layer in rough-wall flows, i.e. the layer very close to the rough wall. This is necessary because Bradshaw's assumption is not valid there. The function F_3 is given by

$$F_3 = 1 - \tanh\left[\left(\frac{150\nu}{\omega d^2}\right)^4\right] \tag{2.73}$$

In general, the $k-\omega$ model tends to produce better results than the $k-\epsilon$ model in adverse pressure-gradient flows [34]. A clear advantage of the $k-\omega$ model is the freedom of wall-damping functions. On the other hand, the solid wall boundary condition for ω is theoretically infinite, and therefore the boundary conditions have to be specified with extreme care. The methods employed in the present computations to specify the boundary conditions for $\rho\omega$ were developed and tested by Hellsten [41, 42].

Weaknesses of the Two-Equation Turbulence Models A common weakness in both the $k-\epsilon$ and $k-\omega$ models is related to the use of Boussinesq approximation. As such, it is actually not a weakness of the $k-\epsilon$ or the $k-\omega$ model, but since the Boussinesq approximation is almost regularly employed with them, the associated problems should also be identified. The alternative would be to use a nonlinear stress–strain relationship for the turbulent stresses, and that is actually what was previously denoted with EARSM.

The main weakness of Eq. (2.39) is the assumption that the turbulent stress tensor is aligned with the main strain-rate tensor. This assumption works quite well in plain shear flow, but fails totally in impinging flows and in flows with strong streamline curvature and swirl [43].

The problems with the impinging flow were encountered by Kaurinkoski and Hellsten [18] in front of the stagnation point of an artillery projectile. Following Menter [37], an ad-hoc fix was developed to limit the production of turbulent kinetic energy with

$$P_{\max} = \left\{ 2 + 18 \, \tanh \left[\left(\frac{|\Omega|}{\Omega_{\text{ref}}} \right)^{n_\omega} \right] \right\} \rho\varepsilon \tag{2.74}$$

Here, C_Ω is a model parameter set to 0.03 and the exponent $n_\omega = 4$ is also a selected model parameter. In Eq. (2.74), Ω_{ref} is given by

$$\Omega_{\text{ref}} \approx C_\Omega \frac{V_\infty}{\delta} = C_\Omega \frac{V_\infty \sqrt{Re_\infty}}{5.3\, L} \tag{2.75}$$

where δ is an estimate for the boundary-layer thickness based on the Blasius solution for the flat plate boundary layer. L is a characteristic length for the flow case, and V_∞ is the free-stream velocity.

Eq. (2.74) is called the Vorticity-Based Production Limit (VBPL), and is employed in all the subsequent computations presented in this work, unless stated otherwise. In addition, a rotation and curvature correction presented by Hellsten [42] is employed in all the computations with the $k-\omega$ model in this work. The basic idea with the correction is to modify the turbulent length-scale by multiplying $\beta\rho\omega^2$ in Eq. (2.61) by a function F_4 defined by

$$F_4 = \frac{1}{1 + C_{rc} Ri} \tag{2.76}$$

where Ri is the Richardson number defined by

$$Ri = \frac{|\Omega_{ij}|}{|S_{ij}|} \left(\frac{|\Omega_{ij}|}{|S_{ij}|} - 1 \right) \tag{2.77}$$

Later on in this work, the model will be called the $k-\omega$ RCSST model.

Algebraic Turbulence Models

The simplest class of turbulence models is known as zero-equation turbulence models, or algebraic turbulence models. They are such that no separate conservation equation is solved for a turbulence variable. Instead, the turbulent stresses are evaluated based on Boussinesq approximation with a μ_T obtained from the model. Therefore, the models are actually models for μ_T in terms of the local flow field properties. The underlying theory is based on the analogy between turbulent fluctuations and random molecular movement. The conceptual expression for the turbulent stress in a simple shear flow is

$$-\overline{\rho u'' v''} = \frac{1}{2} \rho v_{\text{mix}} l_{\text{mix}} \frac{\mathrm{d}u}{\mathrm{d}y} \tag{2.78}$$

where v_{mix} is the mixing velocity and l_{mix} is the mixing length, both determined based on local flow properties, and the distance to the wall or the wake centreline.

Prandtl postulated that the mixing velocity can be expressed in terms of the mixing length [34]

$$v_{\text{mix}} = \text{constant} \cdot l_{\text{mix}} \left| \frac{\mathrm{d}u}{\mathrm{d}y} \right| \tag{2.79}$$

which leaves us only with one unknown, the mixing length l_{mix}. There are various models based on the mixing length concept [44, 45], and basically they all share the same weaknesses. They do not model history effects in any way, and they have problems with separation points due to the vanishing friction velocity u_τ, since they usually employ y^+ in one way or another. Also, since the models are often developed for aerodynamic boundary layer type flows, they explicitly need the boundary-layer thickness, which may be tricky to determine in complicated flow cases.

Turbulent Scalar–Equations

The time-averaging procedure described earlier produced a species conservation equation (2.20) with an additional term representing turbulent diffusion of mass. The whole diffusion term of Eq. (2.20) is often modelled with

$$\frac{\partial}{\partial x_j} \left(\bar{\rho} \mathcal{D}_{\text{im}} \frac{\partial}{\partial x_j} \tilde{\phi}_i - \overline{\rho \phi_i'' u_j''} \right) \approx \frac{\partial}{\partial x_j} \left(\mu_{\phi_i} \frac{\partial}{\partial x_j} \tilde{\phi}_i \right) \tag{2.80}$$

where

$$\mu_{\phi_i} = \frac{\mu}{\sigma_{\phi_{iL}}} + \frac{\mu_T}{\sigma_{\phi_{iT}}} \tag{2.81}$$

Here $\sigma_{\phi_{iL}}$ and $\sigma_{\phi_{iT}}$ are the laminar and turbulent Schmidt numbers for ϕ_i, respectively. This type of gradient diffusion modelling is consistent with the modelling of the diffusion of ρk and $\rho \psi$ in Eqs. (2.40) and (2.41). Just like σ_k and σ_ψ, the Schmidt numbers $\sigma_{\phi_{iL}}$ and $\sigma_{\phi_{iT}}$ are not required to have constant values, although this is usually the case.

The turbulent conduction of heat in the energy equation (2.19) is usually modelled employing the eddy viscosity model. Also, the energy diffusion due to the diffusion of mass is modelled in this work by simply multiplying the total diffusion of species i by h_i and thus the whole energy diffusion is modelled as

$$\frac{\partial}{\partial x_j} \left(k \frac{\partial}{\partial x_j} T - \overline{\rho u_j'' h''} - \bar{q}_{\phi_j} \right) = \frac{\partial}{\partial x_j} \left((k + k_T) \frac{\partial}{\partial x_j} T + \bar{h}_k \mu_{\phi_k} \frac{\partial}{\partial x_j} \tilde{\phi}_k \right) \tag{2.82}$$

where

$$k_T = \mu_T \frac{c_p}{Pr_T} \tag{2.83}$$

Here Pr_T is the turbulent Prandtl number, and c_p is the specific heat of the gas.

2.3.2 Modelling of the Thermo-Chemical Details

When analyzing reactive flows, there are several new issues that have to be modelled. As temperatures rise, the thermodynamic properties of the gases change, as explained in Section 2.2.4. One possibility is, of course, to ignore the changes, but in order to model these changes, the basic problem is to model the dependency between e and T. Another thing is to account for the changes caused by the changes in the composition, may they be caused by reactions or mixing. This issue is coupled to the concept of heat of reaction.

Thermodynamic Model

For the thermodynamic details, the model selected in this work is based on curve-fit equations for the properties of individual gases. Knacke [46] gives an interpolation equation for $C_p = \mathcal{M} c_p$ with coefficients A, B, C and D as

$$C_p = A + B10^{-3}T + C10^{6}T^{-2} + D10^{-6}T^{2}, \qquad T > 25^{\circ}\mathrm{C} \tag{2.84}$$

where the second and third term account for vibrational energy and the fourth term covers the contribution of electronic energy. With Eq.(2.84) the equation of state is closed and the remaining problem is to solve for T with a given e and ρ. The details are shown in Ref. [22]. In order to be able to model the heat release associated with chemical reactions, the heat of formation is included in the expression of total internal energy, i.e. energies are treated as absolute energies as

$$e = h_0^{T=0} + \int_0^T c_v \, \mathrm{d}T \tag{2.85}$$

where $h_0^{T=0} = \sum_i \phi_i \, h_{0_i}^{T=0}$ is the heat of formation of the mixture at $T = 0\,\mathrm{K}$. Changes in the local mixture composition will then immediately be seen as changes in the heat of formation, which is subtracted from the absolute energy to get the sensible energy. For a given mixture composition, the sensible energy is a function of the temperature only, and consequently, the temperatures will change if the sensible energies are changed.

There is also another possibility to model the heat release, which would involve treatment of the energies as sensible energies. Then, the energy equation (2.3) would have to be completed with a source term accounting for the chemical energy exchange [31, p. 617]. The choice is free, but once either one is selected, the whole treatment of energies has to be consistent throughout the solver. In the end, it is a matter of taste which one is more convenient.

One point worth mentioning here is the way $h_{0_i}^{T=0}$ is obtained. The tables given by Knacke [46] contain a reference enthalpy at $T = 25^{\circ}\mathrm{C}$. Also, as explained in Ref. [22], the employed model for $c_{p_i}(T)$ at temperatures below $T = 25^{\circ}\mathrm{C}$ approximates c_{p_i} with constant values evaluated at $T = 25^{\circ}\mathrm{C}$. The values for $h_{0_i}^{T=0}$ are obtained consistently from

$$h_{0_i}^{T=0} = h_{0_i}^{T=25^\circ\mathrm{C}} - 298 \cdot c_{p_i}^{T=25^\circ\mathrm{C}} \tag{2.86}$$

The value of $c_{p_i}^{T=25^\circ\mathrm{C}}$ is calculated with Eq. (2.84).

Reaction Model

An arbitrary single-step chemical reaction can be expressed as

$$\sum_{i=1}^{N} \nu_i' M_i \;\rightarrow\; \sum_{i=1}^{N} \nu_i'' M_i \tag{2.87}$$

where ν_i' is the stoichiometric coefficient of reactant i, and ν_i'' is the stoichiometric coefficient of product i. M_i is an arbitrary specification of the chemical species i, and N is the total number of species involved.

The law of mass action [27], which is confirmed by experimental results, states that the reaction rate depends on the concentrations of the reactants raised to the power equal to the corresponding stoichiometric coefficient as

$$\mathrm{RR} = k \prod_{i=1}^{N} (C_{M_i})^{\nu_i'} \tag{2.88}$$

where C_{M_i} is the concentration of species i, and ν_i is the corresponding stoichiometric coefficient of the reactant. k is the specific reaction rate coefficient, which is a function of the temperature and the reaction under consideration. A widely used empirical model for the specific reaction rates of elementary reactions is the Arrhenius equation

$$k = A e^{-E_\mathrm{a}/\mathcal{R}T} \tag{2.89}$$

where E_a is the activation energy of the reaction, and A is a reaction-dependent coefficient. It may be approximated with a pre-exponential factor, and the Arrhenius equation is written as

$$k = a_1 T^\alpha e^{-E_{\mathrm{a}1}/\mathcal{R}T} \tag{2.90}$$

where a_1, α and $E_{\mathrm{a}1}$ are found from experiments. As explained in Subsection 2.2.6, this type of a formalism is unfortunately valid only for elementary reactions. For a small set of reactions, like the dissociation-recombination of oxygen, the above approach is useful, but for a detailed description of the combustion of a base-bleed propellant, the whole concept of solving the mass fractions of every single species present in the complicated chain of reactions is not feasible. Therefore, in this work, a different kind of approach has been selected.

First of all, all the fine details of the reaction mechanism are dropped. The combustion reaction of the partially burned propellant (or fuel in the test case of Chapter 4) is modelled with the conceptual form of Eq. (2.37) as

$$1 \text{ kg } \textit{Fuel} + r_\mathrm{fu} \text{ kg } \textit{Air} \;\rightarrow\; (1 + r_\mathrm{fu}) \text{ kg } \textit{Products} \tag{2.91}$$

where r_{fu} is the oxidant-to-fuel mass ratio. As is obvious, this kind of reaction is not an elementary reaction and an expression like Eq. (2.89) is not valid.

Assuming temperatures are high enough for the reactions to take place, the reactions themselves are, in reality, usually very fast. Under such conditions, the rate-limiting phenomenon is the mixing of the reactants, not the reaction kinetics. Actually, as Spalding points out in Ref. [24], a reaction model based solely on the average concentrations of the reactants gives results which are not even qualitatively correct. Therefore, he deduced that a proper model would utilize a time-scale based on the local turbulence conditions. Originally, a model based on the mixing-length concept was proposed [24], but after a some more development [27], the eddy breakup model of combustion (EBU) was introduced by Spalding as

$$\overline{Q_{\mathrm{pr}}} = C_{\mathrm{EBU}}\,\bar{\rho}\frac{\varepsilon}{k}\sqrt{\overline{\phi'^{\,2}_{\mathrm{fu}}}} \tag{2.92}$$

where Q_{pr} is the rate of product formation, ϕ'_{fu} is the fuel mass fraction fluctuation, and C_{EBU} is a model constant. The drawback of this model is that it requires explicit knowledge of the mass fraction fluctuations. To remove this problem, Magnussen and Hjertager [23] proposed a model based on only the time-average values according to which the time-rate of the consumption of fuel is

$$Q_{\mathrm{fu}} = -C_R\,\rho\,\frac{\varepsilon}{k}\,\min\left(\phi_{\mathrm{fu}}\,,\ \frac{\phi_{\mathrm{ox}}}{r_{\mathrm{fu}}}\,,\ C_{R1}\frac{\phi_{\mathrm{pr}}}{(1+r_{\mathrm{fu}})}\right) \tag{2.93}$$

where $C_R = 4.0$ and $C_{R1} = 0.5$ are model constants. All the values present in the above equation are time-averages, and the overbars have been dropped. As can be seen, the reaction rate is also a function of the mass fraction of the reaction product.

In the present implementation of the EBU model, Eq. (2.93) has been modified somewhat. First, we identify the turbulence time-scale τ defined based on k and ε or k and ω as

$$\tau \sim \frac{k}{\varepsilon} \qquad\qquad \tau \sim \frac{1}{\omega} \tag{2.94}$$

According to Eq. (2.59), ε/k may be replaced with $\beta^*\omega$. Also, the dependency of the reaction rate on the mass fraction of the reaction product is undesirable in the sense that with a zero initial reaction product mass fraction, the reaction will never start. Therefore, in the present implementation, ϕ_{pr} in Eq. (2.93) has been changed to $\max\left(\phi_{\mathrm{pr}}, \phi_{\mathrm{pr}_{\mathrm{min}}}\right)$. Also, the time-scale is expressed in terms of k and ω, because with this formulation the expression for the reaction rate becomes simpler. The final form of the implemented EBU model is

$$Q_{\mathrm{fu}} = -C_R\,\beta^*\rho\omega\,\min\left(\phi_{\mathrm{fu}}\,,\ \frac{\phi_{\mathrm{ox}}}{r_{\mathrm{fu}}}\,,\ C_{R1}\frac{\max\left(\phi_{\mathrm{pr}}\,,\ \phi_{\mathrm{pr}_{\mathrm{min}}}\right)}{(1+r_{\mathrm{fu}})}\right) \tag{2.95}$$

where $\phi_{\mathrm{pr}_{\mathrm{min}}} = 0.001$ is employed to ensure the starting of the reaction under otherwise favourable conditions. The source terms for the reaction product and air are obtained easily from

$$Q_{\mathrm{ox}} = r_{\mathrm{fu}} Q_{\mathrm{fu}} \tag{2.96}$$
$$Q_{\mathrm{pr}} = -(1 + r_{\mathrm{fu}}) Q_{\mathrm{fu}} \tag{2.97}$$

Setting a lower limit $\phi_{\mathrm{pr}_{\mathrm{min}}}$ is a relatively safe operation, because the reaction still needs both fuel and oxidant to start, and the true mass fraction exceeds that of the lower limit almost immediately. The other alternative would be to employ an initial small value for the reaction product mass fraction either in the fuel stream or in the oxidant stream. This approach, however, does not sound too attractive, because it would actually require modified boundary conditions.

2.4 Discretization of the Physical Model

So far, we have examined the governing equations for the flow of a reactive mixture of gases, i.e. Eqs. (2.1)–(2.8), and we have investigated some models for the unknown terms in the equations. Since no general solution exists, there are basically two different ways from which to choose. One can investigate a sufficiently simplified problem for which an analytic solution might exist, or one has to discretize the equations and try to solve the resulting system of equations. In this work, the latter approach is followed.

When discretizing the conservation equations, the basic idea is to obtain numerical expressions for the derivatives and other terms in the equations. There are several ways to discretize the equations, and in computational fluid dynamics (CFD) the most common ways are the finite volume method (FVM), the finite difference method (FDM), and the finite element method (FEM).

In the finite element method, the unknown variables are expressed as a weighted sum of all the values at the grid nodes. For a fixed geometry, $\Phi(x, y, z, t)$ is obtained from

$$\Phi(x, y, z, t) = \sum_{\mathrm{elements}} N_i(x, y, z)\, \Phi_i(t) \tag{2.98}$$

where Φ represents any general variable, $N_i(x, y, z)$ and $\Phi_i(t)$ are the shape function and general variable value associated with node i, respectively. The form of the shape functions is not predetermined from a methodological point of view, except that the value of N_i has to be unity at node i, and it has to vanish at any other node.

When constructing the system of equations in the finite element method, the differential equations are multiplied by arbitrary weight functions W, and integrated over the whole domain. Then the approximation for Φ is inserted into the integrated equations, and a system of algebraic equations is obtained. The idea is to search for a solution that satisfies the differential equations in an integral sense, thus posing weaker differentiability conditions on the solution. Therefore, this formulation is also known as the weak formulation, as opposed to the strong formulation, which is based on the differential equations. Since the finite element method is not employed in this work, it will not be discussed any further.

The finite difference method is based on the idea of replacing all the derivatives in the differential equations with difference expressions in terms of the values of Φ at the nodes. The difference formulas are derived from Taylor series expansions of Φ around the point under investigation. FDM was at first the most popular one in CFD, and as a consequence, a lot of the terminology employed in the FVM is inherited from the FDM community. The final equations solved with FDM are actually almost exactly the same as those solved with FVM.

Because the solver employed in this work is based on the finite volume method, FDM will not be discussed any further. Some finite difference terminology, however, will appear in the text. The following discussion describes both the present implementation, and FVM in general.

2.4.1 Finite Volume Form and Discretization of the Fluxes

In the finite volume method, the basic idea is to fulfil the principle of conservation stated by the governing equations. Therefore, the conservation equations are first cast in an integral form, sometimes also referred to as a weak form, and for an arbitrary fixed region V with a boundary S the equations are

$$\frac{\mathrm{d}}{\mathrm{d}t}\int_V U\,\mathrm{d}V + \int_S \vec{F}(U)\cdot\mathrm{d}\vec{S} = \int_V Q\,\mathrm{d}V \tag{2.99}$$

where U is the vector of conservative variables, $\vec{F}(U)$ is the flux vector, and Q is the source term. Performing the integrations for a computational cell i yields

$$V_i\frac{\mathrm{d}U_i}{\mathrm{d}t} = \sum_{\text{faces}} -S\hat{F} + V_iQ_i \tag{2.100}$$

where S is the area of the cell face, and the sum is taken over the faces of the computational cell. Each face has a unit normal vector $\vec{n}$ defined by

$$\vec{n} = n_x\vec{i} + n_y\vec{j} + n_z\vec{k} = \frac{S_x}{S}\vec{i} + \frac{S_y}{S}\vec{j} + \frac{S_z}{S}\vec{k} \tag{2.101}$$

where n_x, n_y, and n_z are the x, y and z-components of $\vec{n}$, respectively, and S_x, S_y and S_z are the respective components of the cell face area. The flux for each face is defined by

$$\hat{F} = n_x(F - F_\mathrm{v}) + n_y(G - G_\mathrm{v}) + n_z(H - H_\mathrm{v}) = n_i\left(F_i - F_{\mathrm{v}_i}\right) \tag{2.102}$$

Here F, F_v, G, G_v, H and H_v are the inviscid and viscous fluxes in the x, y and z-directions, respectively. Using tensor notation with two-equation turbulence models in mind, F_i is given by

$$F_i = \begin{pmatrix} \rho u_i \\ \rho u u_i + \delta_{1i}\left(p + \frac{2}{3}\rho k\right) \\ \rho v u_i + \delta_{2i}\left(p + \frac{2}{3}\rho k\right) \\ \rho w u_i + \delta_{3i}\left(p + \frac{2}{3}\rho k\right) \\ (\rho E + p + \frac{2}{3}\rho k) u_i \\ \rho k u_i \\ \rho \psi u_i \\ \rho \phi u_i \end{pmatrix} \tag{2.103}$$

and the corresponding viscous flux F_{v_i} is

$$F_{\mathrm{v}_i} = \begin{pmatrix} 0 \\ \tau_{1i} + \delta_{1i}\frac{2}{3}\rho k \\ \tau_{2i} + \delta_{2i}\frac{2}{3}\rho k \\ \tau_{3i} + \delta_{3i}\frac{2}{3}\rho k \\ u_k\left(\tau_{ik} + \delta_{ik}\frac{2}{3}\rho k\right) - q_i \\ \mu_k(\partial k/\partial x_i) \\ \mu_\psi(\partial \psi/\partial x_i) \\ \mu_\phi(\partial \phi/\partial x_i) \end{pmatrix} \tag{2.104}$$

In the above, τ and q denote the sum of the molecular and turbulent diffusion defined by Eqs. (2.4), (2.39) and (2.82). The total internal energy ρE is now obtained from

$$\rho E = \rho e + \frac{1}{2}\rho u_i u_i + \rho k \tag{2.105}$$

Eq. (2.100) illustrates the basic idea of the finite volume method: to fulfil conservation. Also, it is obvious that in a finite volume formulation, the important issue is to obtain accurate expressions for the flux $\hat{F}$. We could note here that actually, as defined by Eq. (2.100), $\hat{F}$ is of type flux density, and the flux is $S\hat{F}$. It is, however, common practice to drop the attribute "density" from the name and simply use the word flux for $\hat{F}$. From this point on, this practice is followed. Discretization of the temporal derivative $\mathrm{d}U_i/\mathrm{d}t$ is discussed later.

Inviscid Fluxes

The solver employed in this study is designed for compressible flows. For such solvers, proper upwinding is necessary to stabilize the scheme. In this case, a locally one-dimensional Riemann problem is solved with Roe's method [47] on each cell face to determine the inviscid fluxes. The flux is calculated as

$$\hat{F} = T^{-1}F(TU) \tag{2.106}$$

where T is a rotation matrix that transforms the dependent variables to a local coordinate system normal to the cell surface. In this way, only the Cartesian form F of the flux is needed. This is calculated from

$$F(U^{\mathrm{l}}, U^{\mathrm{r}}) = \frac{1}{2}\left[F(U^{\mathrm{l}}) + F(U^{\mathrm{r}})\right] - \frac{1}{2}\sum_{k=1}^{K} r^{(k)}|\lambda^{(k)}|\alpha^{(k)} \tag{2.107}$$

where U^{l} and U^{r} are the solution vectors evaluated on the left and right sides of the cell surface, $r^{(k)}$ the right eigenvector of the Jacobian matrix $A = \partial F/\partial U = R\Lambda R^{-1}$, the corresponding eigenvalue is $\lambda^{(k)}$, and $\alpha^{(k)}$ is the corresponding characteristic variable obtained from $R^{-1}\Delta U$, where $\Delta U = U^{\mathrm{r}} - U^{\mathrm{l}}$. The vectors U^{l} and U^{r} are evaluated with the MUSCL scheme together with the van Albada limiter. Details of the implementation are found from Refs. [14, 17].

Viscous Fluxes

Discretization of the viscous fluxes does not cause any special stability problems. Instead, the viscous fluxes can be discretized in a very straightforward manner using central differences. There are several ways of deriving expressions for the viscous terms, and depending on the selected starting point, somewhat different expressions may be derived. In the present solver, the gradient of any general variable ϕ on the cell surface $i + 1/2$ is approximated with

$$\nabla\phi|_{i+1/2} = \frac{\phi_{i+1} - \phi_i}{d_{i+1/2}}\vec{n}_{i+1/2} \tag{2.108}$$

where $d_{i+1/2}$ is the distance between the centre-points of the cells i and $i + 1$, and $\vec{n}_{i+1/2}$ is the normal vector of the cell face between the cells i and $i + 1$ defined by Eq. (2.101).

Simulation of Rotational Flows

In the simulations of the flow past the rotating artillery projectile to be described later in this work, the method developed by Siikonen and Pan [48] is employed for the effects of a rotating system of coordinates. The implementation is practically unchanged from the original implementation, and therefore only the associated theory is repeated here briefly.

The basic idea is to employ Cartesian velocity components in a fixed frame of reference, and to let the grid rotate about the axis of rotation. The flow equations need only small modifications for rotational geometries. Assuming rotation around the x-axis, the Navier–Stokes equations need additional source terms for the y and z-momentum equations, and also the convective speed associated with the fluxes has to be rewritten. Denoting the angular velocity with $\vec{\Omega}$, the velocity of a point in the grid is $\vec{\Omega} \times \vec{r}$. The grid velocities have to be subtracted from the inertial velocities when evaluating the convective speeds in the fluxes. In the energy flux, however, the work done by pressure is pressure p multiplied by the inertial velocity $\vec{V}$, not the relative velocity. As a result, the inviscid parts of the fluxes in the y and z-directions are written as

$$G = \begin{pmatrix} \rho\hat{v} \\ \rho u\hat{v} \\ \rho v\hat{v} + p + \frac{2}{3}\rho k \\ \rho w\hat{v} \\ (\rho E + \frac{2}{3}\rho k)\hat{v} + pv \\ \rho k\hat{v} \\ \rho\psi\hat{v} \\ \rho\phi\hat{v} \end{pmatrix} \qquad H = \begin{pmatrix} \rho\hat{w} \\ \rho u\hat{w} \\ \rho v\hat{w} \\ \rho w\hat{w} + p + \frac{2}{3}\rho k \\ (\rho E + \frac{2}{3}\rho k)\hat{w} + pw \\ \rho k\hat{w} \\ \rho\psi\hat{w} \\ \rho\phi\hat{w} \end{pmatrix} \tag{2.109}$$

where $\hat{v} = v - v_{\mathrm{rot}}$, $\hat{w} = w - w_{\mathrm{rot}}$, $v_{\mathrm{rot}} = -\mathbf{\Omega}z$ and $w_{\mathrm{rot}} = \mathbf{\Omega}y$. The contributions of rotation to the flux terms depend only on the geometry and the angular velocity, and they can therefore be precalculated and stored as separate arrays.

The source terms for the momentum equations due to rotation of the grid are $-\vec{\mathbf{\Omega}} \times \rho\vec{V}$, which in this case reduces to

$$Q_{\mathrm{rot}} = (\,0 \quad 0 \quad \mathbf{\Omega}\rho w \quad -\mathbf{\Omega}\rho v \quad 0 \quad 0 \quad 0 \quad 0\,)^T \tag{2.110}$$

The source term Q_{rot} is a direct consequence of the rotation of the grid. The time derivative of a vector $\vec{V}$ in an inertial frame of reference $\mathrm{d}/\mathrm{d}t\,\vec{V}$ expressed in terms of the derivative in a rotating coordinate system $\delta/\delta t\,\vec{V}$ is [49, p. 56]

$$\frac{\mathrm{d}}{\mathrm{d}t}\vec{V} = \frac{\delta}{\delta t}\vec{V} + \vec{\mathbf{\Omega}} \times \vec{V} \tag{2.111}$$

where $\vec{\mathbf{\Omega}}$ is the angular velocity of the rotating coordinate system.

Special Treatment of the Inviscid Fluxes in the Circumferential Direction

For the axially symmetric flows to be simulated later on in this work, a special simplified flux-treatment for the circumferential direction was developed. Due to the axisymmetric nature of the flows, the gradient of any scalar variable in the circumferential direction vanishes. Therefore, assuming x-axis is the axis of rotation, it is unnecessary to calculate the circumferential fluxes of ρ, ρu, ρE, ρk, $\rho\psi$ and $\rho\phi$. The necessary terms for the inviscid fluxes of ρv and ρw are

$$F_{3_{k\pm1/2}} = \dot{m}_A\, v_{k\pm1/2} + p\, n_{y_{k\pm1/2}} \tag{2.112}$$

$$F_{4_{k\pm1/2}} = \dot{m}_A\, w_{k\pm1/2} + p\, n_{z_{k\pm1/2}} \tag{2.113}$$

where $\dot{m}_A$ is the mass flow rate per unit area in the circumferential direction

$$\dot{m}_A = \frac{1}{2}\rho\left[(v_k - v_{\mathrm{rot}_k})(n_{y_{k+1/2}} + n_{y_{k-1/2}}) + (w_k - w_{\mathrm{rot}_k})(n_{z_{k+1/2}} + n_{z_{k-1/2}})\right] \tag{2.114}$$

When considering the flows simulated in this work, there is only one computational cell in the circumferential direction, and k in Eqs. (2.112) through (2.114) could be replaced with 1.

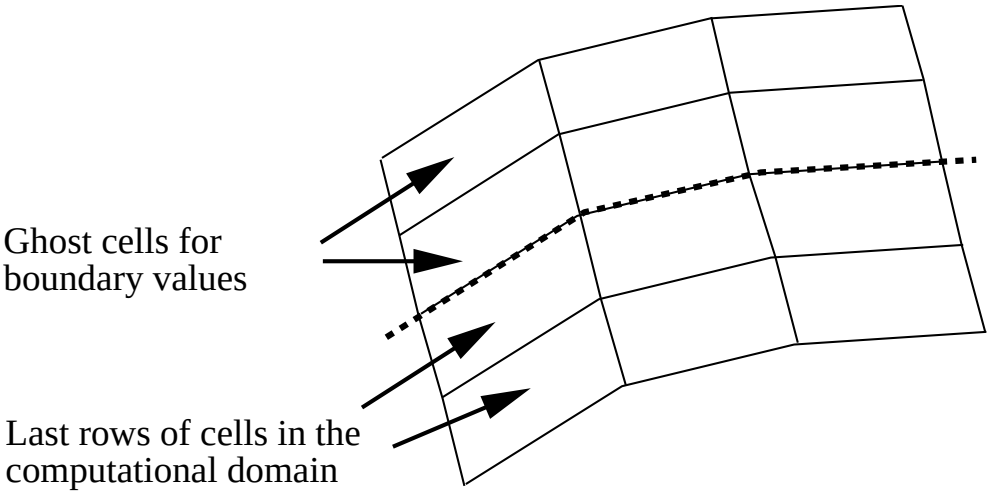

Fig. 2.1: The ghost cells located outside the computational domain are for the specification of the boundary conditions.

2.4.2 Boundary Conditions

For the finite volume formulation of Eq. (2.100), we should note that the solution of $\mathrm{d}U_i/\mathrm{d}t$ depends on the fluxes over the surfaces $S_{i\pm1/2}$, which in general also depend on $U_{i\pm1}$. On the other hand, there is no requirement that $\hat{F}_{i+1/2}$ should always depend on both U_i and U_{i+1}. The flux just has to be determined somehow. Therefore, it makes sense to argue that the boundary condition for a finite volume method is a given flux at the boundary. For the practical implementation, however, usually two extra rows of cells are allocated for the definition of the boundary conditions, as shown in Figure 2.1. These ghost cells are utilized for storing block-to-block connectivity in order to ensure continuous solutions over block boundaries, and they are, at least in the present case, employed for specifying the free-stream boundary conditions.

For a well posed problem, the boundary conditions need to be defined appropriately. In external flows, like flow past a wing, the obvious free-stream boundary condition is to fix the flow variables. Nevertheless, this can also be a misleading definition, because free stream is easily interpreted as the far-field boundary, which again includes also the wake. In the wake, however, there is no justification for a fixed boundary condition. Fortunately, the downstream boundary conditions tend to have only a small effect on the solution of an external flow field, as far as the boundary is sufficiently far away from the body.

For internal flows, like flows in a channel, there may exist detailed knowledge of the flow conditions at the inflow boundaries, but very often the available data is limited to some integrated information, like mass flow rate, average temperature etc. Even if the mean flow characteristics are fairly well known, for practical flow cases, the details of turbulence are usually unknown. In internal flows, the specification of the outflow conditions is a contradictory matter: How could one know in advance what is going to flow out from the flow field, when the whole problem is to determine what happens inside the flow field?

Free-Stream and Solid Surface Boundaries

In the present implementation, the boundary conditions are treated as follows: At the free-stream boundary, as far as the specified free-stream velocity is directed into the computational domain, the values of the dependent variables are kept as constants. On the other hand, if the free-stream velocity is directed out from the computational domain, the pressure p is fixed to its free-stream value and all the other dependent variables are extrapolated.

In the calculation of the inviscid parts of the fluxes at the solid wall boundaries, the flux-difference splitting is not used. Since the convective speed is equal to zero on the solid surfaces, the only contribution to the inviscid surface fluxes arises from the pressure terms in the momentum equations. A second-order extrapolation is applied for the evaluation of the wall pressure as

$$p_{\mathrm{w}} = \frac{3}{2}p_1 - \frac{1}{2}p_2 \tag{2.115}$$

where the subscript w refers to conditions on the wall, and 1 and 2 refer to the centre of the first and second cell from the surface, respectively. A similar formula is used for the diffusion coefficients on the wall.

The viscous fluxes on the solid surfaces are obtained by setting $\vec{V}_{\mathrm{w}} = 0$, or $\vec{V}_{\mathrm{w}} = \vec{V}_{\mathrm{moving}}$ if the wall is moving. At the walls, the central expression of the viscous terms is replaced by a second-order one-sided formula.

$$\frac{\partial \phi}{\partial y_{\mathrm{n}}} = \frac{-8\phi_{\mathrm{w}} + 9\phi_1 - \phi_2}{3d_{\mathrm{w}}} \tag{2.116}$$

where d_{w} is the thickness of the first cell above the surface.

Inlet Boundaries

In numerical simulations, an inlet boundary is such from which the flow enters the computational domain. An inlet boundary should be placed so that the flow conditions at that boundary are as easy as possible to define reliably. For that reason, the computational domain of the base-bleed projectile studied in this work is extended to the inside of the base-bleed unit, and the burning surface of the propellant is treated as an inlet. In the bluff-body stabilized flame case only the fuel jet is treated as an inlet.

For the surface of the base-bleed unit, a special treatment for the fluxes had to be developed in this work. On the burning surface of the unit, hot gas enters the flow field from a solid surface, which may be rotating. The basic specification of the flow conditions is carried out as explained in Ref. [50]. The mass flow rate per area $\dot{m}_A$, the stagnation temperature T_0, turbulence level Tu and turbulent viscosity μ_T/μ are fixed by the user, and for a subsonic inlet the static pressure is extrapolated from the flow field. The stagnation temperature is converted to specific total enthalpy H, and the boundary conditions become

$$\begin{cases} \dot{m}_A &= \rho V \\ H(T_0) &= h + \frac{1}{2}V^2 + k \\ Tu &= \sqrt{2k/3V^2} \\ \mu_T &= 0.09\dfrac{(\rho k)^2}{\rho\epsilon} = \dfrac{\rho k}{\omega} \\ p &= p_{\text{inlet}} \end{cases} \tag{2.117}$$

In order to differentiate between a subsonic or supersonic inlet, the following condition is applied:

$$p_{\text{inlet}} = \max\left(p_{\text{field}}\ ,\ \frac{\dot{m}_A}{\gamma}\sqrt{\frac{2H(T_0)(\gamma-1)}{\gamma+1}}\right) \tag{2.118}$$

For a calorically perfect gas, the solution of Eq. (2.117) with respect to the primitive variables is

$$\rho = \frac{\sqrt{(\gamma p)^2 + 2\dot{m}_A^2 H(\gamma-1)^2(1+3Tu^2)} + \gamma p}{2H(\gamma-1)} \tag{2.119}$$

$$V = \frac{\dot{m}_A}{\rho} \tag{2.120}$$

$$T = \frac{p}{\rho R} \tag{2.121}$$

$$\rho k = \frac{3}{2}\rho\, Tu^2\, V^2 \tag{2.122}$$

$$\rho\epsilon = 0.09\frac{(\rho k)^2}{\mu_T} \tag{2.123}$$

$$\rho\omega = \rho\frac{\rho k}{\mu_T} \tag{2.124}$$

If the gas is not perfect, the iterative scheme presented in Ref. [50] is employed with the above solution as a starting point.

Improved Method for the Inlet Boundaries

So far, the above discussion has nothing to do with rotation. When the inlet surface is rotating, as in the case of the rotating base-bleed unit, Eqs. (2.119)–(2.124) are employed as such, but the velocity is corrected with an additional velocity due to rotation $\vec{\Omega} \times \vec{r}$. This way, the boundary condition specification is interpreted as specified in the coordinate system fixed to the rotating surface.

The interesting part is that, except for the rotation of the base-bleed unit, the above scheme has been successfully employed in several studies [18, 22, 50] for determining the boundary values in the ghost cells of a base-bleed unit. In those studies, the standard flux-difference splitting scheme was employed on the inlet

surfaces together with the appropriately defined boundary values. This time, when employed for a grid clustered for boundary-layer modelling purposes, the numerical algorithm became unstable. The solution to this stability problem was to explicitly specify the fluxes based on Eqs. (2.119)–(2.124) together with the viscous terms as usual on a solid surface, except for the contributions of the pressure. The changes of pressure due to the multigrid method were accounted for when evaluating the fluxes on the solid surface inlets, and this way the scheme became stable.

These stability problems are quite evidently a problem tied to the employed solution method with a multigrid scheme. Nevertheless, such problems have not been encountered in any of the previous simulations employing the "standard" ghost-cell value approach. The present scheme turned out to be more robust than the previous standard approach, and, as suggested earlier, the boundary condition is now set by defining the flux.

2.5 Solution of the Discretized Equations

2.5.1 Discretization of the Temporal Derivative

The derivative with respect to time in Eq. (2.100) can be discretized with a difference expression like

$$\frac{\mathrm{d}U_i}{\mathrm{d}t} \approx \frac{U^{n+1} - U^n}{\Delta t} \tag{2.125}$$

which has second-order accuracy at time-level $t^n + 1/2\Delta t$, but first-order at time-levels t^n and t^{n+1}. The superscripts n and $n+1$ refer to the current (known) and the next (unknown) time-levels, respectively. For a steady-state solution, the numerical accuracy of this term is not important, and Eq.(2.125) may be employed without worries. Even though the term could basically be left out when searching for a steady-state solution, this approach is not practical, because, in a general case, the nonlinearities in the equations to be solved make it impossible to obtain a direct solution. Therefore, a time-marching approach is the normal way also for steady-state solutions.

For an explicit method, the fluxes and source terms are evaluated on time-level t^n, and U^{n+1} can be calculated explicitly. For an implicit method, they are linearized around time-level n with respect to U and the following equation is obtained

$$V\frac{U^{n+1} - U^n}{\Delta t} = V\frac{\Delta U}{\Delta t} = R^n + \frac{\partial R}{\partial U}\Delta U \tag{2.126}$$

where the subscript i has been dropped and R is used as shorthand for the right-hand side of Eq. (2.100), i.e. the residual. Moving terms involving ΔU to the left-hand side and all the rest to the other side, an equation for ΔU is obtained

$$\left(1 - \frac{\Delta t}{V}\left[\frac{\partial R}{\partial U}\right]\right)\Delta U = \frac{\Delta t}{V}R^n = \Delta U^{\mathrm{e}} \tag{2.127}$$

where ΔU^{e} is shorthand for the explicit change of U. Eq. (2.127) is a matrix equation for ΔU. For a steady-state solution, assuming one exists, Eq. (2.127) may be used as a basis for a time-marching solution method. The solution procedure for ΔU may involve any numerical convergence acceleration techniques available, because when a steady state is reached, the residuals vanish, and consequently also ΔU vanishes.

2.5.2 Solution Algorithm

As mentioned before, direct inversion of the matrix $I - (\Delta t/V)[\partial R/\partial U]$ is not feasible due to the huge size of the matrix in any practical case. However, with approximate factorization the matrix inversion can be replaced with three successive inversions of a block-tridiagonal matrix. Even though the factorization reduces the numerical accuracy of the temporal discretization, it facilitates a relatively fast solution method. The solution algorithm may be further enchanced by local time-stepping, which means that the time-step sizes vary locally based on stability criteria. Such a method is called pseudo-time integration due to the varying time-step sizes.

The solution method employed in this work was developed by Siikonen [14, 15, 51, 52], and it is briefly described here. Only the changes caused by the newly implemented reaction model are explained in detail. The basic solution algorithm is implicit pseudo-time integration applying the Diagonally Dominant ADI-factorization (DDADI) [53]. It is based on approximate factorization and on the splitting of the Jacobians of the flux terms. The resulting implicit stage consists of a backward and forward bidiagonal sweep in every computational coordinate direction plus a matrix multiplication. The sweeps are based on a first-order upwind differencing. In addition, the linearization of the source term is factored out of the spatial sweeps.

The boundary conditions for the implicit sweeps are set explicitly to zero. After factorization, the implicit stage can be written as

$$\begin{aligned}
\left[I + \frac{\Delta t_i}{V_i}(\partial_i^- S_{i+1/2} A_i^+ - \partial_i^+ S_{i-1/2} A_i^-)\right] \quad &\times \\
\left[I + \frac{\Delta t_j}{V_j}(\partial_j^- S_{j+1/2} B_j^+ - \partial_j^+ S_{j-1/2} B_j^-)\right] \quad &\times \\
\left[I + \frac{\Delta t_k}{V_k}(\partial_k^- S_{k+1/2} C_k^+ - \partial_k^+ S_{k-1/2} C_k^-)\right] \quad &\times \\
\Big[I - \Delta t_i D_i\Big]\Delta U_i \quad &= \quad \frac{\Delta t_i}{V_i} R_i^{\mathrm{e}}
\end{aligned} \tag{2.128}$$

where I is an identity matrix, $\partial^-_{i,j,k}$ and $\partial^+_{i,j,k}$ are first-order spatial difference operators in the i, j and k-directions, A, B and C are the corresponding Jacobian matrices, $D = \partial Q/\partial U$, and R_i^{e} is the right-hand side of Eq. (2.100). The Jacobians are calculated as

$$A^{\pm} = R(\Lambda^{\pm} \pm kI)R^{-1} \tag{2.129}$$

where R is the eigenvector matrix of A, and $\Lambda^{\pm}$ are diagonal matrices containing the positive and negative eigenvalues, and k is a factor to ensure the stability of the viscous term. More details about the basic implicit solution method can be found in Refs. [15, 19].

In order to accelerate convergence, a multigrid method is employed. The multigrid cycling employs a V-cycle and is based on the method by Jameson [54]. The details of the implementation are found in Ref. [55]. The details have not changed notably since the original implementation, as explained in Ref. [19].

Changes Caused by the Reaction Model

As explained above, the implicit sweeps invert a block-tridiagonal matrix. In detail, the changes in the conservative variables ΔU are first transformed to changes in primitive variables ΔV, which are further converted to changes in contravariant characteristic variables δW. In the first transformation, it is implicitly assumed that the total internal energy is ρE treated as sensible energy. Therefore, to make the old scheme work, ρE and $\Delta(\rho E)$ are modified with

$$\rho E \rightarrow \quad \rho E - \sum_i \rho\phi_i \, h_{0,i}^{T=0} \quad = \rho E_\mathrm{s} \tag{2.130}$$

$$\Delta(\rho E) \rightarrow \quad \Delta(\rho E) - \sum_i \Delta(\rho\phi_i) \, h_{0,i}^{T=0} \quad = \Delta(\rho E_\mathrm{s}) \tag{2.131}$$

where the subscript s stands for sensible. With these formulas, the change in pressure is obtained from

$$\Delta p = \frac{1}{\partial e/\partial p} \left[\Delta e_\mathrm{s} - \frac{\partial e}{\partial \rho} \Delta\rho \right] \tag{2.132}$$

as usual. As explained in Subsection 2.3.2, the whole implementation could have been built on sensible energies. In that case the above problems would never have appeared. On the other hand, the source terms in the energy equations would require special treatment at least comparable in complexity to Eqs. (2.130) and (2.131). Therefore, the present approach was chosen.

The implicit treatment of the chemical source terms is factored out from the spatial sweeps and treated in a separate routine. It is based on linearization of the production of $\rho\phi_i$ with respect to $\rho\phi_i$ only, and the result is

$$\Delta\rho\phi_i = \frac{\Delta(\rho\phi_i)^\mathrm{e}}{1 - \Delta t \, (\partial Q_i / \partial \rho\phi_i)} \tag{2.133}$$

After the implicit sweeps, ρE_s and $\Delta(\rho E_\mathrm{s})$ are converted back to absolute energies.

Also, in order to ensure stability of the time-integration scheme, the time-step size was further limited with the expression

$$\frac{1}{\Delta t_\mathrm{max}} = \frac{2}{CFL} \max\left(\frac{-Q_i}{\max(\rho\phi_i \, , \, \varepsilon)} \, , \, \frac{Q_i}{\max((\rho - \rho\phi_i) \, , \, \varepsilon)} \, , \, \varepsilon \right) \tag{2.134}$$

where ε is a small number to avoid possible division by zero.

2.5.3 Time-Accurate Time-Integration Scheme

The basic time-integration scheme employed for steady-state problems is not accurate in time for several reasons. First of all, the spatially varying time-steps spoil time-accuracy. Secondly, the Jacobians in Eq. (2.128) should be calculated exactly, but still the factorized scheme would remain a first-order scheme. Thirdly, the implicit Euler scheme employed for steady-state problems is of first order accuracy due to the truncation error of Eq. (2.125).

For time-accurate simulations, the idea is to employ second-order one-sided differences for the temporal derivatives, and to express R at time-level t^{n+1}. Following Hoffren's work [56], a time-accurate time-integration scheme was implemented into the present solver by Kaurinkoski *et al.* [57]. In short, the method is based on casting the equations to a form resembling the form of the original steady-state solver as

$$V\left(\frac{3}{2}U^{n+1} - 2U^{n} + \frac{1}{2}U^{n-1}\right) \;=\; \Delta t\left(\sum_{\text{faces}} -S\,\hat{F}^{n+1} + V\,Q^{n+1}\right) \quad (2.135)$$

where the superscripts $n+1$, n and $n-1$ refer to the next, current and previous time-levels, respectively. Again, the direct solution of U^{n+1} from Eq.(2.135) is in practice impossible, and therefore an iterative solution method based on calculating successive corrections to the previous estimate for U^{n+1} is employed. As a result, the solution on the next time-level is obtained after iteration inside a time-step. The equation solved is

$$\left(1 - \frac{\Delta\tau_{\text{mod}}}{V}\left[\frac{\partial R}{\partial U}\right]^{k}\right)\delta U^{k} = \frac{\Delta\tau_{\text{mod}}}{\Delta t}\,\delta U^{k}_{\text{mod}} \quad (2.136)$$

where τ is a local time-step based on stability criteria for the steady-state pseudo-time integration method, and $\Delta\tau_{\text{mod}} = \Delta\tau\Delta t/(\Delta t + \Delta\tau)$ is a modified time-step. We can see that Eq. (2.136) is exactly of the same form as Eq. (2.127) solved with the steady-state pseudo-time integration method. Only the time-step is modified and the right-hand side is multiplied by the factor $\Delta\tau_{\text{mod}}/\Delta t$. Hence, the existing steady-state solver with all the modifications presented in this text may be employed for obtaining the solutions, as far as the necessary changes to the time-integration scheme are made.

3 Application of the Chemical Reaction Model

The reaction model employed in this work was outlined in the previous chapter. The thermo-chemical details of the investigated problems are described here, and all the employed model constants are given. The model is first validated by simulating an axisymmetric bluff-body stabilized flame, which has been investigated both experimentally [29] and numerically [29, 30] by other groups. After that, the model is employed for the final combustion of a fuel-rich base-bleed propellant.

3.1 Axisymmetric Bluff-Body Stabilized Flame

In the experiments carried out by Correa and Gulati [29], the fuel in the reaction was a mixture consisting of 27.5% CO/32.3% H_2/40.2% N_2. Modelling air with 21% O_2/79% N_2 results in a global reaction

$$0.275\ \mathrm{CO} + 0.323\ \mathrm{H_2} + 0.402\ \mathrm{N_2} + r_{\mathrm{st}}^{\mathrm{mol}}(0.21\ \mathrm{O_2} + 0.79\mathrm{N_2}) \longrightarrow \quad (3.1)$$
$$0.275\ \mathrm{CO_2} + 0.323\ \mathrm{H_2O} + (0.402 + 0.79 r_{\mathrm{st}}^{\mathrm{mol}})\ \mathrm{N_2}$$

where $r_{\mathrm{st}}^{\mathrm{mol}} = 1.42$ is the molar stoichiometric coefficient, the value of which is determined based on the oxygen consumption. The composition and model parameters of the fuel for Eq. (2.84) are shown in Table 3.1. The same data for the reaction product is found from Table 3.2.

Table 3.3 shows the composition and model parameters for air, and the actual model parameters employed in the simulations. As can be seen, air is modelled as a calorically perfect gas to allow smooth transition between initial computations without any reactions and the reactive flow field simulations. The model parameters are chosen to represent air with $\gamma = 1.4$ and $R = 287.05$ J/kg. This same selection concerning the modelling of air was also adopted when simulating the artillery projectile.

For the same initialization reason, the heats of formation were tailored to produce the same net change in the heat of formation as with the original values, but with zero heats of formation for the reactants. In other words, regardless of the origin of the heat of reaction, it is faked to be completely built from the product's contribution. Therefore, after transforming the data given for $H_0^{T=25^\circ\mathrm{C}}$ in Tables

Table 3.1: The composition and model parameters of the fuel in the bluff-body stabilized flame. $H_0^{T=25^\circ\mathrm{C}}$ is the heat of formation per mole at $T = 25^\circ\mathrm{C}$. Values for A, B, C and D are given on a per mole basis.

	$\mathcal{M}$	X	ϕ	A	B	C	D	$H_0^{T=25^\circ\mathrm{C}}$
CO	28.010	0.275	0.393	30.962	2.439	-0.280	0.0	-110528
H_2	2.020	0.323	0.033	26.882	3.586	1.050	0.0	0.0
N_2	28.020	0.402	0.574	30.418	2.544	-0.238	0.0	0.0
Mix	19.619	1.000	1.000	29.425	2.852	0.166	0.0	-30395

Table 3.2: The composition and model parameters of the reaction product in the bluff-body stabilized flame. $H_0^{T=25^\circ\mathrm{C}}$ is the heat of formation per mole at $T = 25^\circ\mathrm{C}$. Values for A, B, C and D are given on a per mole basis.

	$\mathcal{M}$	X	ϕ	A	B	C	D	$H_0^{T=25^\circ\mathrm{C}}$
CO_2	44.010	0.130	0.200	51.128	4.368	-1.469	0.0	-393521
H_2O	18.020	0.153	0.096	34.376	7.841	-0.423	0.0	-241856
N_2	28.020	0.718	0.704	30.418	2.544	-0.238	0.0	0.0
Mix	28.571	1.000	1.000	33.711	3.589	-0.426	0.0	-87978

3.1, 3.2 and 3.3 with Eq.(2.86), we can write the modified heat of formation of the product as

$$H_{0_{\mathrm{pr\,mod}}}^{T=0} = H_{0_{\mathrm{pr}}}^{T=0} - \sum_{\mathrm{reactants}} \frac{\nu_i'}{\nu_{\mathrm{pr}}''} H_{0_i}^{T=0} \tag{3.2}$$

where ν_i' is the stoichiometric coefficient of reactant i, and ν_{pr}'' is the stoichiometric coefficient of the product. The final value of $H_{0_{\mathrm{pr\,mod}}}^{T=0}$ employed for the reaction described by Eq.(3.1) is $-72\,289$ J/mol. As mentioned earlier, the mole-based coefficients are transformed to mass-based values simply by division by the respective molar masses.

The stoichiometric coefficient r_{fu} employed in the mass-based global reaction Eq.(2.91) is obtained by multiplying the molar stoichiometric coefficients by the respective molar masses and then dividing the mass-based coefficients by the mass-based coefficient of the fuel mixture. As a result, the final value $r_{\mathrm{fu}} = 2.094$ is obtained.

3.2 Partially Burned Base-Bleed Propellant

When modelling the chemical reactions of the base-bleed gas, a number of simplifications are made. First of all, the bled gas, which is partially burned when flowing

Table 3.3: The composition and model parameters of air according to the selected thermodynamics model, and the way it was approximated. $H_0^{T=25^\circ\mathrm{C}}$ is the heat of formation per mole at $T = 25^\circ\mathrm{C}$. Values for A, B, C and D are given on a per mole basis.

	$\mathcal{M}$	X	ϕ	A	B	C	D	$H_0^{T=25^\circ\mathrm{C}}$
O_2	31.999	0.210	0.233	29.154	6.477	-0.184	-1.017	0.0
N_2	28.020	0.790	0.767	30.418	2.544	-0.238	0.0	0.0
`Mix`	28.856	1.000	1.000	30.153	3.370	-0.227	-0.214	0.0
`Model`	28.965	1.000	1.000	29.100	0.0	0.0	0.0	0.0

Table 3.4: The composition and model parameters of the bled partially burned propellant [58]. $H_0^{T=25^\circ\mathrm{C}}$ is the heat of formation per mole at $T = 25^\circ\mathrm{C}$. Values for A, B, C and D are given on a per mole basis.

	$\mathcal{M}$	X	ϕ	A	B	C	D	$H_0^{T=25^\circ\mathrm{C}}$
CO	28.010	0.260	0.337	30.962	2.439	-0.280	0.0	-110528
H_2O	18.020	0.232	0.194	34.376	7.841	-0.423	0.0	-241856
H_2	2.020	0.230	0.021	26.882	3.586	1.050	0.0	0
HCl	36.461	0.145	0.244	26.527	4.602	0.109	0.0	-92307
N_2	28.020	0.076	0.098	30.418	2.544	-0.238	0.0	0
CO_2	44.010	0.050	0.101	51.128	4.368	-1.469	0.0	-393521
H	1.010	0.005	0.000	20.786	0.000	0.000	0.0	217965
Cl	35.453	0.002	0.004	23.736	-1.284	-0.126	0.0	121294
OH	17.010	0.001	0.001	27.984	3.301	250.0	-0.09	39042
`Mix`	21.606	1.000	1.000	31.069	4.356	0.211	-0.0001	-116474

out from the base-bleed unit, is in reality composed of several species. In this work, however, it is treated as a single species, the properties of which are based on the composition given in Ref. [58]. The composition is shown in Table 3.4.

The details of the reaction are also dropped, and the reaction is modelled as an artificial single-step reaction producing the final reaction product of the burning reaction. The composition of the final product is based on data from Ref. [59] at a final temperature of $T = 600$ K.

The investigated problem in Ref. [59] is to determine the final outcome of the reacting base-bleed gas when the reaction progress is not limited by the amount of oxygen present during the reaction. In these simulations, air is modelled with 21% $O_2/79\%$ N_2, and from the composition of the products it is obvious that the nitrogen N_2 is an inert component in the global reaction. Also, according to the results of Ref. [59], the amount of oxygen consumed is independent of the prescribed final temperature of the reaction environment. Therefore, the global reaction is modelled in this work with a single-step reaction, where the inert part of air (N_2)

Table 3.5: The composition and model parameters of the mixture of totally burned propellant [59] and inert components of air. $H_0^{T=25^\circ\mathrm{C}}$ is the heat of formation per mole at $T = 25^\circ\mathrm{C}$. Values for A, B, C and D are given on a per mole basis.

	$\mathcal{M}$	X	ϕ	A	B	C	D	$H_0^{T=25^\circ\mathrm{C}}$
N_2	28.020	0.544	0.522	30.418	2.544	-0.238	0.0	0.0
H_2O	18.020	0.256	0.158	34.376	7.841	-0.423	0.0	-241856
CO_2	44.010	0.153	0.231	51.128	4.368	-1.469	0.0	-393521
Cl_2	35.453	0.026	0.063	36.610	1.079	-0.272	0.0	0
HCl	36.461	0.021	0.027	26.527	4.602	0.109	0.0	-92307
`Mix`	29.201	1.000	1.000	34.685	4.185	-0.468	0.0	-124207

is transferred to the product side of the reaction without any changes, and all the oxygen in the air is consumed. The composition of the reaction products formed based on these approximations is shown in Table 3.5. The so formed reaction is expressed as

$$1 \text{ mol } \textit{Fuel} + 1.292 \text{ mol } \textit{Air} \longrightarrow 2.017 \text{ mol } \textit{Product} \tag{3.3}$$

or as a mass-based reaction equation

$$1 \text{ kg } \textit{Fuel} + 1.725 \text{ kg } \textit{Air} \longrightarrow 2.725 \text{ kg } \textit{Product} \tag{3.4}$$

Hence, the stoichiometric coefficient to be employed in the EBU model is $r_{\mathrm{fu}} = 1.725$. The heats of formation are manipulated in a similar manner as in the previous section describing the bluff-body stabilized flame. The resulting heat of formation of the reaction product is $H_{0_{\mathrm{pr\,mod}}}^{T=0} = -64\,908$ J/mol.

4 Axisymmetric Bluff-Body Stabilized Flame

In order to validate the implementation of the EBU-reaction model, a test case with a bluff-body stabilized flame is simulated. For the selected test case both experimental [29] and numerical [29, 30] results exist. The case is simulated employing both the $k-\omega$ RCSST and Chien's $k-\epsilon$ turbulence models.

4.1 Experimental Setup and Computational Grid

In the experiments, an axisymmetric flame holder with an outer diameter of $D = 38.1$ mm was placed in a stream of air at a velocity of $V_\infty = 6.5$ m/s. At the centreline was a concentric fuel jet of diameter $d = 3.18$ mm at an average velocity of 80 m/s. The blockage ratio of the bluff body in the tunnel was approximately 5%, based on which we can approximate the outer diameter of the test section with 170.4 mm. Figure 4.1 shows the experimental setup and the main dimensions of the problem. Both the fuel-jet inlet stream and the wind tunnel flow were at a temperature of $T = 300$ K and pressure of $p = 1$ atm $= 101$ kPa.

For the numerical simulations, an orthogonal grid with $80 \times 80 \times 1$ cells in the axial, radial and circumferential directions, respectively, was employed. The fuel-jet inlet was discretized with 16 cells, the bluff-body surface with 32 cells, and the wind tunnel air flow inlet was modelled with 32 cells. The grid is depicted in Figure 4.2. The top-wall of the wind tunnel was treated as an inviscid wall, since it was assumed to have little effect on the jet properties. The boundary conditions for the wind tunnel air flow inlet as well as the outlet from the test-section were specified as free-stream boundaries, i.e. fixed values on the upstream side and extrapolated values with fixed pressure on the downstream side, as explained earlier.

Since the fuel-jet inlet conditions are not described in detail in Ref. [29], the fuel jet was modelled in two different ways: the flow was either assumed to be a bulk flow with constant axial velocity $u = 80$ m/s, or the flow was assumed to be a fully developed pipe flow with an average velocity of $\bar{u} = 80$ m/s. In the figures shown later, the two fuel-jet types are labelled with "Bulk" and "FD", denoting the constant velocity fuel jet and the fully developed fuel jet, respectively. In order to specify the mass flow rate per unit area, as in Eq. (2.117), the velocities were multiplied by the assumed density $\rho = p/RT$, where $T = 300$ K and $p = 101$ kPa. The gas constant was obtained from Eq. (2.22). The average mass flow rate per unit

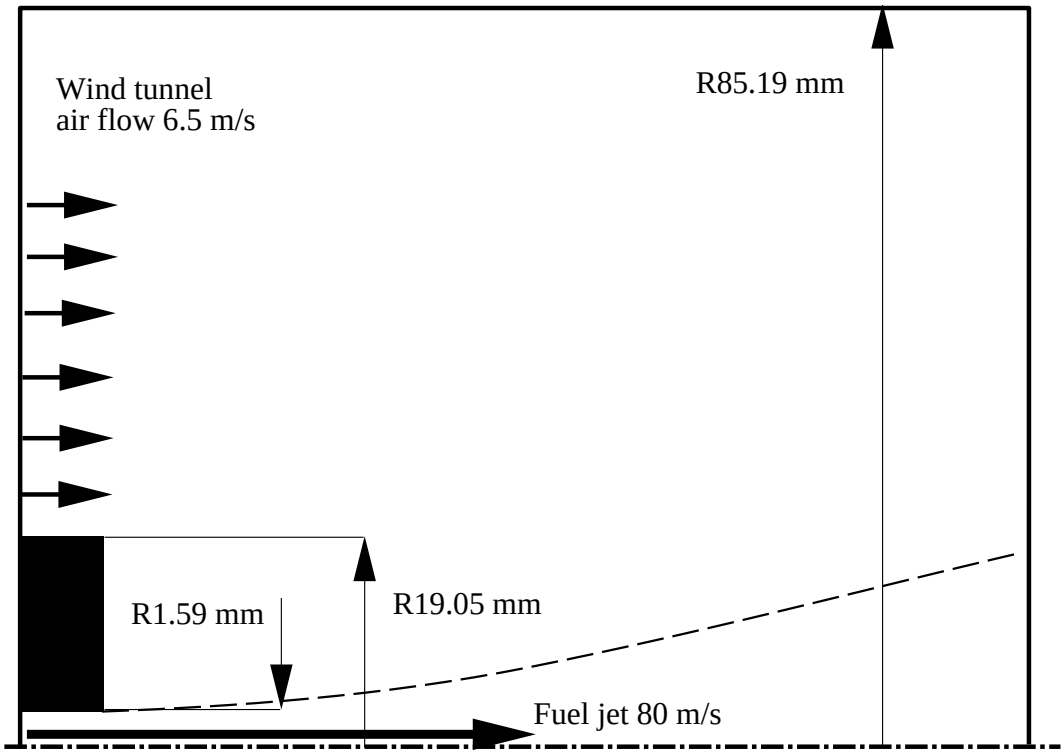

Fig. 4.1: The geometry of the experimental setup.

area was thus set to $\dot{m}_A = 63.76$ kg/(m^{2}s).

With the bulk flow fuel inlet, following the convention of the simulations of Ref. [29], the inlet turbulence kinetic energy was fixed to $k = 0.005\,V^2$, and the turbulence length-scale $l = k^{1.5}/\epsilon$ was set to $0.03\,d$. For the inlet definition scheme presented by Eq. (2.117), the fuel-jet turbulence level was set to 0.057, and the turbulent viscosity was fixed to $\mu_T/\mu = 2.19$.

Both the fully developed inlet and the bulk inlet cases were simulated employing both the $k-\omega$ RCSST and Chien's $k-\epsilon$ turbulence models. The so defined four cases were also simulated as the flow of a non-reacting fuel jet, i.e. inert fuel with unchanged thermodynamic properties, to make comparisons of the jet spreading rates. In all the computed cases, the outflow boundary was treated with a fixed pressure, and a first-order extrapolation for ρ and $\rho\vec{V}$.

When comparing the results, a frequently used quantity is the conservative scalar, denoted here with ξ, which is defined as the mass fraction of fuel, both burned and unburned. Therefore, it is obtained from

$$\xi \equiv \frac{\rho_{\rm fu} + 1/(1+r_{\rm fu})\rho_{\rm pr}}{\rho} = \phi_{\rm fu} + \frac{1}{1+r_{\rm fu}}\phi_{\rm pr} \tag{4.1}$$

With the above definition, ξ is a truly conservative scalar, i.e. there is no net change for ξ due to the source terms. For the reaction under investigation, the stoichiometric value of ξ is

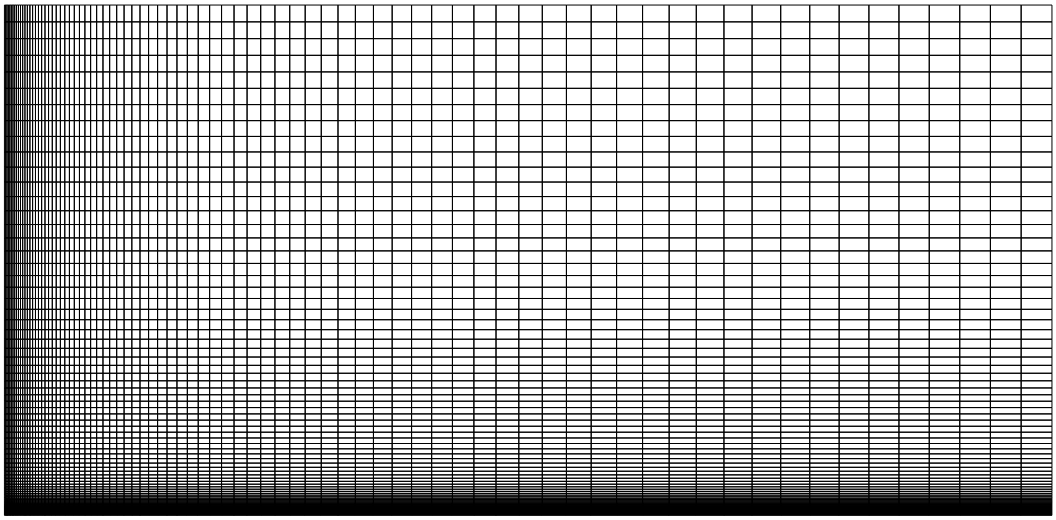

Fig. 4.2: The $80 \times 80 \times 1$ grid employed to model the geometry of the experimental setup.

$$\xi_{\rm st} = \frac{1}{1 + r_{\rm fu}} = 0.3232 \tag{4.2}$$

The jet spreading rates are analyzed by monitoring the scaled velocity profiles of u^* versus r_u^* defined by

$$u^* = \frac{u - u_\infty}{u_{CL} - u_\infty} \tag{4.3}$$

$$r_u^* = \frac{r}{r_{u^*=0.5}} \tag{4.4}$$

where $r_{u^*=0.5}$ is the distance from the x-axis at which $u^* = 0.5$, u_∞ is the velocity on the inviscid top-wall, and u_{CL} is the velocity at the centreline. In all the figures, x is scaled with the diameter of the fuel jet d. Another measure of the jet spreading rate is obtained from the half-width based on the conservative scalar ξ, which gives rise to another definition for r_ξ^*

$$\xi^* = \frac{\xi - \xi_\infty}{\xi_{CL} - \xi_\infty} \tag{4.5}$$

$$r_\xi^* = \frac{r}{r_{\xi^*=0.5}} \tag{4.6}$$

where $r_{\xi^*=0.5}$ is the distance from the x-axis at which $\xi^* = 0.5$, and ξ_∞ is the value of ξ on the top-wall.

4.2 Simulations with the Reacting Fuel Jet

The simulations with the EBU model converged quite slowly. This is most probably due to the thin cells in the circumferential direction near the symmetry axis and the

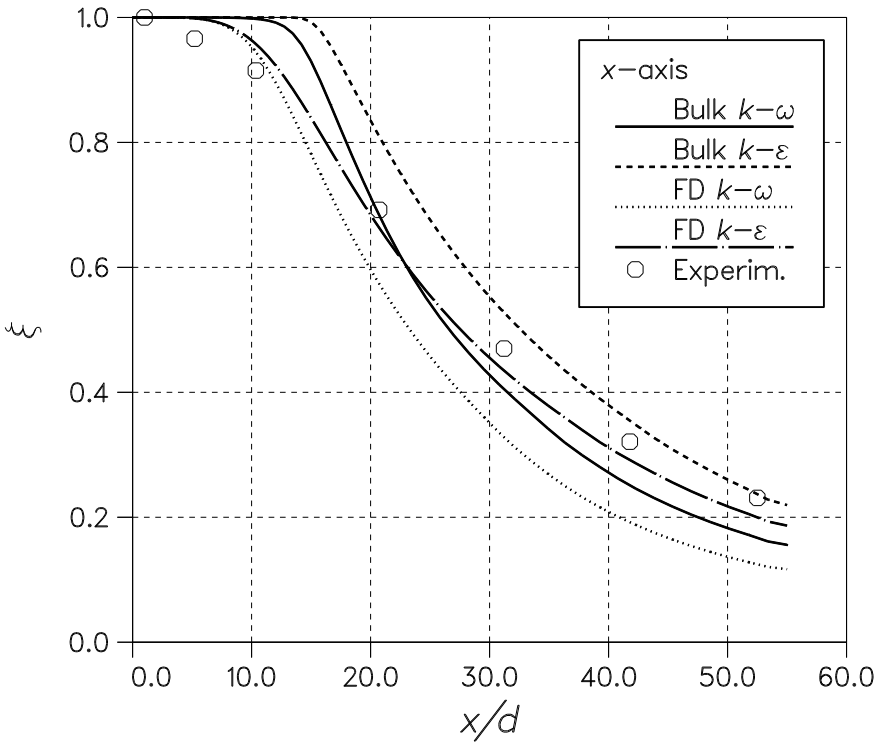

Fig. 4.3: The conservative scalar ξ along the symmetry axis according to the $k-\omega$ model (solid line) and the $k-\epsilon$ model (broken line) with a constant velocity fuel jet, as well as according to the $k-\omega$ model (dotted line) and the $k-\epsilon$ model (dash-dotted line) with a fully developed fuel jet. All these with the EBU-reaction model. ∘ Experiments from Ref. [29].

high speeds of sound due to the high temperatures. Nevertheless, after completing all the necessary modifications to the solver, there were no special problems with the simulations. One noteworthy thing was that the flux limiter had to be employed in all the simulations with the reaction model. Therefore, the discretization scheme was second-order upwind with the van Albada limiter. The reason is obviously the strong gradients caused by the reaction zones in the flow field.

Figure 4.3 shows the conservative scalar distributions along the symmetry axis according to all the reactive simulations carried out in this work together with the experimental results. As can be seen, the inlet conditions have a strong effect on the initial mixing properties of the jet, whereas the final distribution closer to the outflow edge seems to depend more on the employed turbulence model. According to the $k-\omega$ model, the conservative scalar ξ diffuses faster than according to the $k-\epsilon$ model.

Figure 4.4 shows the temperature distributions along the symmetry axis according to the different solutions. Again, the inlet conditions of the fuel jet affect the initial mixing properties, and the overall behaviour is governed by the employed turbulence model. The peak temperature on the axis is somewhat lower according to the $k-\omega$ model than according to the $k-\epsilon$ model. According to Ref. [29], the stoichiometric equilibrium temperature for this mixture is $2\,170$ K, whereas in Ref. [30] a value of $2\,183$ K is given. Both of these are higher than those seen in

Figure 4.4.

The radial temperature distribution at $x/d = 10$ according to the simulations and experiments is shown in Figure 4.5. These results also conform to the previous statement about the different diffusion rates due to different turbulence models. According to this figure, all the simulations overpredict the maximum temperature by over $200°$. This is probably due to overpredicted reaction rates.

The radial distributions of the conservative scalar ξ at cross-sections $x/d = 10$ and $x/d = 20$ according to all the simulations are shown in Figures 4.6 and 4.7. As can be seen, there are differences between the computed and measured distributions, especially near the axis, but in general the agreement is quite good.

Based on Figures 4.3 – 4.7, the solution according to the $k - \epsilon$ model with the fully developed fuel jet gives the best prediction for the conservative scalar ξ in the flow field. According to Figures 4.6 and 4.7, all but the solution according to the $k - \epsilon$ model with the bulk fuel jet predict the ξ-distribution very well except right at the axis of symmetry. These results demonstrate the importance of the inlet conditions for the solution details near the axis of symmetry. With the bulk inlet, the conservative scalar ξ remains unchanged considerably further downstream along the x-axis, and the steepness of the gradient in the radial direction is clearly overpredicted by the constant velocity fuel-jet simulation employing the $k - \epsilon$ model. Nevertheless, all of the presented results are promising, and the basic implementation can be regarded as validated.

We should keep in mind that the EBU-reaction model is employed with the model coefficients presented for the $k - \epsilon$ turbulence model. The transformation to the ω-based formulation of Eq. (2.95) is merely a change of variables — no efforts to account for the different properties of the $k - \omega$ model with respect to the $k - \epsilon$ model are made. Only one test case is not enough to justify general adjustments of the model parameters. For that purpose, a wider selection of test cases should be studied. The presented results demonstrate that there is no urgent need to tune the parameters.

Although not shown here, the results with a low-Reynolds number $k - \epsilon$ model presented by Gran *et al.* [30] are very similar to those obtained here with the fully developed inlet using the $k - \epsilon$ model. The axial distribution of ξ obtained by Gran *et al.* is as accurate as the present result from $x/d = 30$ downstream, but before that they predicted somewhat higher values for ξ. They employed three combustion models in their work, namely the assumed-PDF method [60], the Eddy-Dissipation Concept (EDC) by Magnussen, with a fast chemistry assumption, and the EDC with detailed chemistry. Gran *et al.* also utilized four turbulence models: the standard $k - \epsilon$ model, RSM, the low-Reynolds number $k - \epsilon$ model by Launder and Sharma, and the low-Reynolds number RSM by Kebede *et al.* Their conclusion was that the important issue was proper turbulence modelling. The results obtained by Correa and Gulati [29] differ somewhat more from the present results probably because they used the standard $k - \epsilon$ model. Correa and Pope [61], on the other hand, obtained very good results with a hybrid Monte Carlo PDF/finite-volume mean flow model.

Figures 4.8 through 4.11 show the scaled excess velocity u^* as a function of the

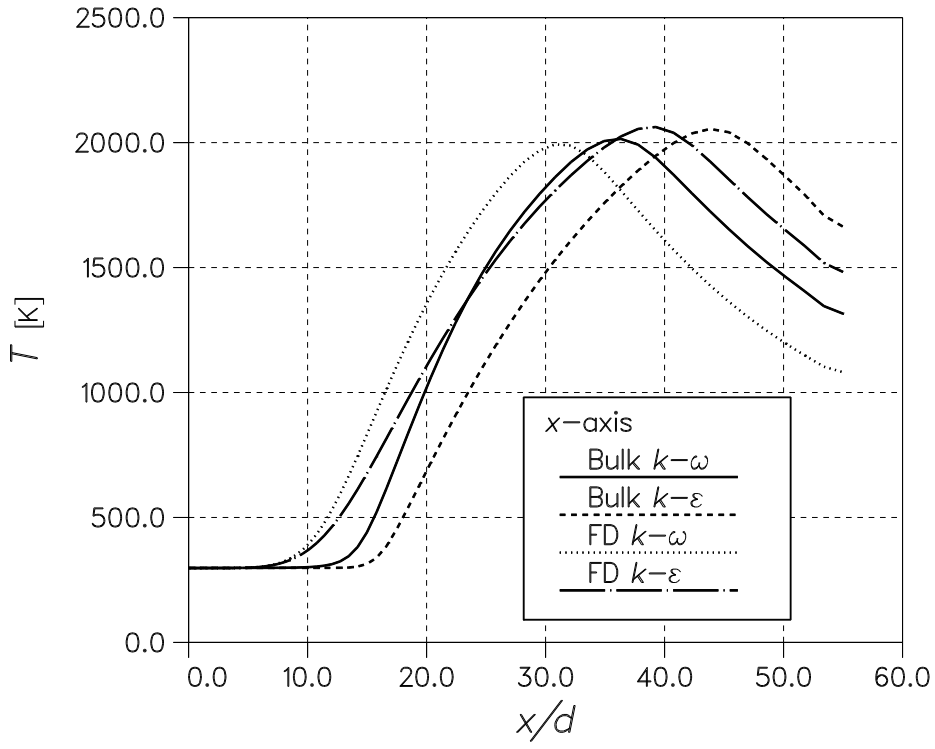

Fig. 4.4: The temperature along the symmetry axis according to the different turbulence models with the EBU-reaction model.

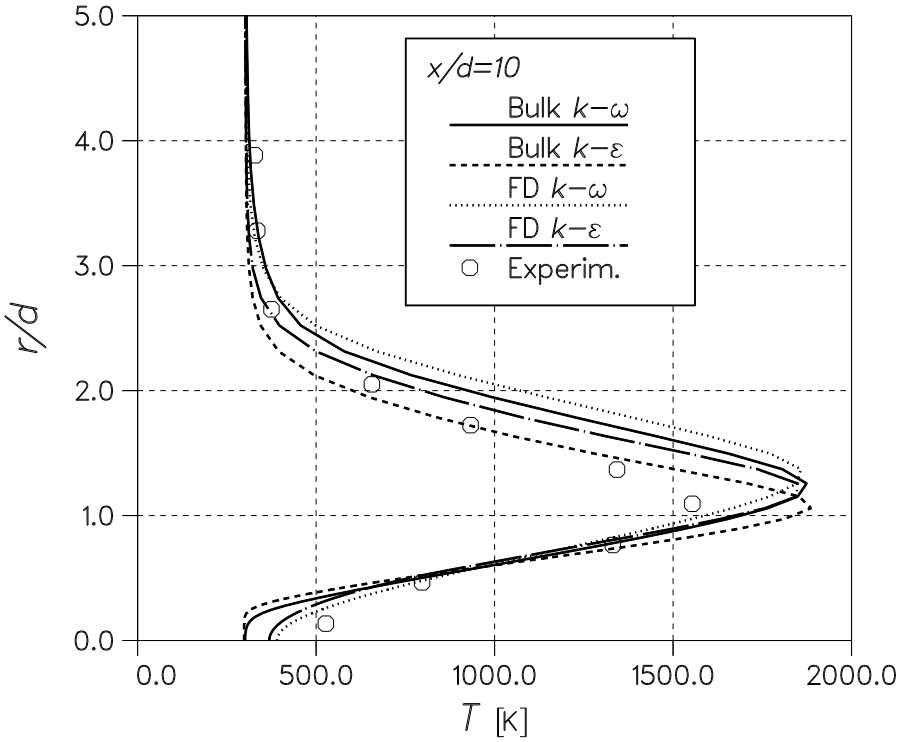

Fig. 4.5: The temperature distribution at section $x/d = 10$ according to the different turbulence models with the EBU-reaction model. ∘ Experiments from Ref. [29].

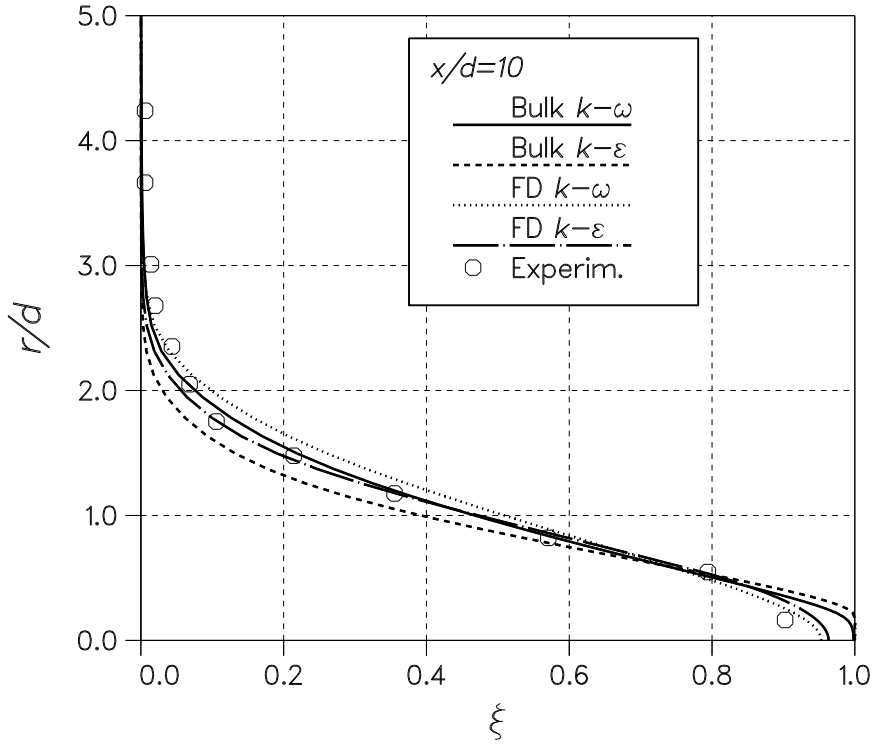

Fig. 4.6: The conservative scalar ξ at section $x/d = 10$ according to the different turbulence models with the EBU-reaction model. ∘ Experiments from Ref. [29].

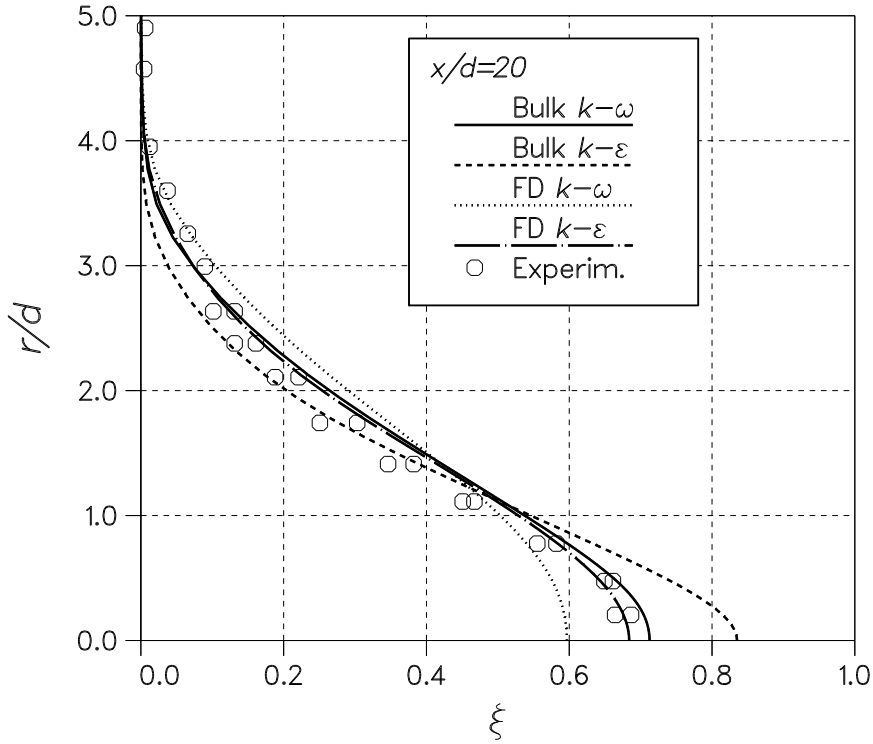

Fig. 4.7: The conservative scalar ξ at section $x/d = 20$ according to the different turbulence models with the EBU-reaction model. ∘ Experiments from Ref. [30].

distance from the x-axis scaled with the velocity-based jet half-width. Results are given for all the computed cases at cross-sections $x/d = 5$, $x/d = 10$, $x/d = 20$, and $x/d = 40$. Figures 4.8 and 4.9 show clearly that the fully developed fuel-jet simulations tend to approach a self-similar solution almost as early as at $x/d = 10$, whereas Figure 4.10 shows that, with the $k - \epsilon$ model and constant velocity fuel jet, self-similarity is reached at $x/d = 20$. According to Figure 4.11, the $k - \omega$ simulation does not reach a self-similar state near the x-axis, but as of $x/d = 10$ and moving downstream from that section, the u^*-profiles seem to converge towards a self-similar solution, especially further away from the axis, when $r_u^* \geq 1.0$.

Figure 4.12 shows the jet half-width based on the conservative scalar as a function of x/d according to all the reactive flow simulations. First and foremost, this figure gives an idea of how quickly the conservative scalar is mixed. The spreading rate is largest according to the $k - \omega$ simulation with the fully developed jet, but in general the trends are pretty much alike with all the simulations.

Figure 4.13 shows the jet half-width based on the axial excess velocity u^* as a function of x according to all the reactive flow simulations. Up to the section $x/d \approx 11$ the results are relatively similar, but after that there is a similar type of scatter in the results as with the conservative scalar ξ.

An interesting property of the solutions is that, from $x/d = 50$ on to the exit, the jet spreading rate becomes zero, or even slightly negative. This is probably partly due to the outflow boundary conditions, but also due to the effects of the recirculation zone behind the bluff body. It creates a region of flow with lower velocities than at the wind tunnel main stream inlet. The slow-velocity region extends to the exit boundary, and its existence is evident from Figures 4.8 through 4.11. The existence of an axial velocity minimum lower than the main flow velocity makes formula (4.3) somewhat questionable. On the other hand, the existence of the recirculation zone does not support the idea of employing the minimum axial velocity instead of the top-wall velocity in Eq. (4.3). Nevertheless, this slow-velocity region explains why the excess-velocity-based jet width suddenly seems to decrease.

Both the ξ-based and the u^*-based jet half-width results show an approximate jet spreading rate of 0.07–0.08, which is a little bit smaller than the experimental value 0.086–0.096 given for a round non-reacting jet in Ref. [34]. The ξ-based jet width values are a little higher than those based on u^*.

When comparing the spreading rate figures with experimental values, we should remember that the experimental setup and theoretical treatment of round jets do not cover the bluff-body stabilized mixing of jets, not to mention the reactive mixing of a fuel and an oxidant. Therefore, the spreading rate comparison is not supposed to give a perfect agreement.

Figure 4.14 shows the axial velocity profiles along the x-axis according to the different turbulence models and fuel-jet velocity profiles. It is interesting to see how the velocity profiles according to the fully developed jet and the constant velocity jet converge towards almost the same solution. Also, the $k - \omega$ model predicts a clearly faster velocity decay than the $k - \epsilon$ model. The reason for the velocity not being exactly 80 m/s at $x = 0$ for the constant velocity jet is that the pressure at the jet inlet is not precisely what was assumed when defining the inlet boundary

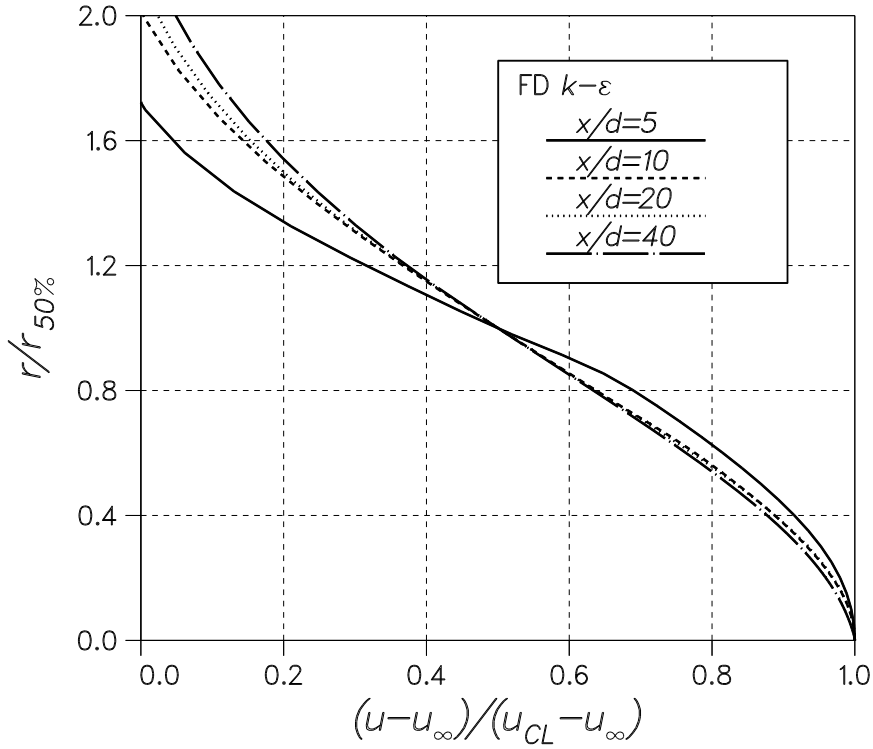

Fig. 4.8: The scaled axial excess velocity u^* as a function of r_u^* at different cross-sections according to the $k-\epsilon$ turbulence model with the reacting fully developed fuel jet.

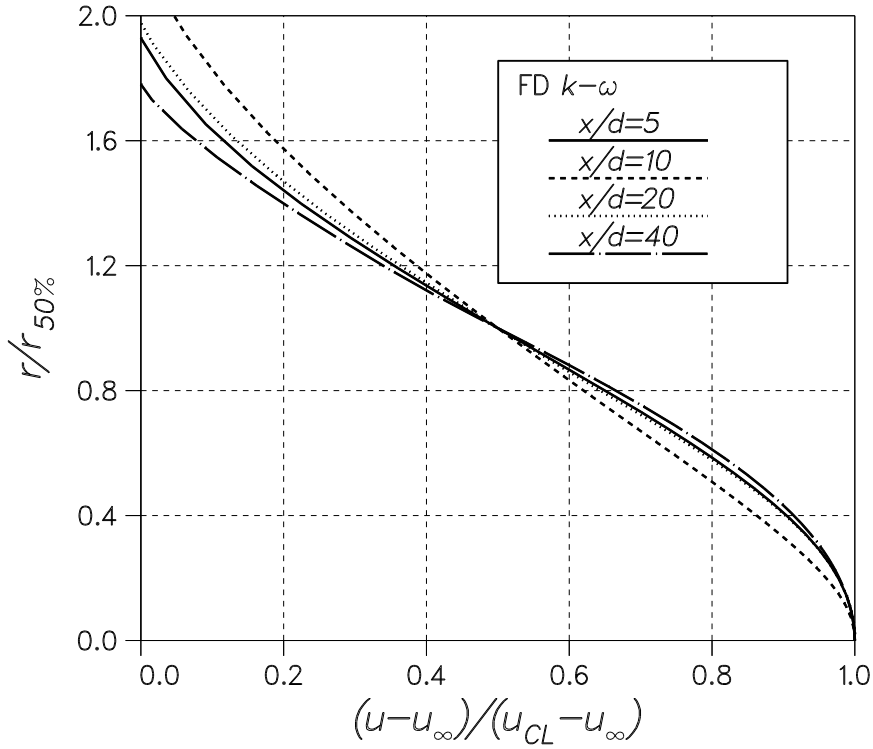

Fig. 4.9: The scaled axial excess velocity u^* as a function of r_u^* at different cross-sections according to the $k-\omega$ RCSST turbulence model with the reacting fully developed fuel jet.

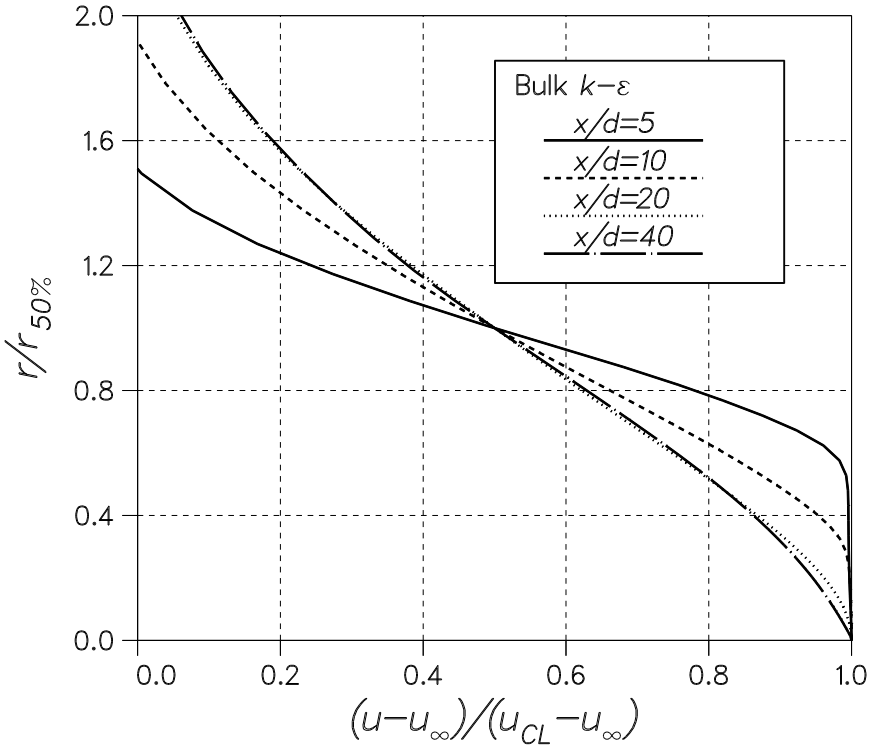

Fig. 4.10: The scaled axial excess velocity u^* as a function of r_u^* at different cross-sections according to the $k-\epsilon$ turbulence model with the reacting constant velocity fuel jet.

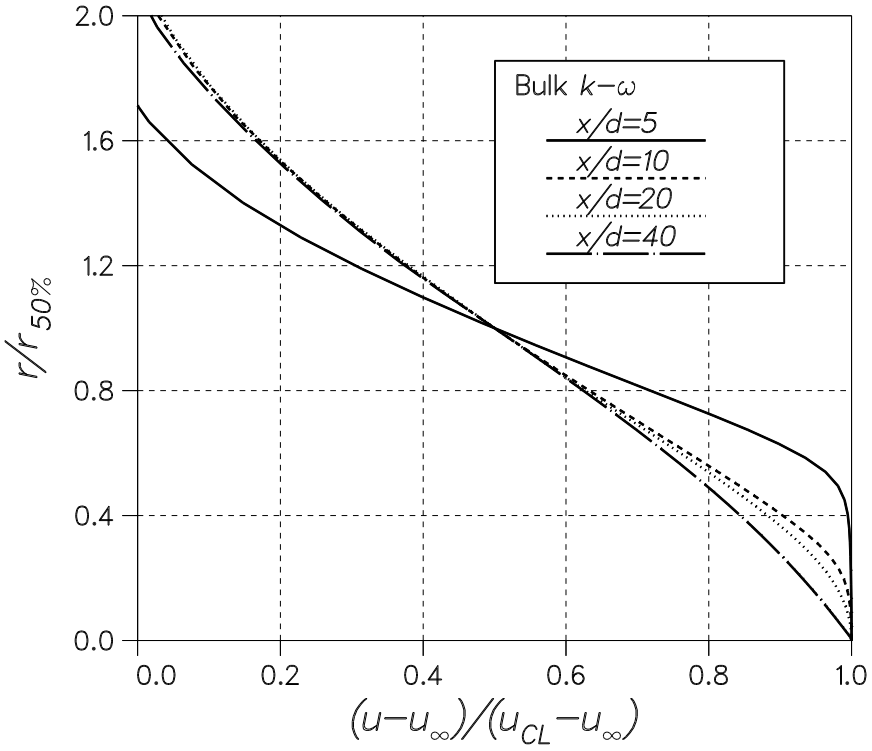

Fig. 4.11: The scaled axial excess velocity u^* as a function of r_u^* at different cross-sections according to the $k-\omega$ RCSST turbulence model with the reacting constant velocity fuel jet.

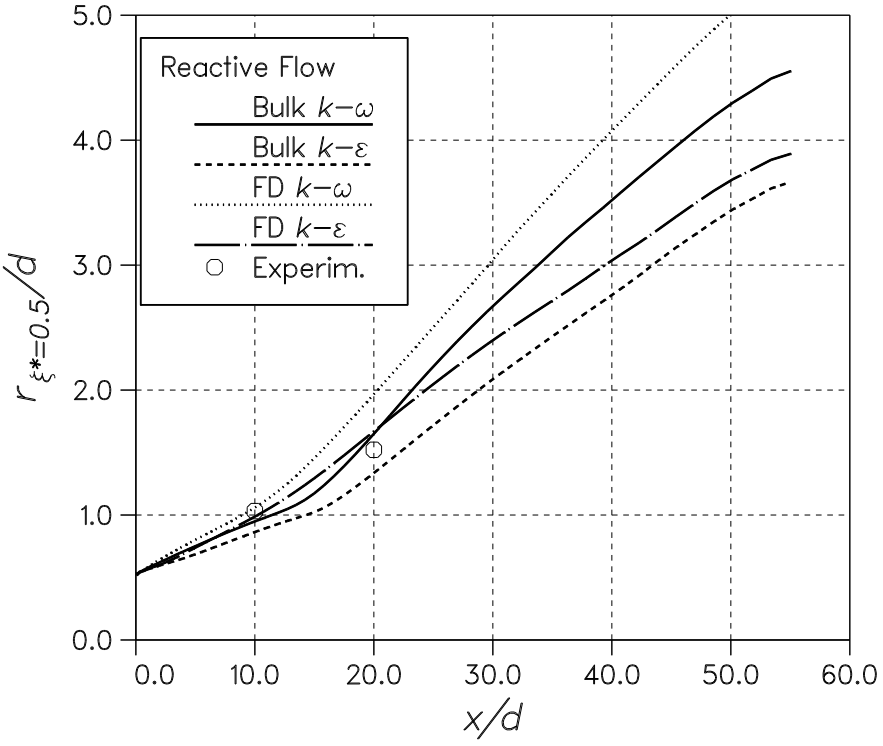

Fig. 4.12: The jet half-width distribution based on the conservative scalar ξ as a function of x/d according to the different turbulence models with the EBU-reaction model.

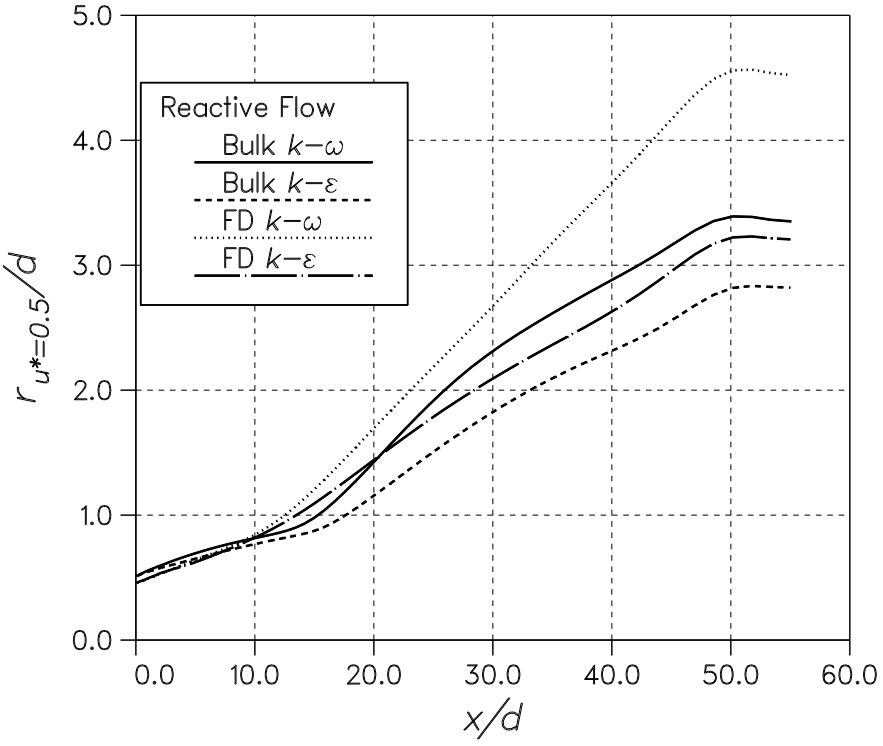

Fig. 4.13: The jet half-width distribution based on the axial velocity u as a function of x/d according to the different turbulence models with the EBU-reaction model.

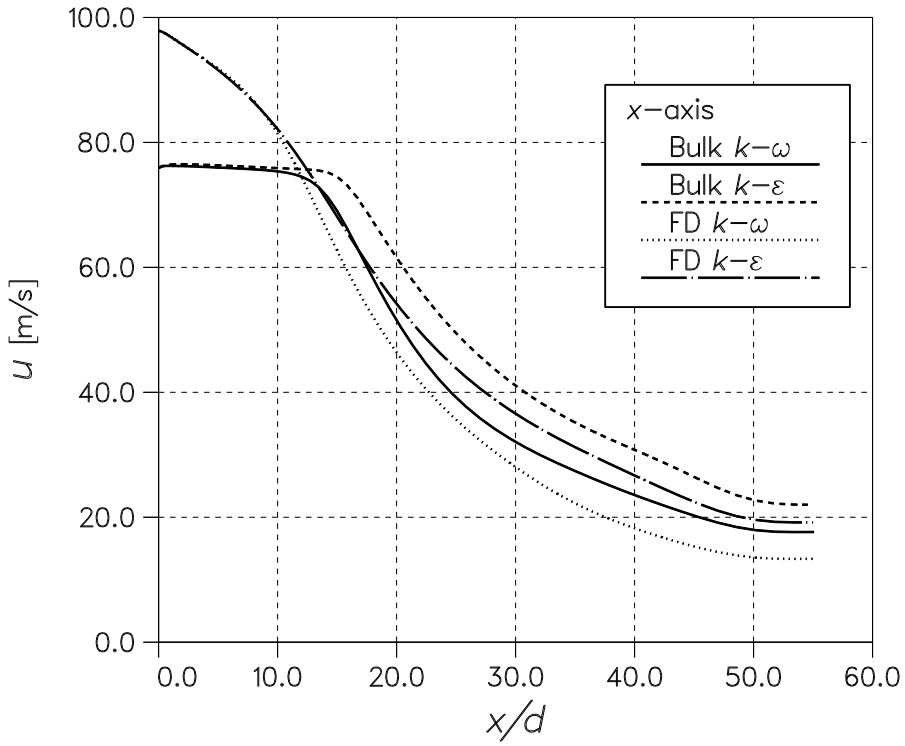

Fig. 4.14: The axial velocity u along the symmetry axis according to the different turbulence models with the EBU-reaction model.

conditions.

Figures 4.15 and 4.16 show the temperature distribution and streamlines for the constant velocity fuel-jet simulations according to the $k-\omega$ and $k-\epsilon$ models, respectively. Figures 4.17 and 4.18 show the same information for the fully developed fuel-jet simulations according to the $k-\omega$ and $k-\epsilon$ models, respectively. These figures show how the $k-\omega$ model predicts a wider, but shorter region of high temperatures than the $k-\epsilon$ model. The streamline patterns are qualitatively very similar to each other, although differences in the details can be seen.

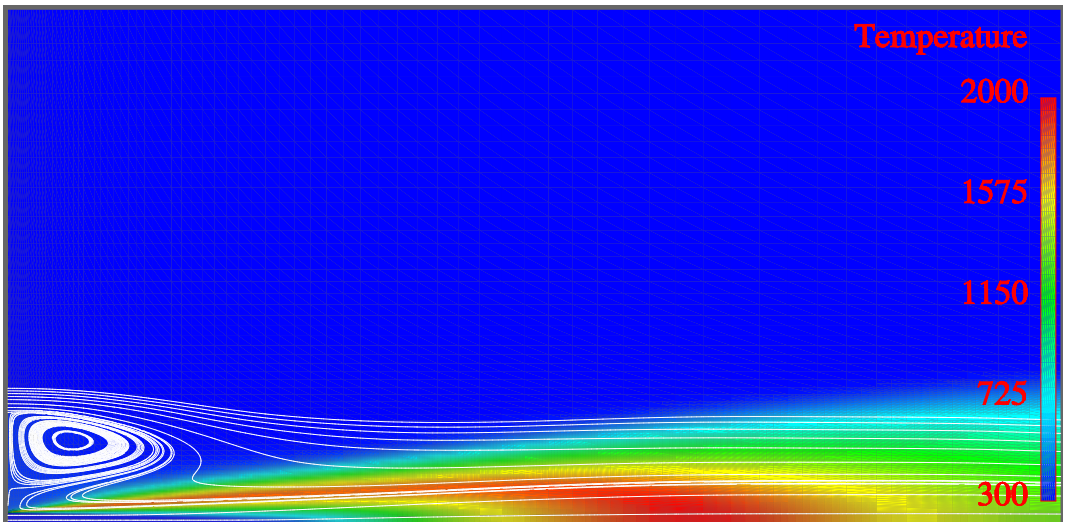

Fig. 4.15: The temperature distribution and streamlines according to the $k-\omega$ model with the reacting constant velocity fuel jet.

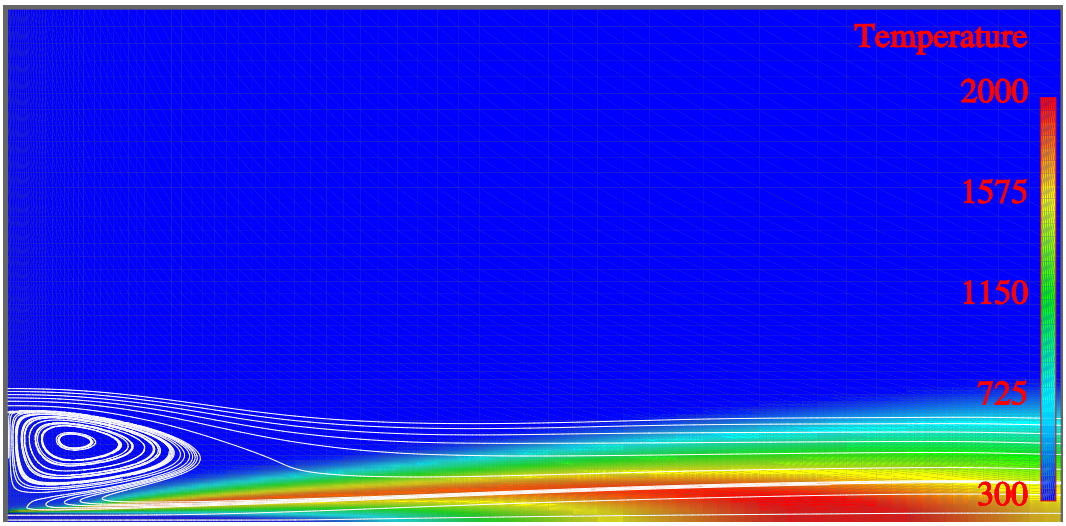

Fig. 4.16: The temperature distribution and streamlines according to the $k-\epsilon$ model with the reacting constant velocity fuel jet.

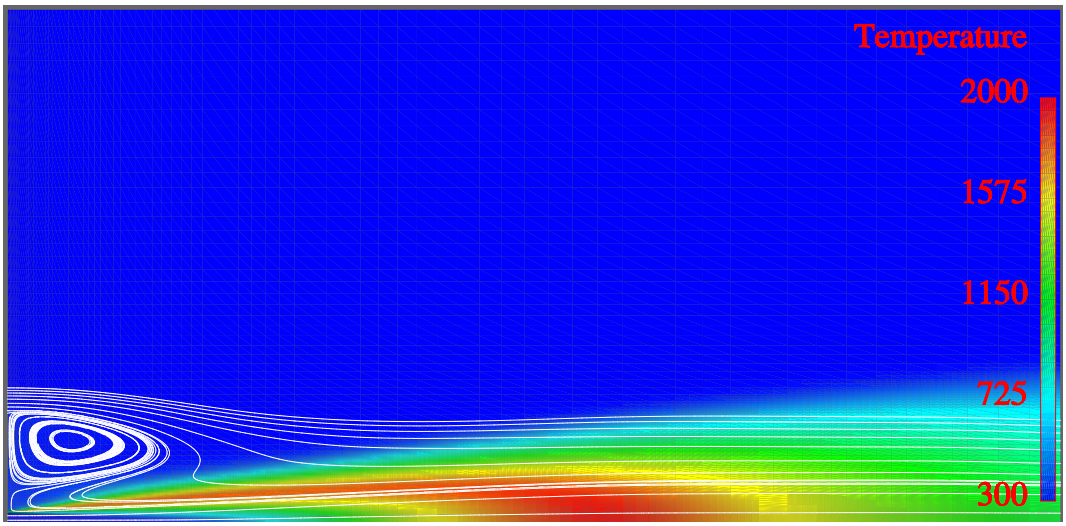

Fig. 4.17: The temperature distribution and streamlines according to the $k-\omega$ model with the reacting fully developed fuel jet.

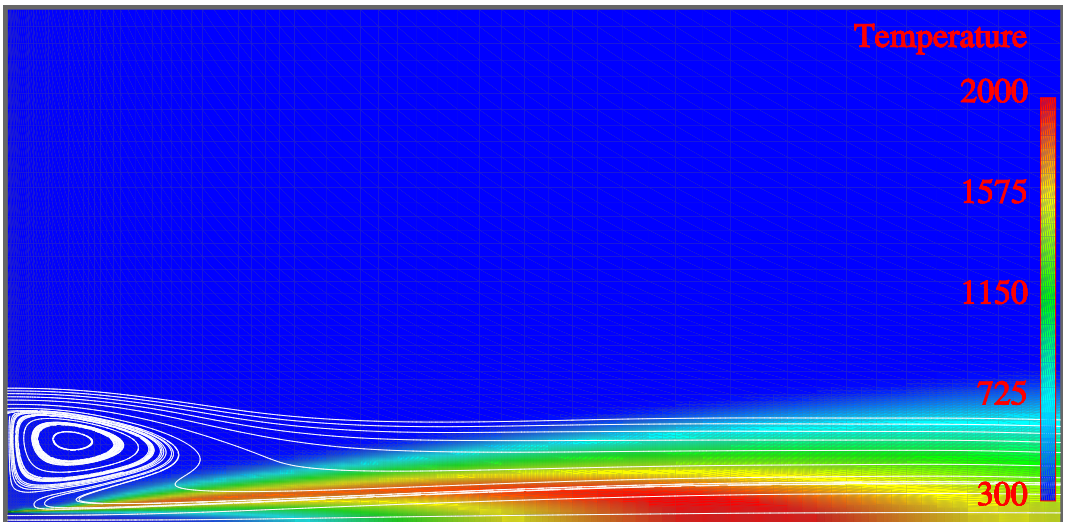

Fig. 4.18: The temperature distribution and streamlines according to the $k-\epsilon$ model with the reacting fully developed fuel jet.

4.3 Simulations with the Non-Reacting Fuel Jet

The same flow cases as described in the previous section were also simulated with the reaction model deactivated, i.e. simulating non-reactive flow. The main idea was to gain more insight into which differences were caused by the differences between the turbulence models, and which ones were caused by the reaction model.

Figures 4.19 and 4.20 show the scaled excess velocity u^* as a function of the distance from the x-axis scaled with the velocity-based jet half-width according to the simulations with the fully developed fuel jet employing the $k-\epsilon$ model and the $k-\omega$ RCSST model, respectively. Figures 4.21 and 4.22 show the same information for the cases with the constant velocity jet. According to these figures, the simulations with the fully developed fuel jet start to reach self-similarity at $x/d = 20$, whereas according to the constant velocity jet, self-similarity is not reached at all.

Figure 4.23 shows the ξ-based and Figure 4.24 shows the u^*-based jet half-width as a function of x/d. As a whole, the different simulations predict quite similar spreading rates to each other. However, it is interesting to see, how the ξ-based data and u^*-based data cross each other. Based on ξ, the $k-\omega$ model predicts systematically faster spreading of the jet than the $k-\epsilon$ model, while based on u^*, towards the end of the computational domain, the constant velocity jet simulations with both of the employed turbulence models predict faster spreading than the fully developed jet simulations. The constant velocity jet simulations predict an almost linear growth of the u^*-based jet half-width between $x/d = 8$ and $x/d = 45$.

After $x/d \approx 50$, the u^*-based jet half-width starts to decrease, which is a consequence of the low-velocity region due to the recirculation zone. This confirms that the similar behaviour seen in the results for the reactive flow field was not an anomaly caused by the reaction model.

The conservative scalar behaves qualitatively in a similar fashion as in the reactive flow simulations. The details are, however, completely different, as seen from the radial ξ-profiles at $x/d = 10$ and at $x/d = 20$ shown in Figures 4.25 and 4.26. The rapid mixing of the conservative scalar is also seen as a fast decay of ξ in the axial ξ-profile shown in Figure 4.27.

Figure 4.28 shows the axial velocity profiles as predicted by the non-reacting simulations. Again, we can see that, the $k-\omega$ model predicts a more rapid velocity decay than the $k-\epsilon$ model.

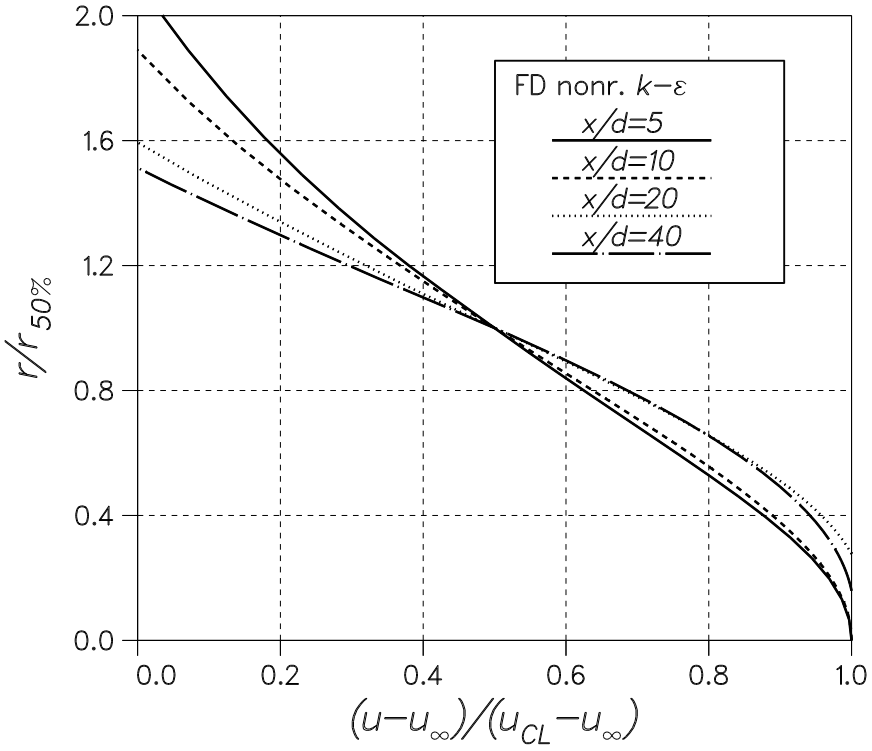

Fig. 4.19: The scaled axial excess velocity u^* as a function of r_u^* at different cross-sections according to the $k-\epsilon$ turbulence model with the non-reacting fully developed jet.

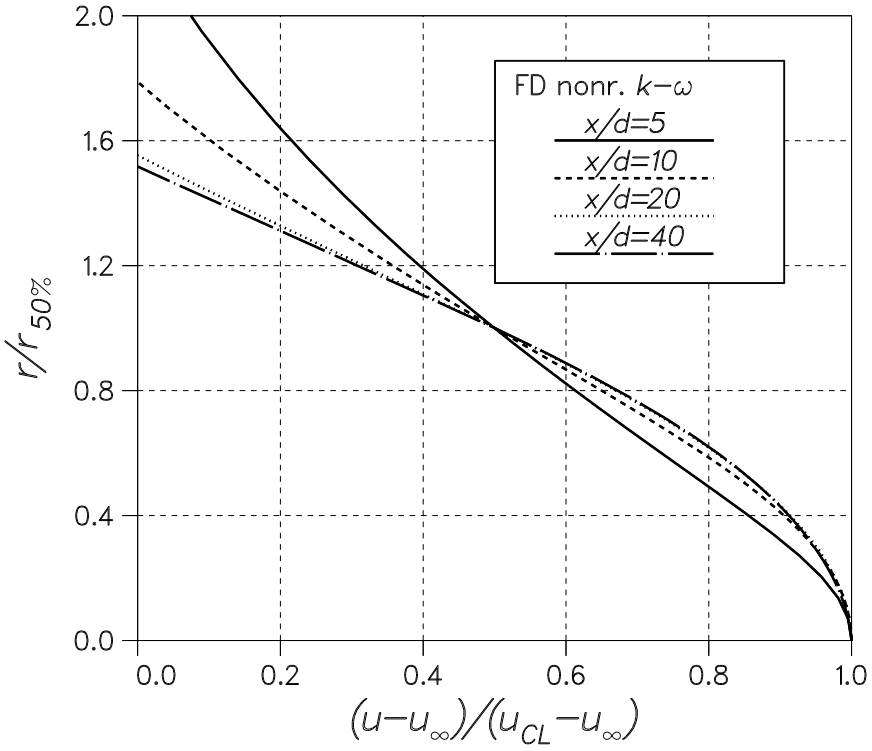

Fig. 4.20: The scaled axial excess velocity u^* as a function of r_u^* at different cross-sections according to the $k-\omega$ RCSST turbulence model with the non-reacting fully developed jet.

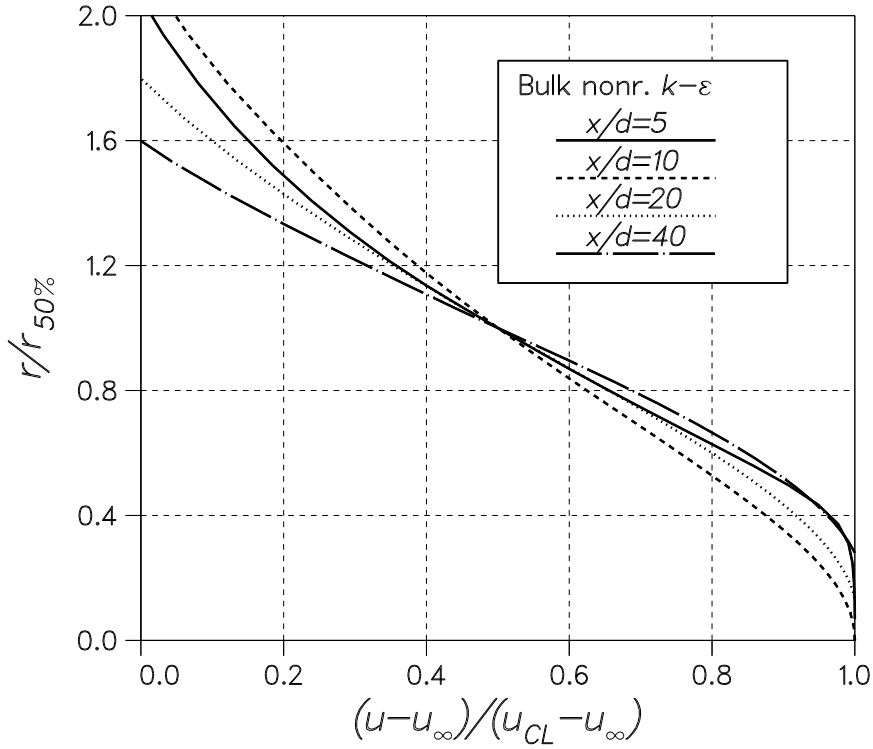

Fig. 4.21: The scaled axial excess velocity u^* as a function of r_u^* at different cross-sections according to the $k-\epsilon$ turbulence model with the non-reacting constant velocity jet.

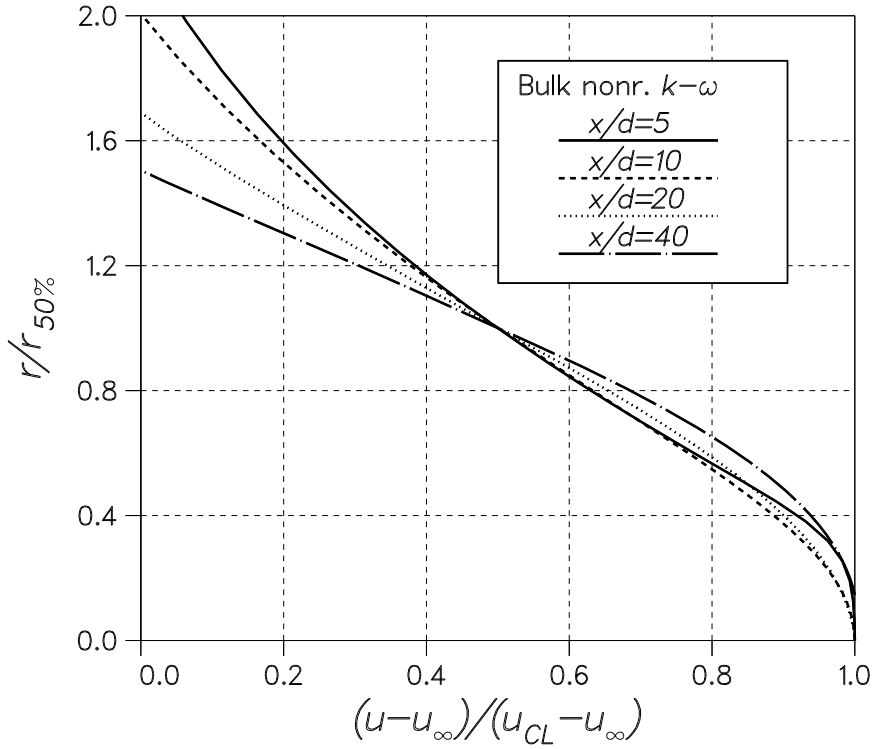

Fig. 4.22: The scaled axial excess velocity u^* as a function of r_u^* at different cross-sections according to the $k-\omega$ RCSST turbulence model with the non-reacting constant velocity jet.

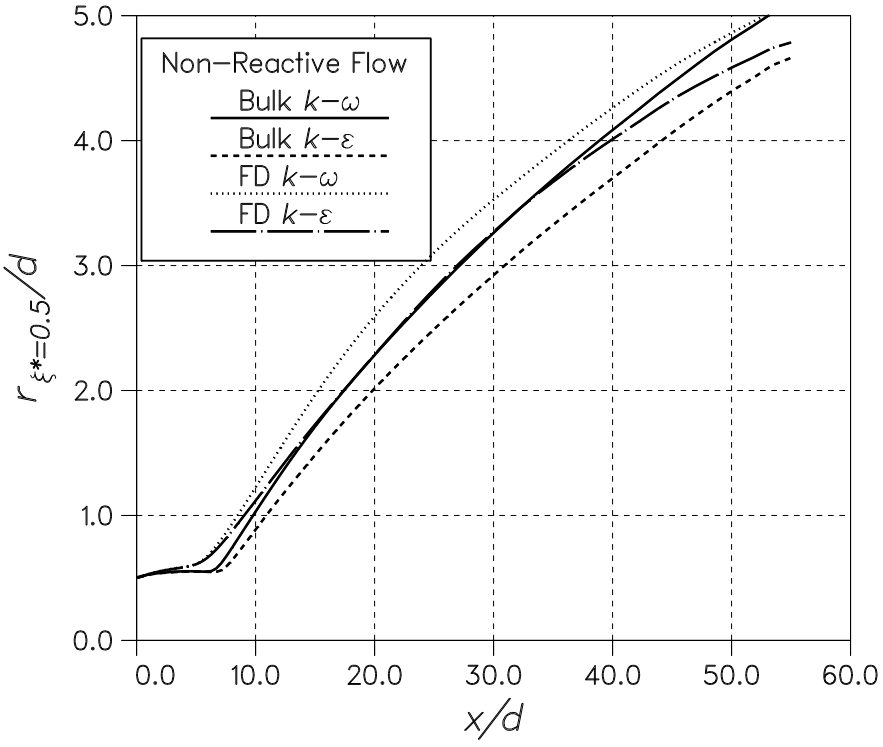

Fig. 4.23: The jet half-width distribution based on the conservative scalar ξ as a function of x/d according to the different turbulence models with the non-reacting jet.

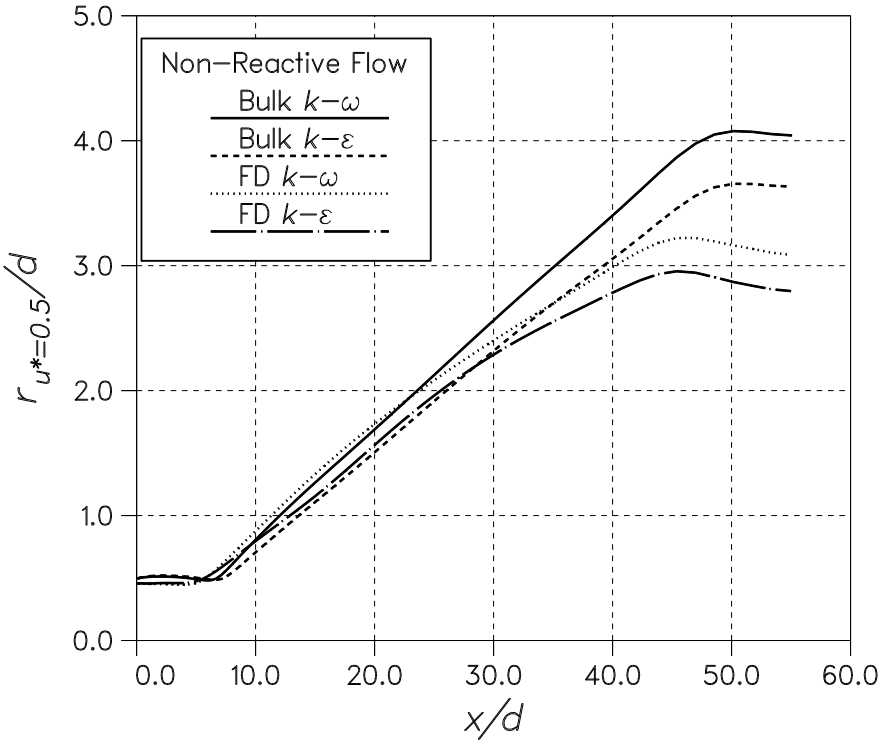

Fig. 4.24: The jet half-width distribution based on the axial velocity u as a function of x/d according to the different turbulence models with the non-reacting jet.

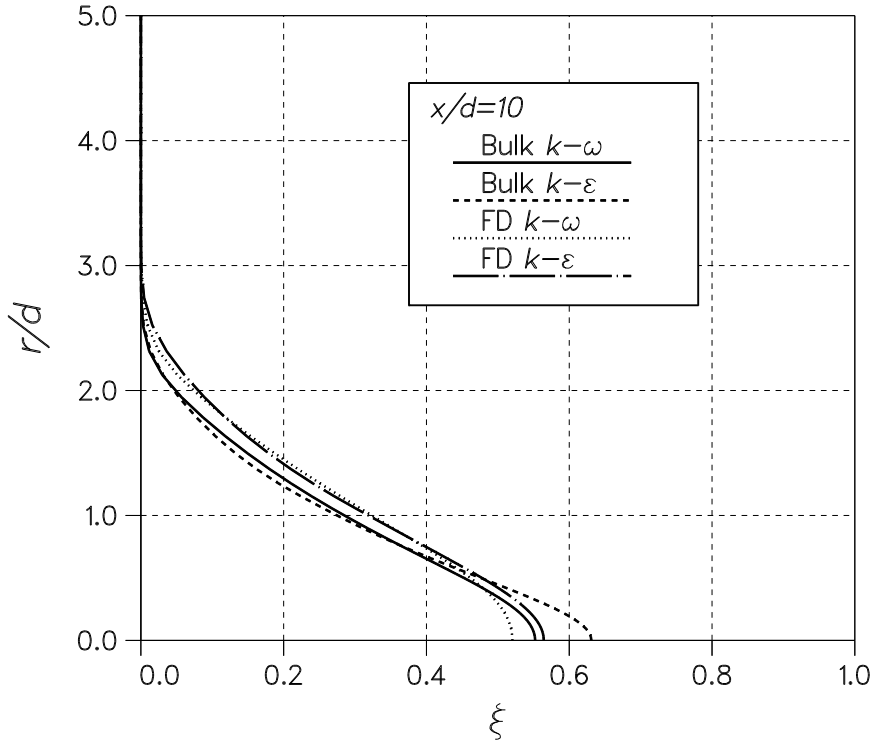

Fig. 4.25: The conservative scalar ξ at section $x/d = 10$ according to the different turbulence models with the non-reacting jet.

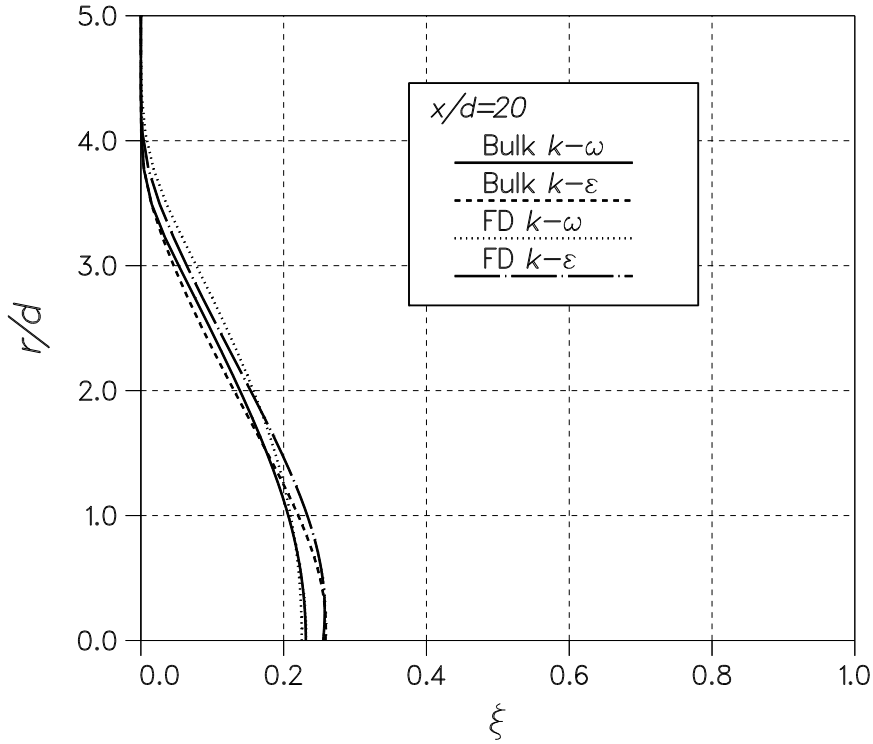

Fig. 4.26: The conservative scalar ξ at section $x/d = 20$ according to the different turbulence models with the non-reacting jet.

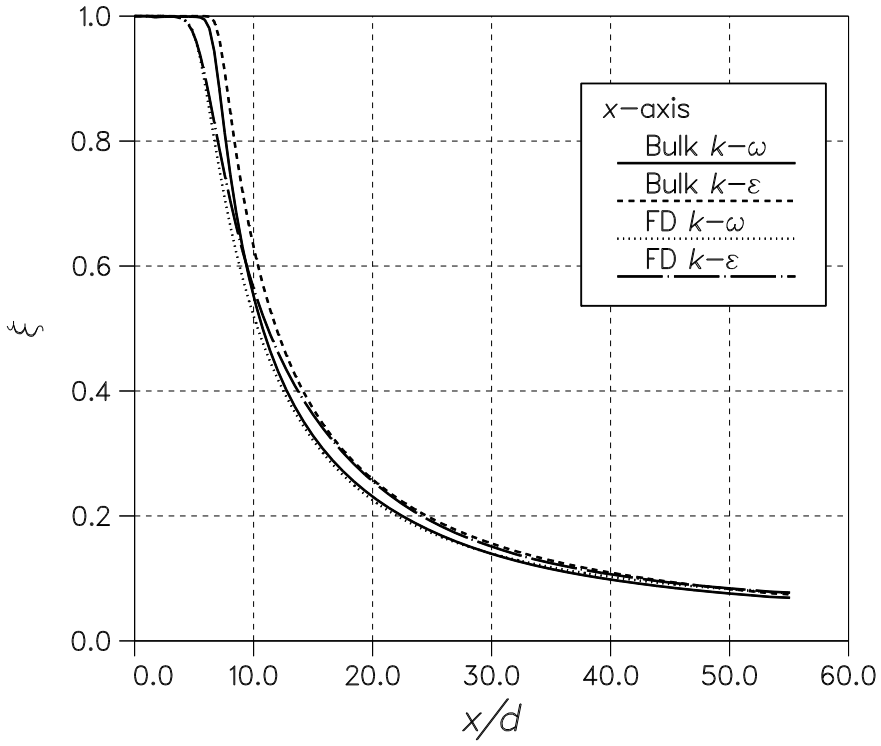

Fig. 4.27: The conservative scalar ξ along the symmetry axis according to the different turbulence models with the non-reacting jet.

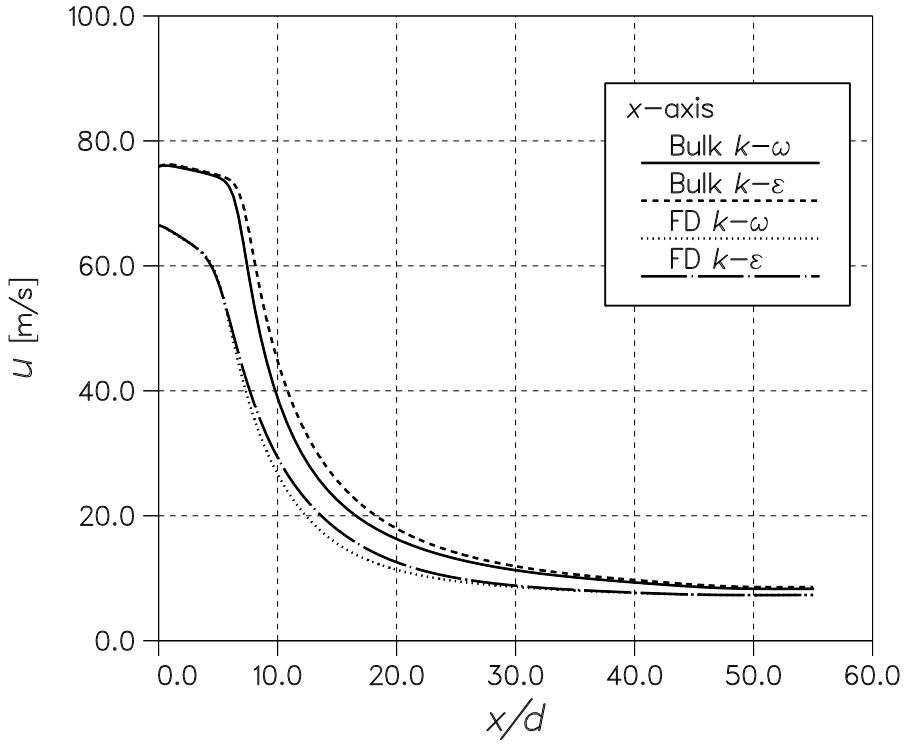

Fig. 4.28: The axial velocity u along the symmetry axis according to the different turbulence models with the non-reacting jet.

4.4 Grid Independence Study

In order to verify that the grid density employed in the previous simulations was sufficient, a grid independence study was carried out. A grid with twice as many cells in the axial and radial directions, respectively, was employed for the simulation of the reactive flow case with a fully developed inlet using the $k-\omega$ RCSST model.

Figure 4.29 shows a comparison of the ξ-distributions along the x-axis according to the simulation with the standard grid and according to the simulation with the dense grid. As can be seen, there are small differences between the results in the area $18 < x/d < 38$. The differences are, however, much smaller than those seen between the different turbulence models. Therefore, the standard resolution employed in the simulations can be regarded as sufficient.

Figures 4.30 and 4.31 show the conservative scalar ξ at sections $x/d = 10$ and $x/d = 20$, respectively, and Figure 4.32 shows the temperature comparison at $x/d = 10$. These figures confirm that the standard resolution is sufficient for the conducted simulations.

4.5 General Remarks

Based on the simulations described in the previous sections, the implementation of the EBU-reaction model can be regarded as validated. There are differences between the computational and experimental results, of course, but qualitatively the numerical results are consistent with the experimental ones, and in general the agreement with the experiments is good.

The implementation with the $k-\omega$ model could be reviewed, and the EBU-model coefficients might be fine-tuned. However, there is nothing fundamentally wrong in the present results, and modification of the model coefficients based on one single test case only is not what should be done.

The comparison between the reactive and the non-reactive flow simulations shows that the jet spreading behaviour is completely changed when the reactions are accounted for. The main reason for this is the slower decay of the jet velocity, which, in effect, stretches the region with high values of ξ further downstream.

The effects of the employed thermodynamic model were also investigated by simulating the constant velocity jet cases with a thermodynamic model for a mixture of calorically perfect gases. The properties of the components were frozen to the conditions at $T = 25°\text{C}$. Although not shown here, the maximum temperatures according to those simulations were over $200°$ higher than those obtained with the model for a mixture of thermally perfect gases, thus exceeding the value of stoichiometric equilibrium temperature. Therefore, it is justified to say that the selected thermodynamic model may have an all but non-negligible effect on the results. This applies, naturally, to the thermodynamic model parameters as well.

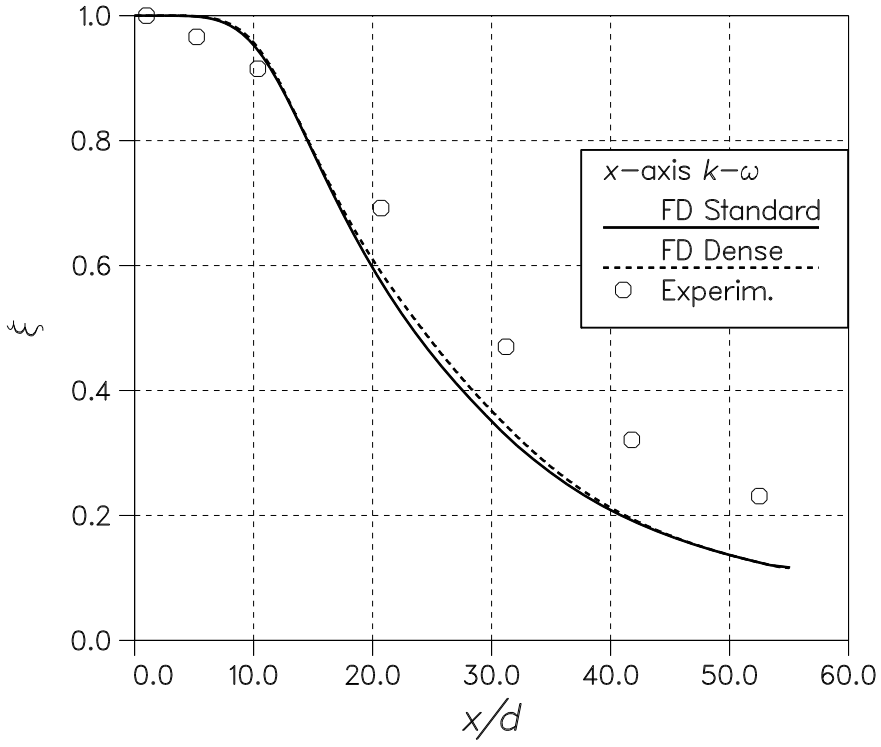

Fig. 4.29: The conservative scalar ξ along the symmetry axis according to the $k-\omega$ RCSST model with the EBU-reaction model employing the standard grid and the dense grid. ∘ Ref. [29].

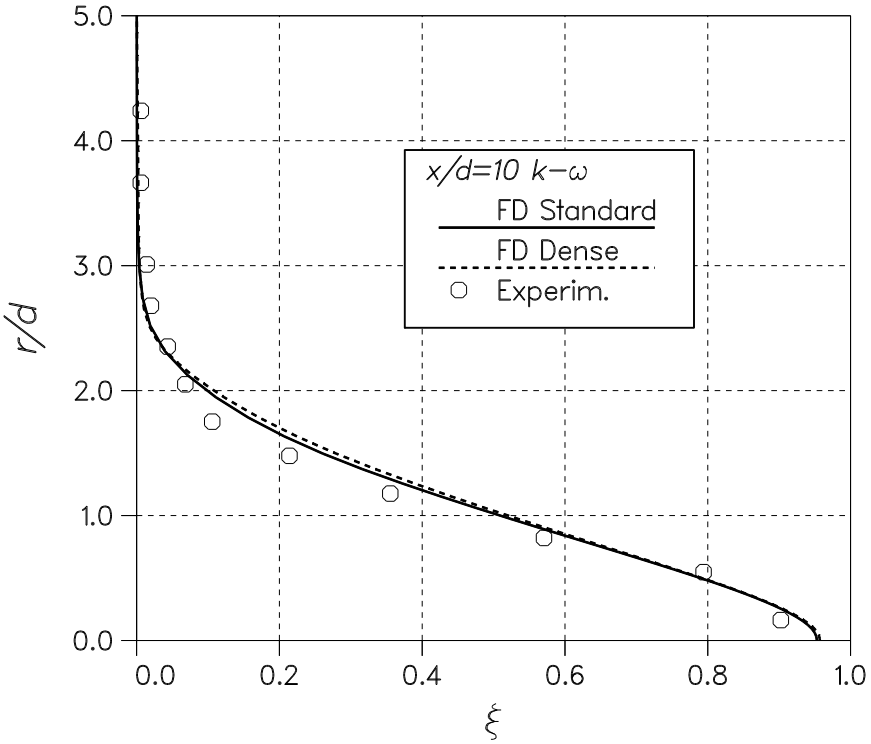

Fig. 4.30: The conservative scalar ξ at section $x/d = 10$ according to the $k-\omega$ RCSST model with the EBU-reaction model employing the standard grid and the dense grid. ∘ Ref. [29].

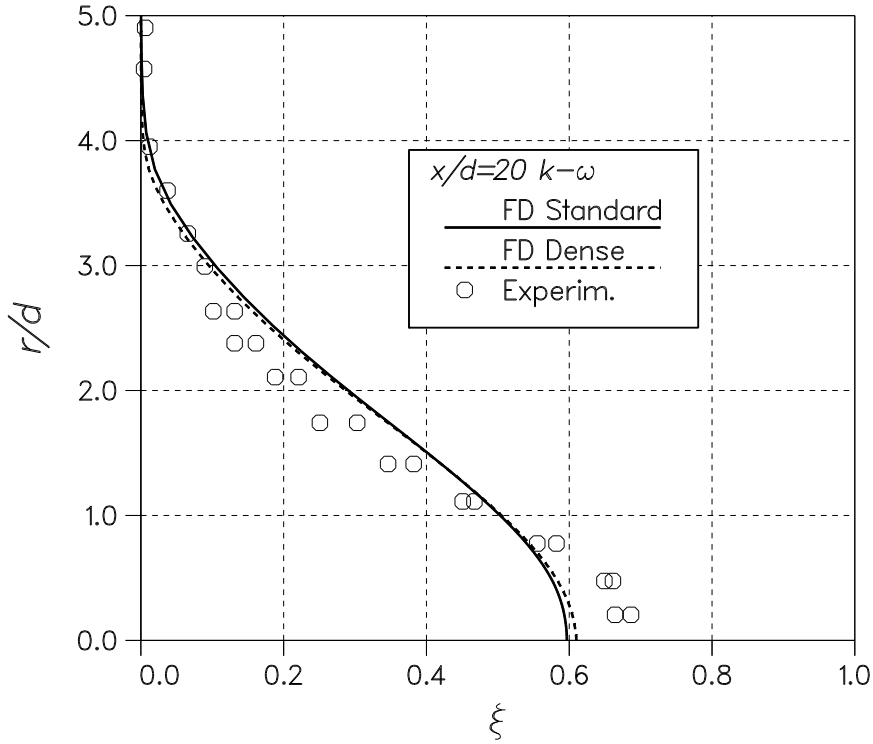

Fig. 4.31: The conservative scalar ξ at section $x/d = 20$ according to the $k - \omega$ RCSST model with the EBU-reaction model employing the standard grid and the dense grid. ∘ Ref. [30].

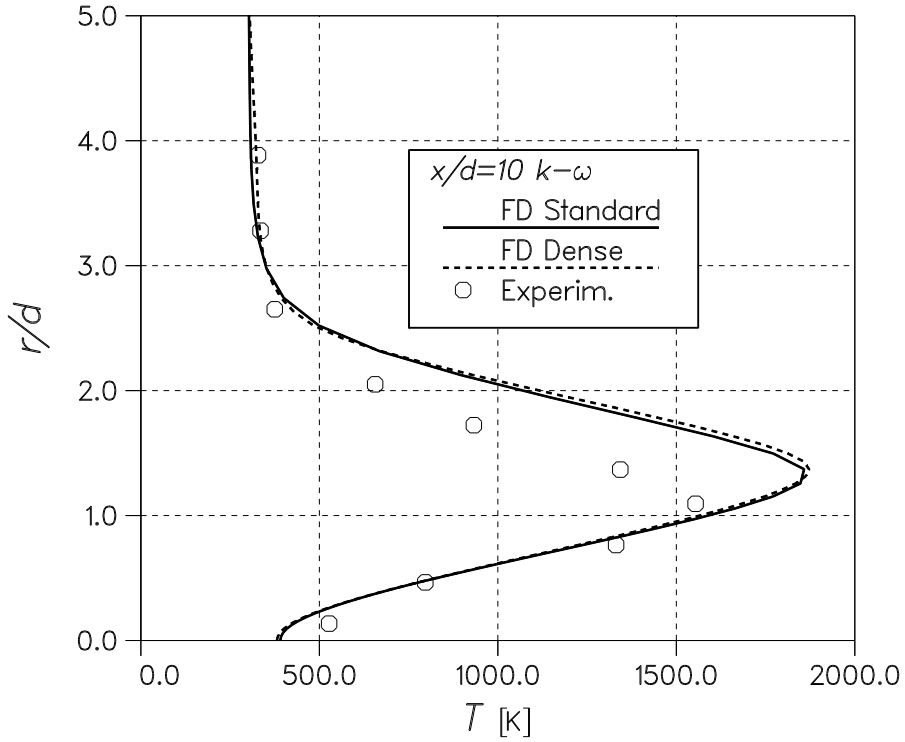

Fig. 4.32: The temperature distribution at section $x/d = 10$ according to the $k - \omega$ RCSST model with the EBU-reaction model employing the standard grid and the dense grid. ∘ Ref. [29].

5 Long-Range Artillery Projectile with a Base-Bleed Unit

The practical application of the reaction model described and validated in the previous chapters is to simulate the flow past a supersonic 155 mm-diameter long-range artillery projectile with base bleed. The same projectile has been simulated previously with base bleed, but the projectile was non-rotating [18]. Another major difference is that now the flow field inside the base-bleed unit is also included in the computational domain, not to mention the simulations including chemical reactions.

The grid for the projectile under investigation is shown in Figure 5.1, and a detailed view of the base-bleed unit is shown in Figure 5.2. The computational domain is discretized with a two-block $128 \times 64 \times 1 + 64 \times 128 \times 1$ grid. One of the blocks describes the surface of the projectile, and the other one describes the inside of the base-bleed unit as well as the wake behind the unit. Based on previous studies [18, 20–22] the employed grid density is expected to be sufficient for these simulations. The origin of the coordinate system with the x-axis aligned with the axis of rotation is placed at the design origin, which is located 50 mm aft of the nose of the fuze. The length of the body is 912 mm and therefore the x-coordinate of the base is 0.862 m. The approximations made in the modelling of the geometry of the nozzle are shown in Figure 5.3.

The simulations are for the projectile flying at $Ma_\infty = 1.2$, $Re_D = 1.4 \cdot 10^6$ and $\alpha = 0°$, which describes approximately the flow conditions just before the burning of the base-bleed unit comes to an end. At this point in the trajectory some problems were encountered with the base-bleed unit in the test firings [62], and therefore this work is focused on that specific point. Since the simulations are for a zero angle of attack case and the geometry is axisymmetric, only a 2-degree slice of the projectile is modelled with one cell in the circumferential direction. This way, the flow is forced to remain 2-D axisymmetric, which is not necessarily the case behind the base of the projectile. The so introduced errors are hoped to be small.

This flow case is simulated in six different ways: without base bleed, with non-reacting base bleed, and with reacting base bleed. These three cases are simulated assuming the projectile is either non-rotating or rotating at $18\,000$ rpm, which is an estimate for the angular velocity of the projectile under the described conditions. In all the simulations, the $k - \omega$ RCSST model is employed for turbulence modelling.

The reaction model and the thermodynamic model parameters employed in the simulations are those described in Section 3.2. In the simulations with base bleed, the mass flow rate is estimated based on the ambient pressure $p = 30.8$ kPa at an

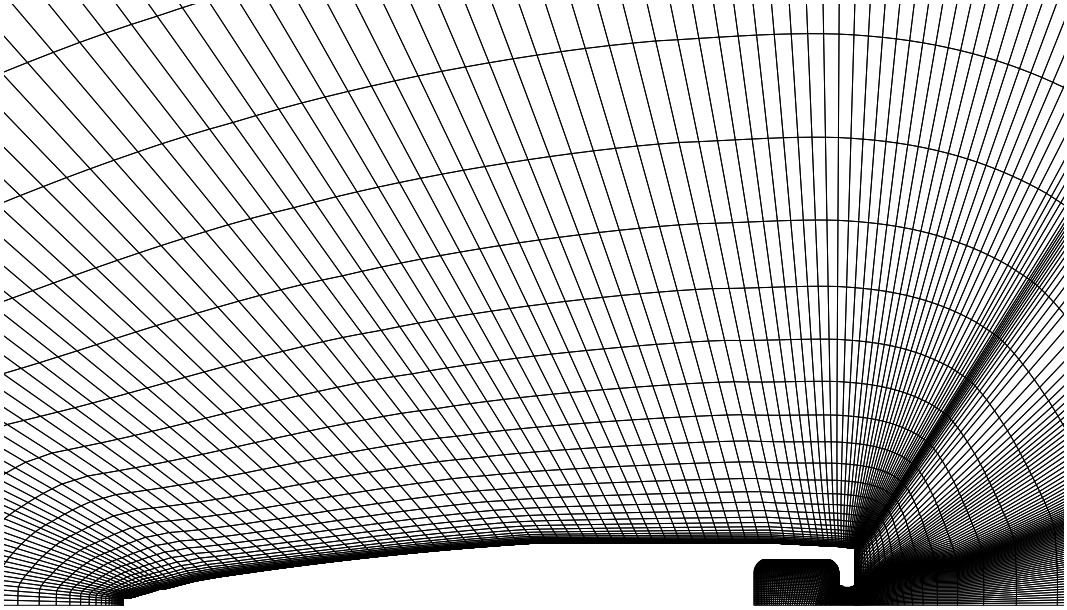

Fig. 5.1: The $2 \times 128 \times 128 \times 1$ grid used to model the geometry of the long-range projectile.

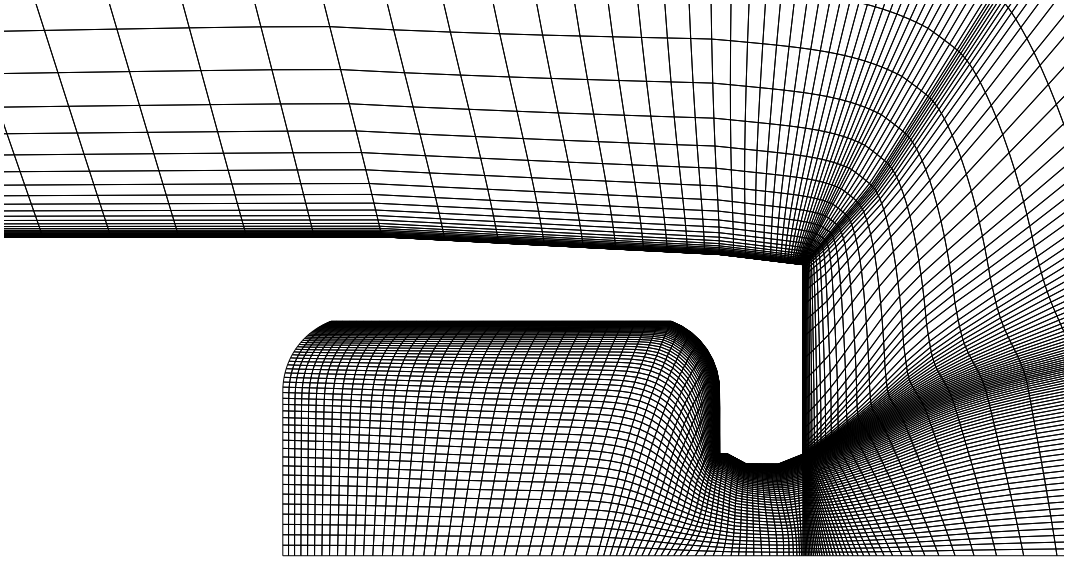

Fig. 5.2: Detail view of the grid near the base of the long-range projectile.

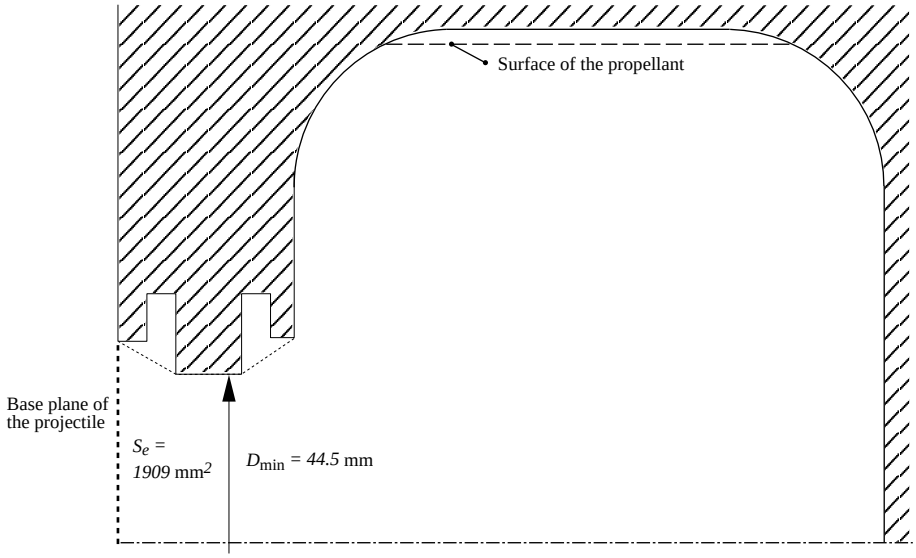

Fig. 5.3: The approximated geometry of the nozzle of the base-bleed unit.

altitude of 9 km, and the propellant properties reported in Ref. [63]. According to Ref. [63] the burning rate of the propellant can be approximated with

$$r = r_0 \left(\frac{p}{p_{\text{ref}}} \right)^n \tag{5.1}$$

where $r_0 = 1.10$ mm/s and $n = 0.6$ are experimentally determined model constants for the propellant. In Eq. (5.1) the reference pressure is $p_{\text{ref}} = 100$ kPa. Multiplying r with the density of the propellant $\rho = 1.525$ g/cm^3 yields the mass flow rate per unit area $\dot{m}_A = 0.8275$ kg/(m^{2}s). In the simulations, the diameter of the surface of the base-bleed propellant is 113.75 mm, which is just slightly less than the outer diameter of the propellant. The area of the burning surface of the propellant under these conditions is $S_{\text{burn}} = 0.02949$ m^2, and consequently the mass flow rate is $\dot{m} = 0.02440$ kg/s. The mass flow rate is commonly expressed with the non-dimensional quantity I defined by

$$I = \frac{\dot{m}}{\rho_\infty V_\infty S_{\text{b}}} \tag{5.2}$$

where $\rho_\infty = 0.362$ kg/m^3 and $V_\infty = 354$ m/s are the free-stream density and velocity, respectively, and $S_{\text{b}} = 0.0156$ m^2 is the area of the shell base. Consequently, in all the simulations with base bleed in this work, the non-dimensional mass flow rate is $I = 0.0122$. To close the inlet definition scheme presented by Eq. (2.117), the turbulence level was set to $4 \cdot 10^{-4}$, and the turbulent viscosity was fixed to $\mu_T/\mu = 0.001$. These values were chosen to represent laminar conditions.

The idea is to determine whether the reaction model improves the accuracy of the drag predictions of the numerical simulations. The cases without base bleed are also simulated with the same grid as the other cases in order to avoid any doubts about grid difference effects. Since there are no wind tunnel measurements available

Table 5.1: The drag coefficient C_D of the projectile. $Ma_\infty = 1.2$, $Re_D = 1.4 \cdot 10^6$ and $\alpha = 0°$. The cases marked with a † required time-accurate time-integration.

	$I = 0$	$I = 0.0122$ Inert flow	$I = 0.0122$ Reactive flow
$\mathbf{\Omega} = 0$ rpm	0.331	$0.280^\dagger$	0.206
$\mathbf{\Omega} = 18\,000$ rpm	0.331	$0.302^\dagger$	$0.217^\dagger$
Test firings [62]	0.324		0.21

for this projectile, the only data for comparison is obtained with a radar from test firings [62]. The drag predictions are presented as non-dimensional drag coefficient values defined by

$$C_D = \frac{D}{\frac{1}{2}\rho_\infty V_\infty^2 S} \tag{5.3}$$

where D is the drag force on the projectile, and $S = \pi D^2/4$ is the reference area based on the nominal diameter of the projectile $D = 155$ mm. The C_D-predictions according to all the simulations, as well as the test firings, are presented in Table 5.1. Based on these results, inclusion of the modelling of the chemical reactions makes a dramatic difference in the C_D-predictions, and, in addition, the predicted drag coefficient is astonishingly close to the experimental value. In the following discussion, the term "base combustion" will be used to denote such combustion that takes place behind the base of a projectile. In all the reactive simulations for the present base-bleed projectile, all the final combustion of the fuel-rich propellant will fall into that category, because the combustion takes place right behind the base, since that is where the fuel and oxidant meet.

5.1 Non-rotating Projectile

According to the simulations with the non-rotating projectile, the base bleed has almost no effect on the pressure and the skin-friction distribution on the surface of the shell. Figure 5.4 shows the C_p-distribution on the surface of the non-rotating shell according to the simulations without base bleed, with inert base bleed, and reactive base bleed. Figure 5.5 shows the c_f-distribution for the same cases. Here, C_p and c_f are defined by

$$C_p = \frac{p - p_\infty}{\frac{1}{2}\rho_\infty V_\infty^2} \tag{5.4}$$

$$c_f = \frac{\tau_\mathrm{w}}{\frac{1}{2}\rho_\infty V_\infty^2} \tag{5.5}$$

In Figures 5.4 and 5.5 the results according to the simulation without base bleed and with non-reacting base bleed are indistinguishable from each other, and they

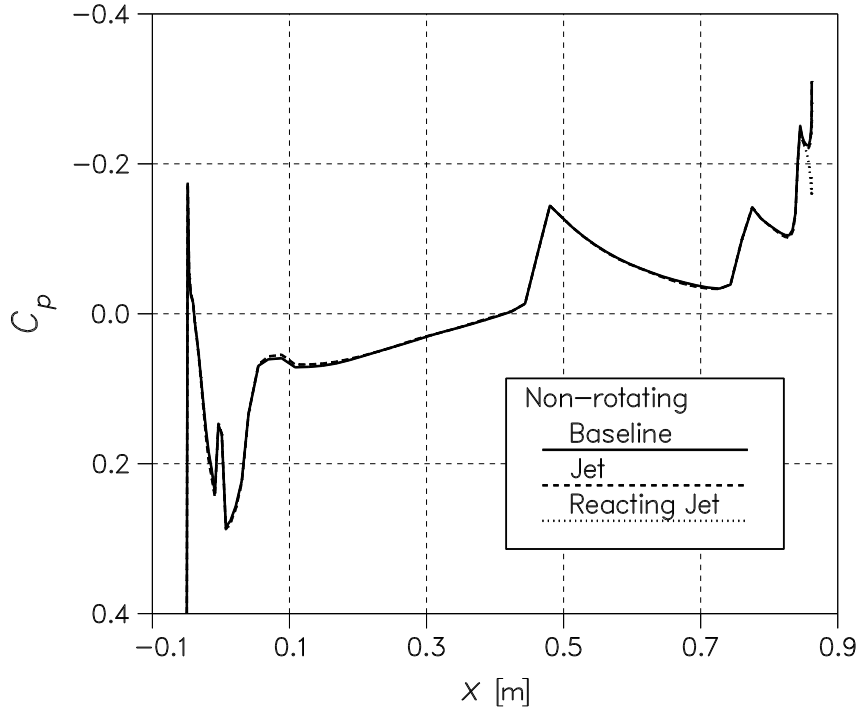

Fig. 5.4: Pressure coefficient distribution on the surface of the projectile. $Ma_\infty = 1.2$, $Re_D = 1.4 \cdot 10^6$, $\alpha = 0°$, $I = 0.0122$ and $\mathbf{\Omega} = 0$ rpm.

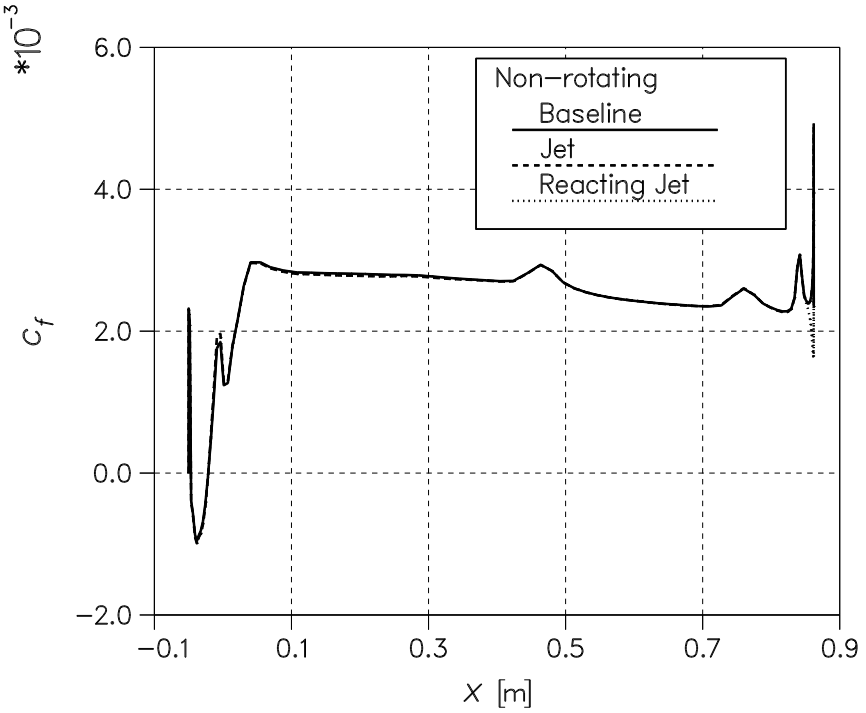

Fig. 5.5: Skin-friction coefficient c_f on the surface of the projectile. $Ma_\infty = 1.2$, $Re_D = 1.4 \cdot 10^6$, $\alpha = 0°$, $I = 0.0122$ and $\mathbf{\Omega} = 0$ rpm.

both differ slightly from the results from the reacting base-bleed simulations on the boattail of the projectile. This is obviously a consequence of the increased base pressure as seen in Figure 5.6.

Figure 5.6 shows the C_p-distribution on the plane of the base of the projectile according to all the non-rotating simulations, and Figure 5.7 shows the C_p-distribution inside the base-bleed unit for the same cases. According to Figures 5.6 and 5.7, the reaction model increases the pressure coefficient level inside the unit by approximately a constant value of 0.05, and at the base plane by 0.09. This explains the huge difference seen in C_D between the inert and reactive base-bleed flows.

It should be kept in mind here that, since the forces acting on the projectile are determined by integrating the momentum flux over the solid surface boundaries as well as the inlet boundary on the burning surface, the C_p-values in Figure 5.6 in the area $0 \leq r \leq 0.0247$ m do not directly contribute anything to the drag. Instead, it is the pressure on the base surface together with the pressure on the bottom of the base-bleed unit, as well as the pressure difference between the bottom and top surfaces of the unit, that constitute the base drag of this projectile. This, of course, is a matter of definition.

Figure 5.8 shows the axial velocity distribution at the base plane of the base-bleed nozzle exit. A small region of recirculating flow is present near the kink of the surface, but otherwise the velocity distribution is plain outflow from the unit. The velocities are lower for the reacting jet case, which is in harmony with the observed higher pressures at the base plane.

Figure 5.9 shows the Mach number distributions at the base plane of the base-bleed nozzle exit. According to this figure, the flow velocities are well below choked conditions.

Figure 5.10 shows the Mach number distribution together with the streamlines near the non-rotating projectile without base bleed. Figure 5.11 shows the C_p-distribution under the same circumstances. The scales of Ma and C_p are chosen to allow identical scales to be employed in the subsequent figures for other cases.

Figures 5.12 and 5.13 show the Mach number and C_p-distributions, respectively, for the non-rotating projectile with inert base bleed, and Figures 5.14 and 5.15 show the Mach number and C_p-distributions for the non-rotating projectile with reacting base bleed, respectively. As the Mach number figures show, the external flow field is unaffected by the base bleed and the base combustion. The shock wave patterns are practically identical with each other, and therefore all the other figures are focused on the base region.

Figures 5.13 and 5.15 show clearly how the main effect of the base combustion is to increase the pressure behind the base of the projectile, and thus reduce the aerodynamic drag. The streamlines also show some differences, especially the shape of the large recirculation region behind the base corner is changed, and the streamlines are displaced away from the symmetry axis. The primary recirculation zone is only slightly stretched downstream by the base combustion, and in both the inert and reactive base-bleed simulations the primary recirculation zone extends approximately $2/3 D_{\text{base}}$ aft of the base plane.

The temperature distributions for these cases shown in Figures 5.16 and 5.17

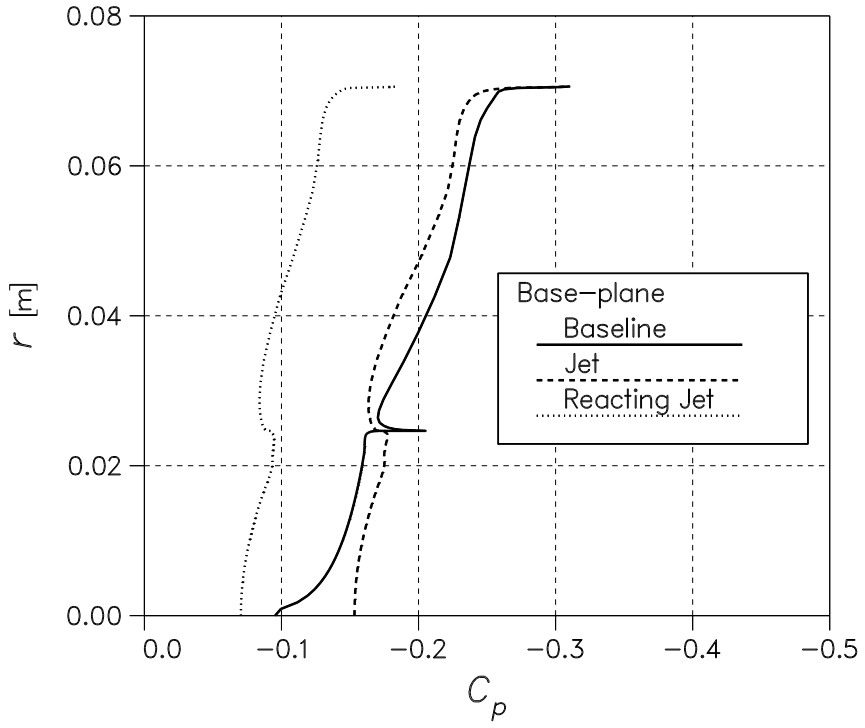

Fig. 5.6: Pressure coefficient distribution on the surface of the base of the projectile and at the base plane in the exit of the nozzle. $Ma_\infty = 1.2$, $Re_D = 1.4 \cdot 10^6$, $\alpha = 0°$, $I = 0.0122$ and $\mathbf{\Omega} = 0$ rpm.

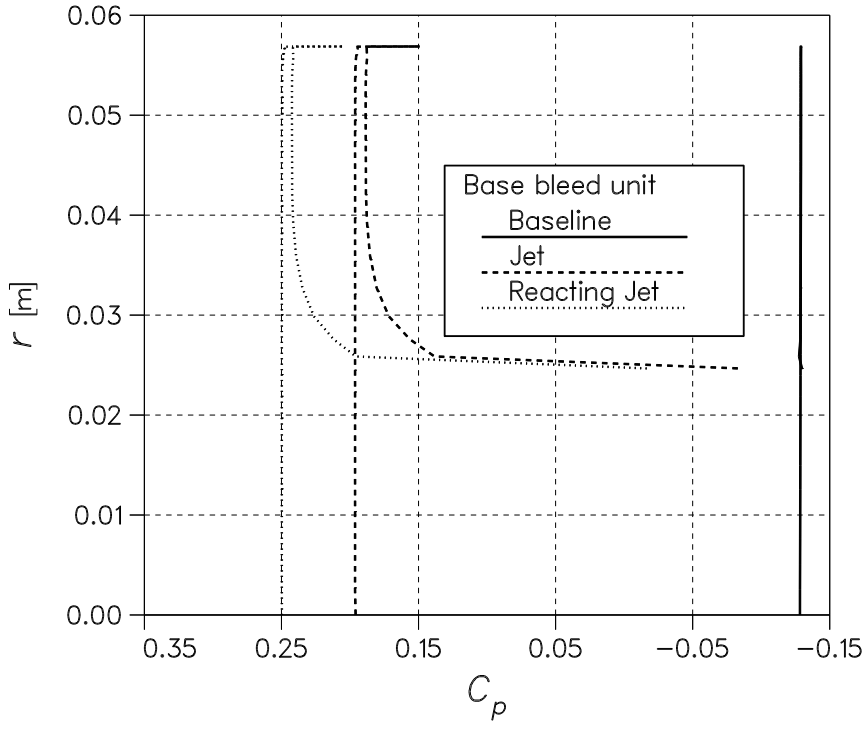

Fig. 5.7: Pressure coefficient distribution on the surface inside the base bleed unit. $Ma_\infty = 1.2$, $Re_D = 1.4 \cdot 10^6$, $\alpha = 0°$, $I = 0.0122$ and $\mathbf{\Omega} = 0$ rpm.

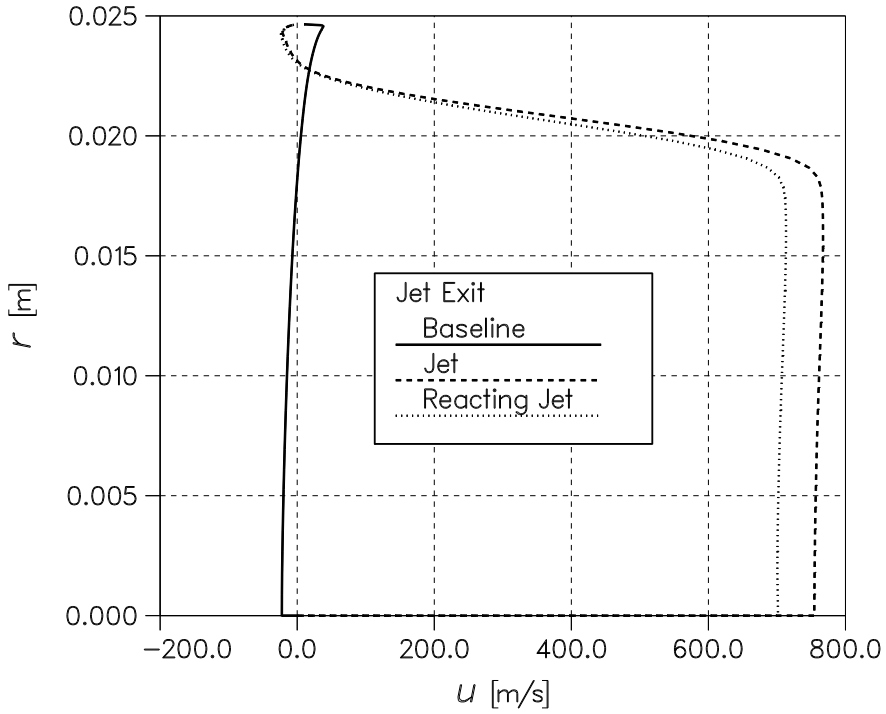

Fig. 5.8: Axial velocity distribution at the base plane in the exit of the nozzle. $Ma_\infty = 1.2$, $Re_D = 1.4 \cdot 10^6$, $\alpha = 0°$, $I = 0.0122$ and $\mathbf{\Omega} = 0$ rpm.

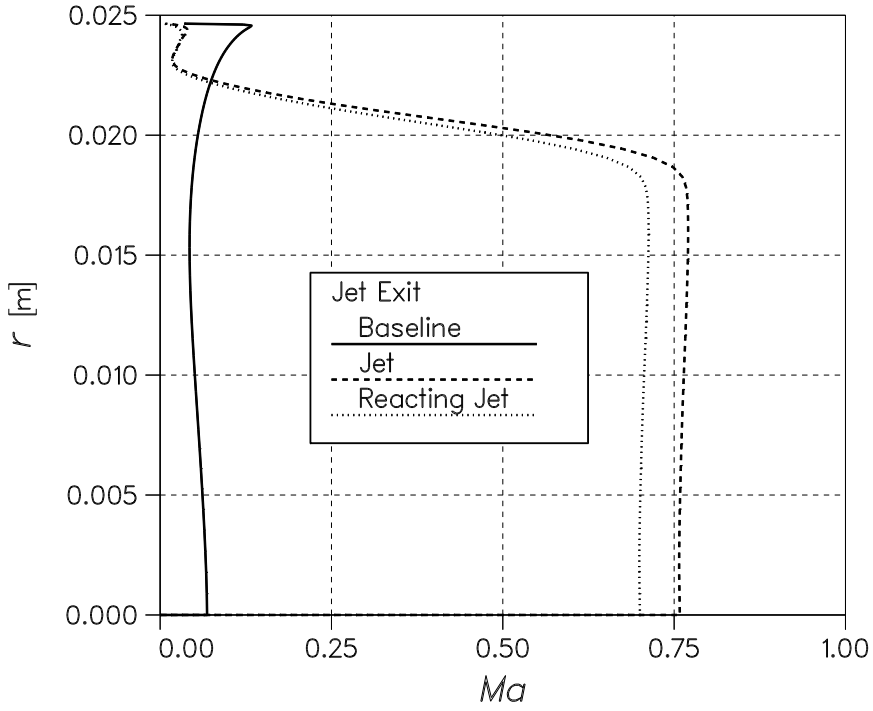

Fig. 5.9: Mach number distribution at the base plane in the exit of the nozzle. $Ma_\infty = 1.2$, $Re_D = 1.4 \cdot 10^6$, $\alpha = 0°$, $I = 0.0122$ and $\mathbf{\Omega} = 0$ rpm.

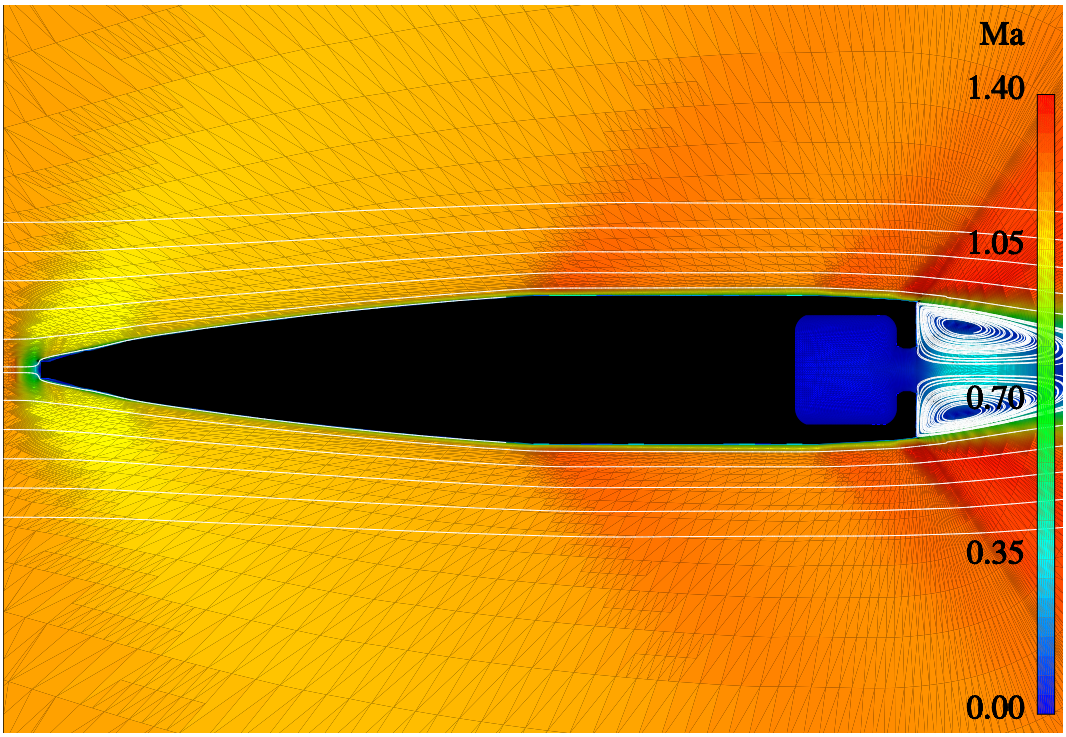

Fig. 5.10: The Mach number distribution and streamlines according to the non-rotating and inert flow field simulation without base bleed. $Ma_\infty = 1.2$, $Re_D = 1.4 \cdot 10^6$, $\alpha = 0°$, $I = 0$ and $\mathbf{\Omega} = 0$ rpm.

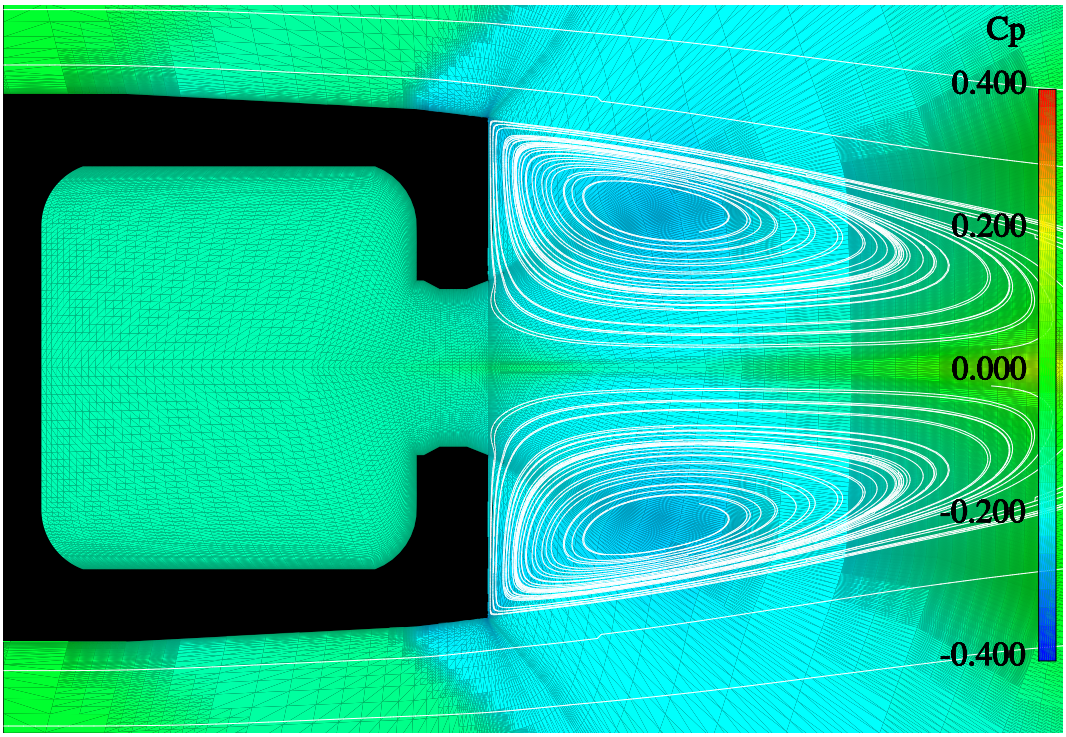

Fig. 5.11: The C_p distribution and streamlines according to the non-rotating and inert flow field simulation without base bleed. $Ma_\infty = 1.2$, $Re_D = 1.4 \cdot 10^6$, $\alpha = 0°$, $I = 0$ and $\mathbf{\Omega} = 0$ rpm.

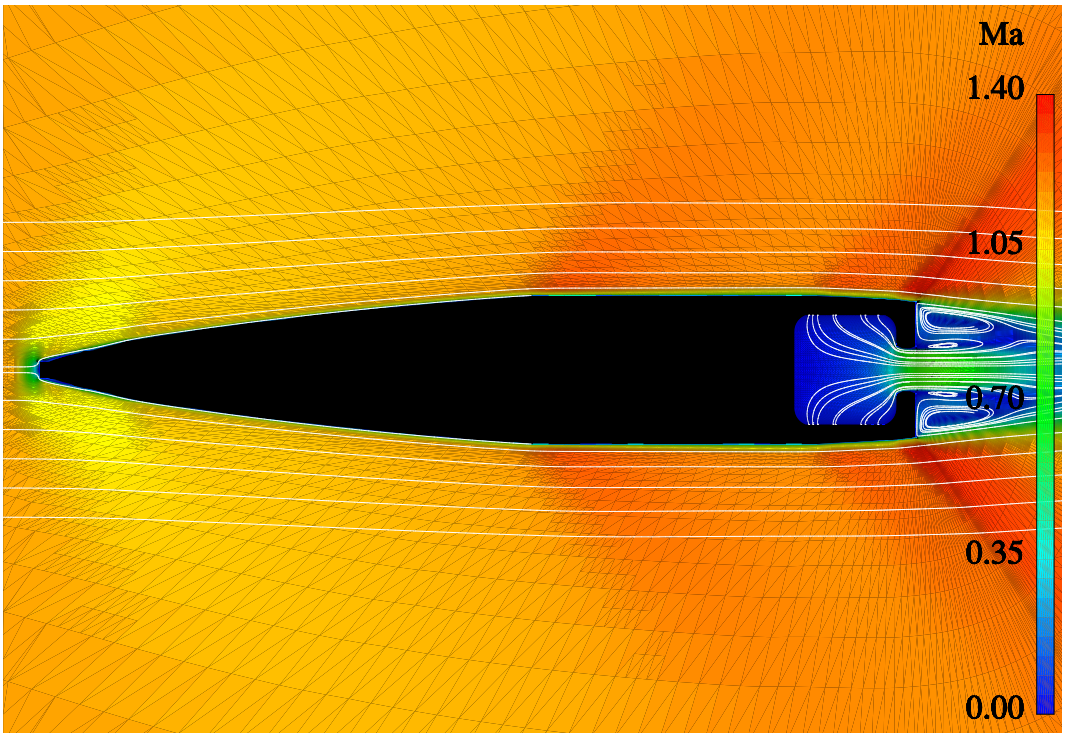

Fig. 5.12: The Mach number distribution and streamlines according to the non-rotating and inert flow field simulation. $Ma_\infty = 1.2$, $Re_D = 1.4 \cdot 10^6$, $\alpha = 0°$, $I = 0.0122$ and $\mathbf{\Omega} = 0$ rpm.

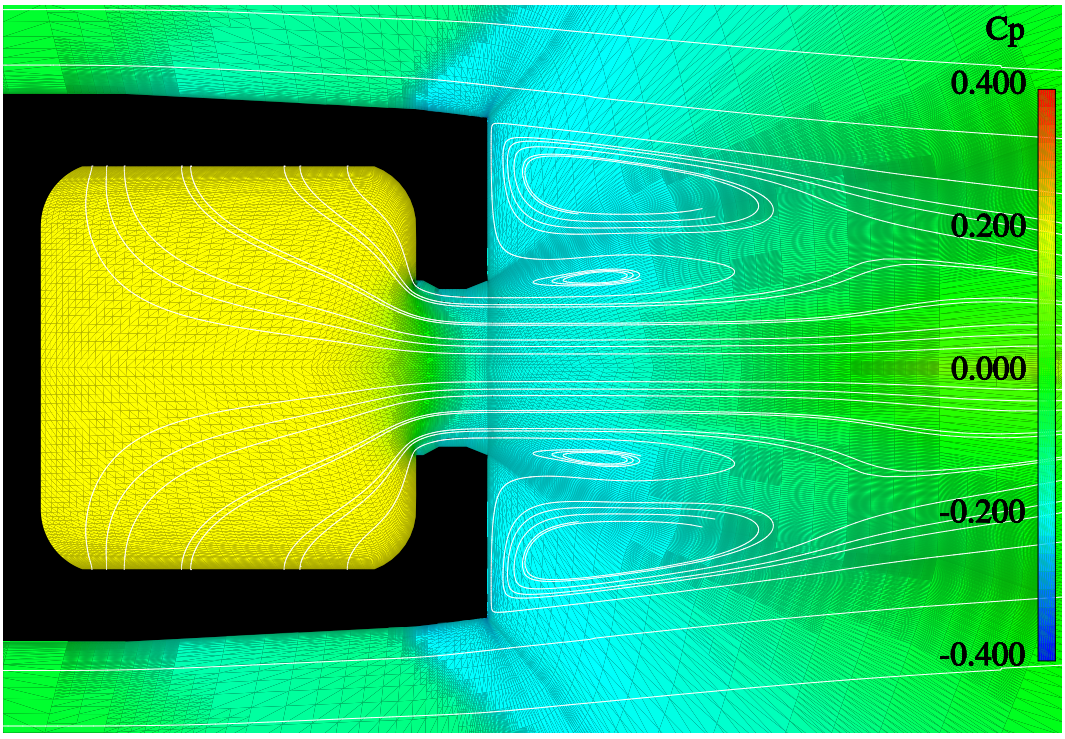

Fig. 5.13: The C_p distribution and streamlines according to the non-rotating and inert flow field simulation. $Ma_\infty = 1.2$, $Re_D = 1.4 \cdot 10^6$, $\alpha = 0°$, $I = 0.0122$ and $\mathbf{\Omega} = 0$ rpm.

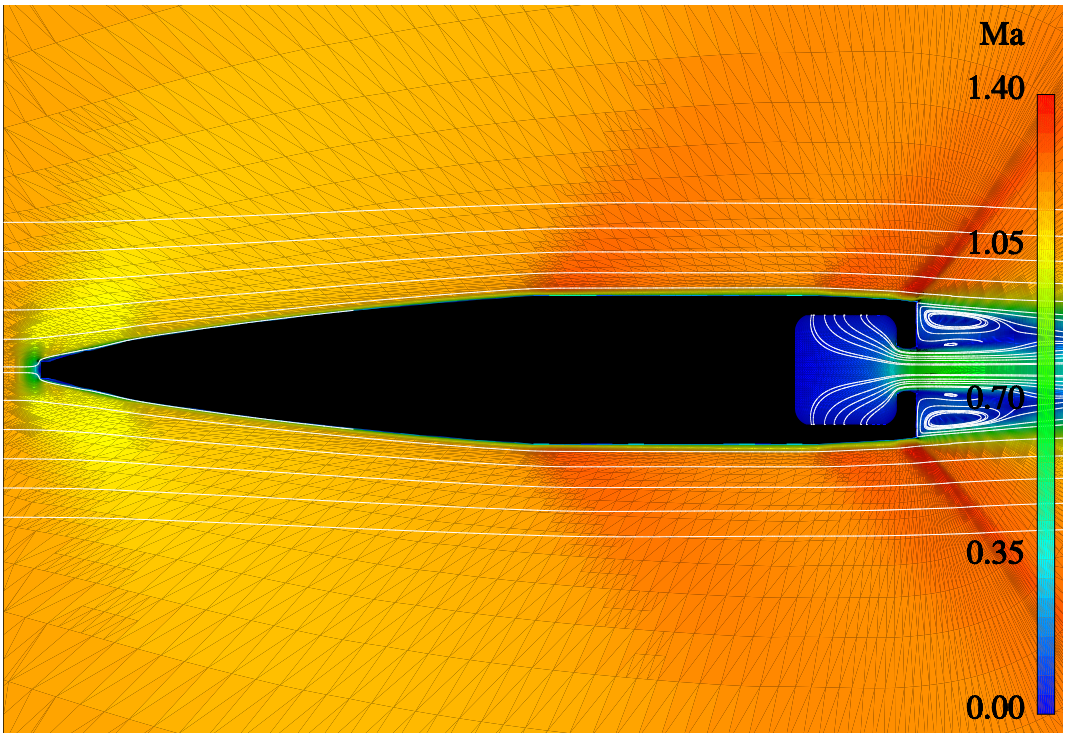

Fig. 5.14: The Mach number distribution and streamlines according to the non-rotating and reacting flow field simulation. $Ma_\infty = 1.2$, $Re_D = 1.4 \cdot 10^6$, $\alpha = 0°$, $I = 0.0122$ and $\mathbf{\Omega} = 0$ rpm.

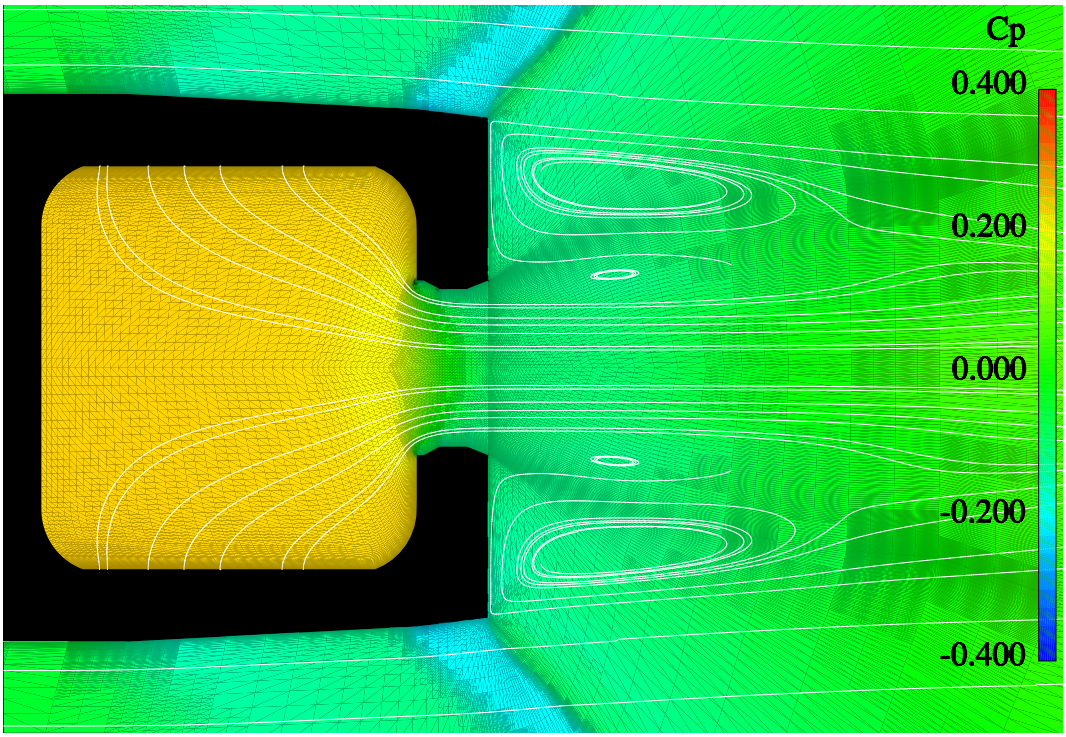

Fig. 5.15: The C_p distribution and streamlines according to the non-rotating and reacting flow field simulation. $Ma_\infty = 1.2$, $Re_D = 1.4 \cdot 10^6$, $\alpha = 0°$, $I = 0.0122$ and $\mathbf{\Omega} = 0$ rpm.

demonstrate the temperature increase caused by the base combustion. The reaction product mass fraction distribution, ϕ_{pr} for the non-rotating projectile is shown in Figure 5.18, and the corresponding reaction rate distribution is shown in Figure 5.19 using a logarithmic scale. When comparing these figures with each other, it can be seen that the highest temperatures occur in the secondary recirculation zone just behind the base-bleed nozzle exit. The reaction rate is highest at the outer edge of the secondary recirculation zone, which is understandable, because that is where the free-stream flow first meets the base-bleed jet.

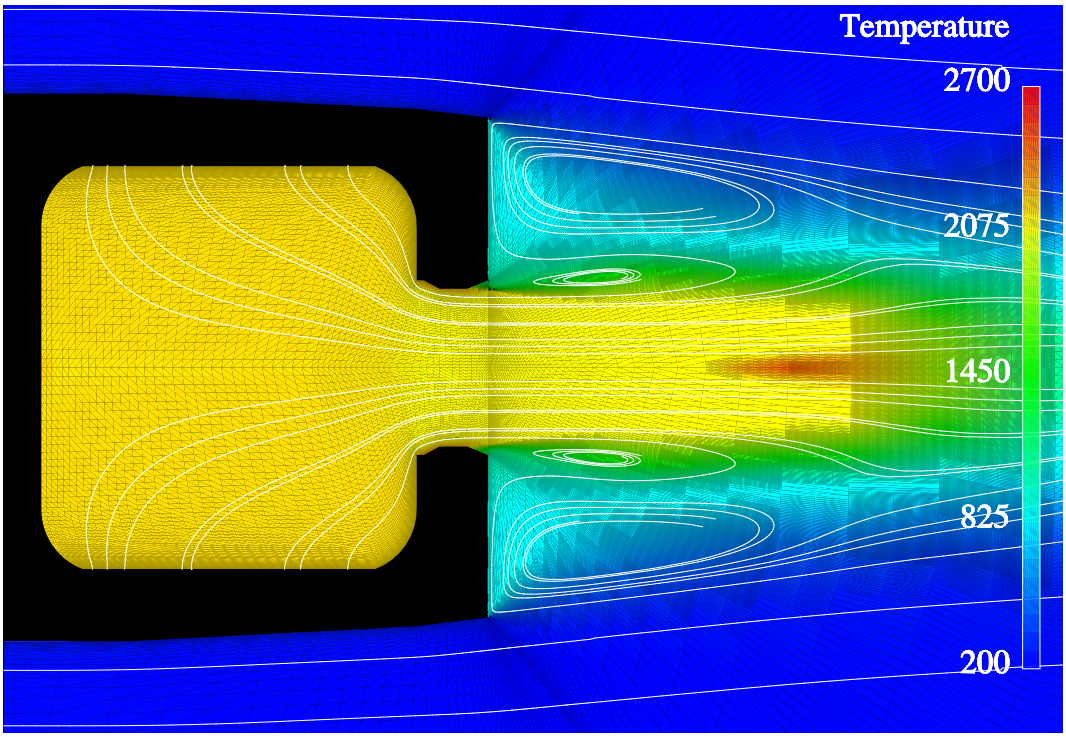

Fig. 5.16: The temperature distribution [K] and streamlines according to the non-rotating and inert flow field simulation. $Ma_\infty = 1.2$, $Re_D = 1.4 \cdot 10^6$, $\alpha = 0°$, $I = 0.0122$ and $\mathbf{\Omega} = 0$ rpm.

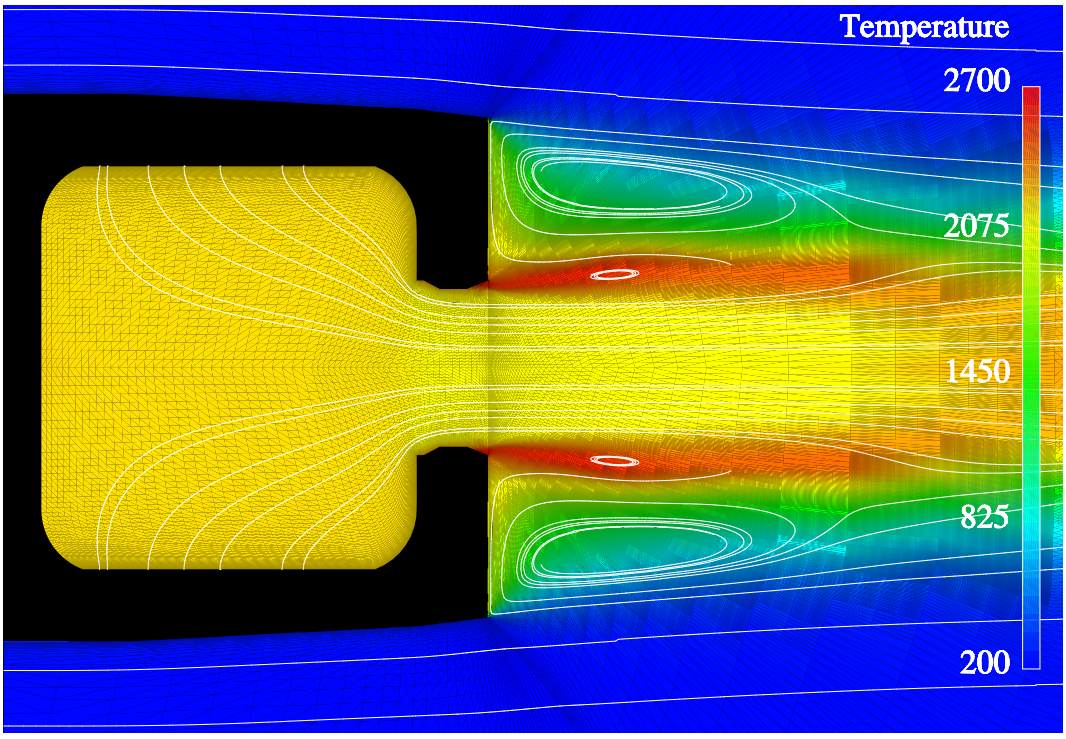

Fig. 5.17: The temperature distribution [K] and streamlines according to the non-rotating and reacting flow field simulation. $Ma_\infty = 1.2$, $Re_D = 1.4 \cdot 10^6$, $\alpha = 0°$, $I = 0.0122$ and $\mathbf{\Omega} = 0$ rpm.

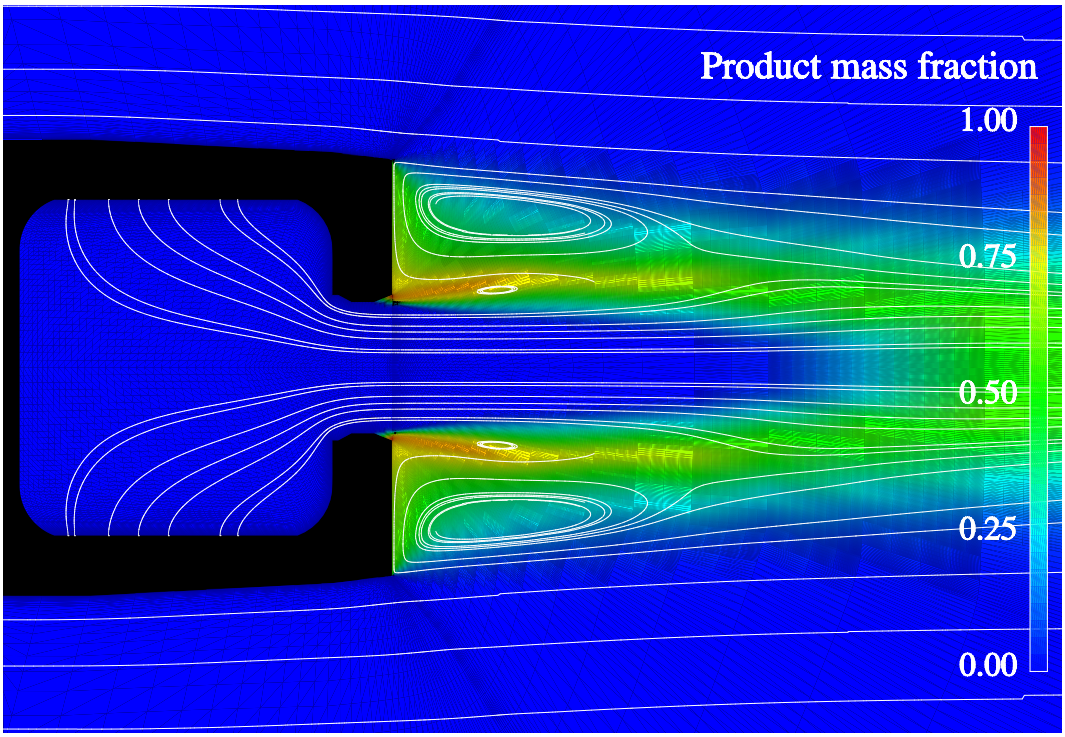

Fig. 5.18: The reaction product mass fraction ϕ_{pr} distribution and streamlines. $Ma_\infty = 1.2$, $Re_D = 1.4 \cdot 10^6$, $\alpha = 0°$, $I = 0.0122$ and $\boldsymbol{\Omega} = 0$ rpm.

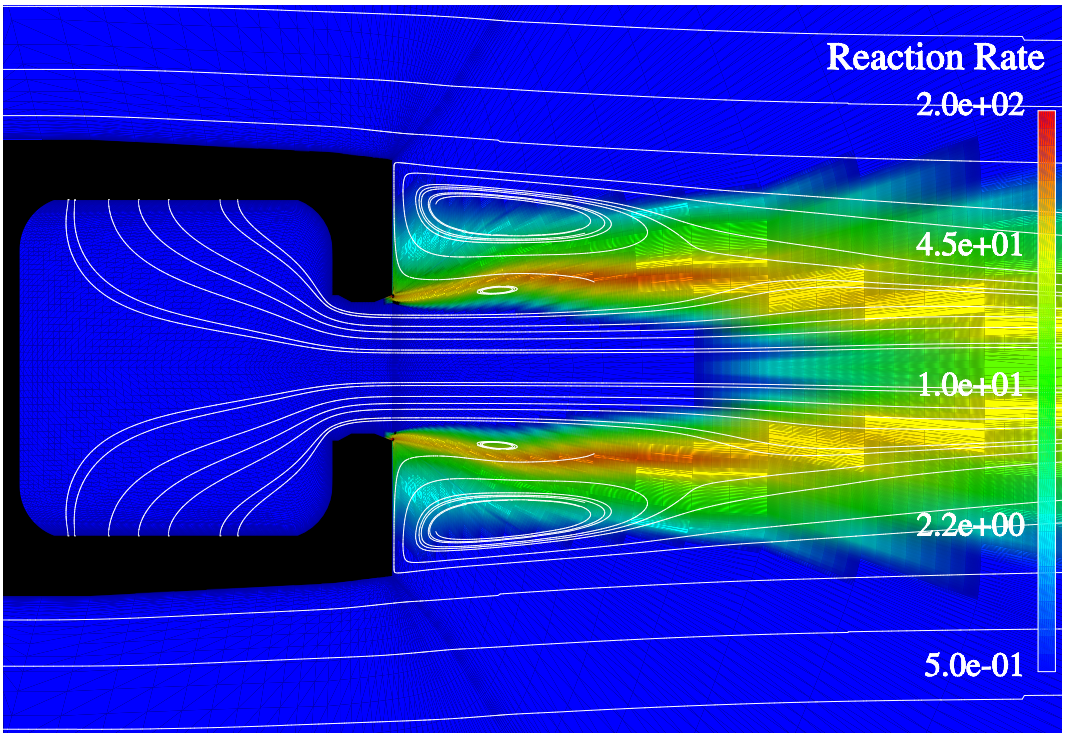

Fig. 5.19: The reaction rate Q_{pr} distribution [kg/(m^{3}s)] and streamlines. $Ma_\infty = 1.2$, $Re_D = 1.4 \cdot 10^6$, $\alpha = 0°$, $I = 0.0122$ and $\boldsymbol{\Omega} = 0$ rpm.

5.2 Rotating Projectile

The simulations with the rotating projectile add one step more realism to the simulations described in the previous section. As the C_D-results in Table 5.1 show, no dramatic changes are introduced to the drag predictions by the rotation of the projectile. The C_p-distributions on the surface of the projectile according to the rotating and non-rotating projectile simulations without base bleed are shown in Figure 5.20, and a comparison between the c_f-values for the rotating and non-rotating baseline projectile is shown in Figure 5.21.

The clearest difference is that the C_p-values of the rotating projectile are higher than those of the non-rotating projectile. The c_f-values show a similar change, and as a consequence these changes increase the drag of the rotating projectile. The C_p-values on the base plane presented in Figure 5.22 show, however, a similar difference in favour of the rotating projectile, and therefore equal C_D-values are obtained for both of the cases. The difference is explained by the larger turbulent viscosities in the rotating case, as demonstrated by Figure 5.23, which shows μ_T/μ at $x = 0.3$ m. The higher turbulent viscosities of the rotating case increase the total shear stress, and consequently also the wall shear stress. The higher stresses make the boundary layer thicker, which in turn changes the pressure coefficient.

According to the simulations with the rotating projectile, the base bleed has a small effect on the pressure and the skin-friction distribution on the surface of the shell. Figure 5.24 shows the C_p-distribution on the surface of the rotating shell according to the simulations without base bleed, with inert base bleed, and with reactive base bleed. Figure 5.25 shows the c_f-distribution for the same cases.

In both of these figures, both of the results from simulations with base bleed are indistinguishable from each other, and they both differ slightly from the no-base-bleed simulations labelled as “Baseline”. Clearly, this effect has nothing to do with the chemistry modelling, but it is a phenomenon caused by the rotating base-bleed jet. On the boattail of the projectile, however, there is a similar difference between the results from the reacting base-bleed simulations and the other simulations as observed with the non-rotating projectile.

The interesting detail in Figure 5.24 is how the pressure is affected in the upstream direction by the changes of the flow field near the base. Even though the difference is small, it is clear and distinct. This information has to be transferred via the boundary layer, because elsewhere the flow is supersonic, and information cannot travel in the upstream direction.

Figure 5.26 shows the C_p-distribution on the surface of the base of the rotating projectile according to the simulations without base bleed, with inert base bleed, and reactive base bleed. Figure 5.27 shows the C_p-distribution inside the base-bleed unit for the same cases. The same trend of increasing the pressure levels by the chemical reactions as was observed with the non-rotating case is seen again with the rotating case. Again, the pressure contributions of the front and back wall of the inside of the base-bleed unit almost cancel each other, and the net contribution to C_D comes from the pressure in the middle of the bottom of the unit as well as the base plane of the projectile.

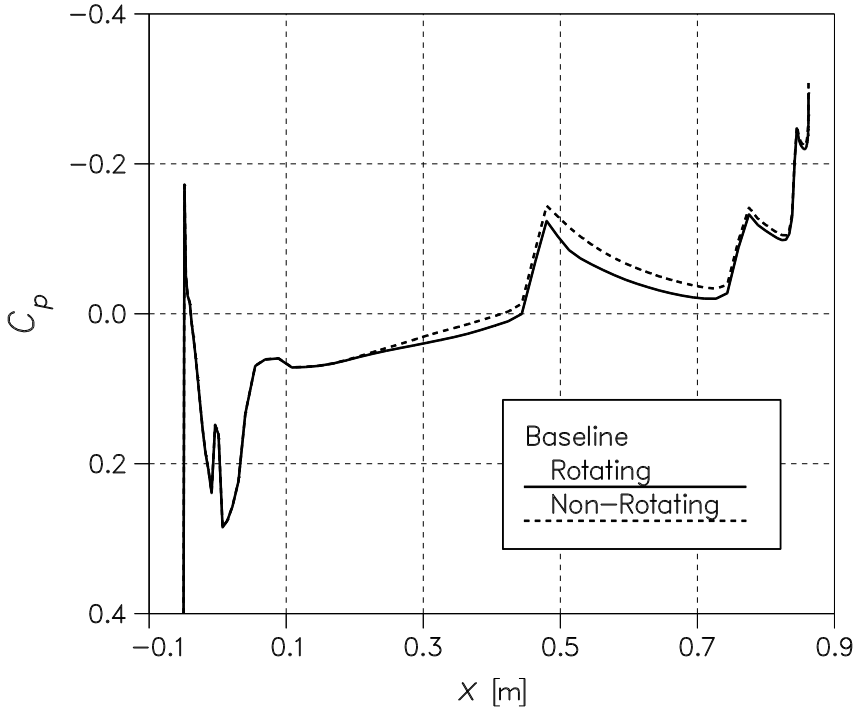

Fig. 5.20: Comparison of the effects of rotation on the pressure coefficient distribution on the surface of the projectile. $Ma_\infty = 1.2$, $Re_D = 1.4 \cdot 10^6$, $\alpha = 0°$ and $I = 0$.

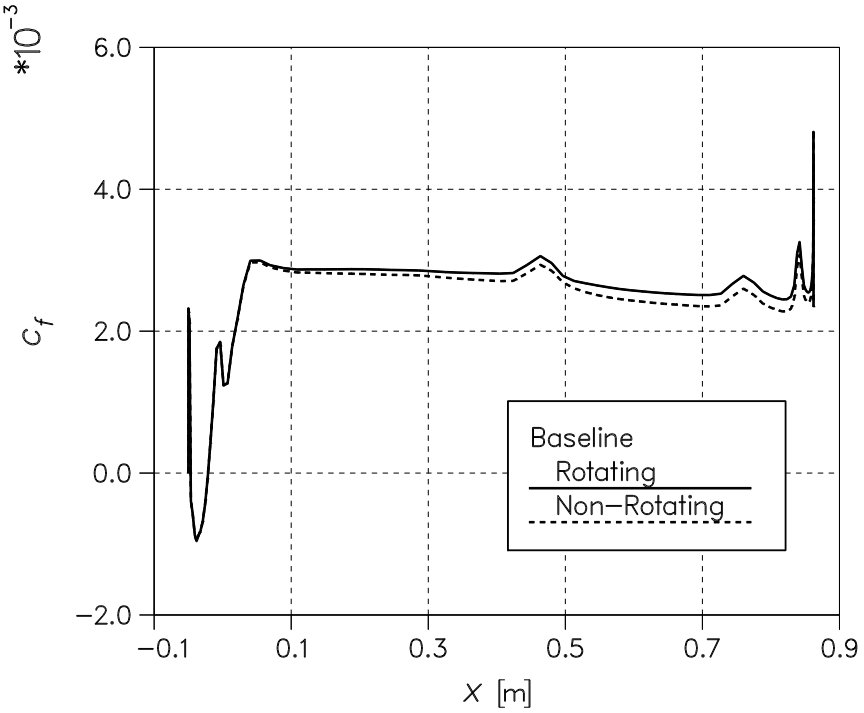

Fig. 5.21: Comparison of the effects of rotation on the skin-friction coefficient c_f on the surface of the projectile. $Ma_\infty = 1.2$, $Re_D = 1.4 \cdot 10^6$, $\alpha = 0°$ and $I = 0$.

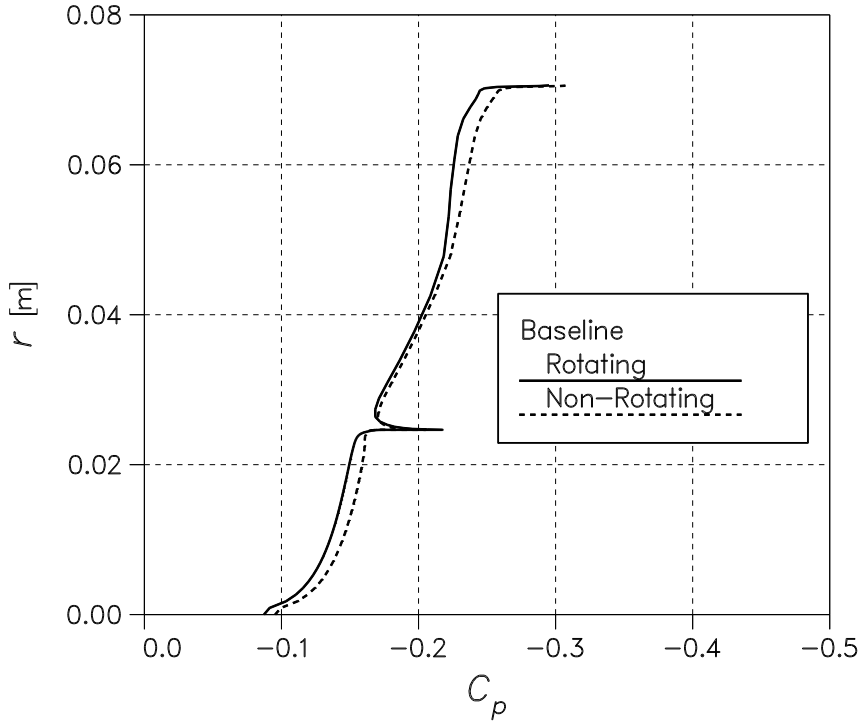

Fig. 5.22: Comparison of the effects of rotation on the pressure coefficient distribution on the surface of the base of the projectile and the base plane in the exit of the nozzle. $Ma_\infty = 1.2$, $Re_D = 1.4 \cdot 10^6$, $\alpha = 0°$ and $I = 0$.

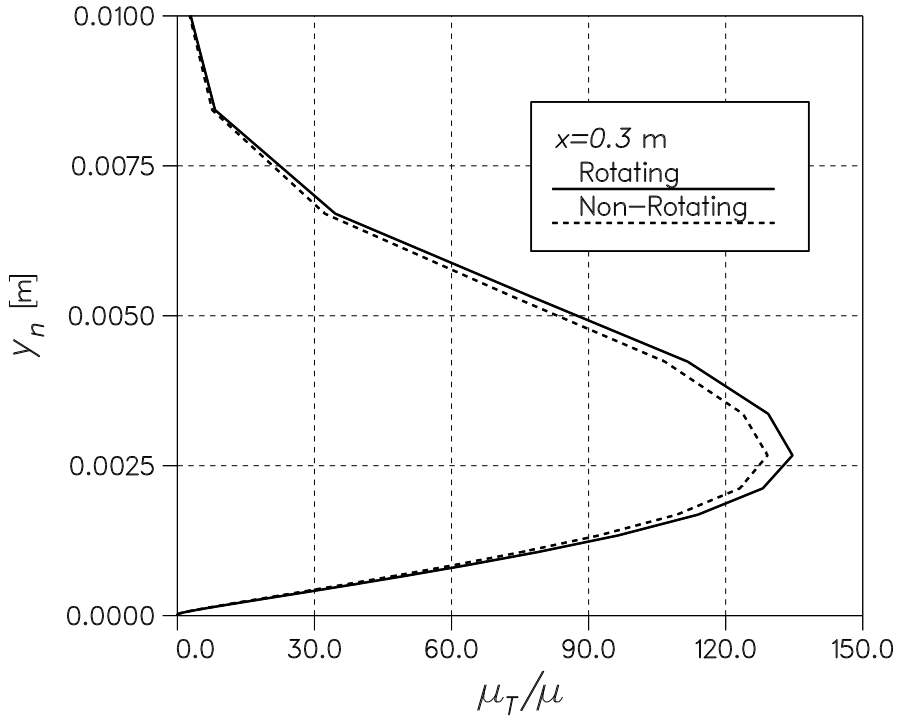

Fig. 5.23: Comparison of the effects of rotation on the turbulent viscosity at $x = 0.3$ m. $Ma_\infty = 1.2$, $Re_D = 1.4 \cdot 10^6$, $\alpha = 0°$ and $I = 0$.

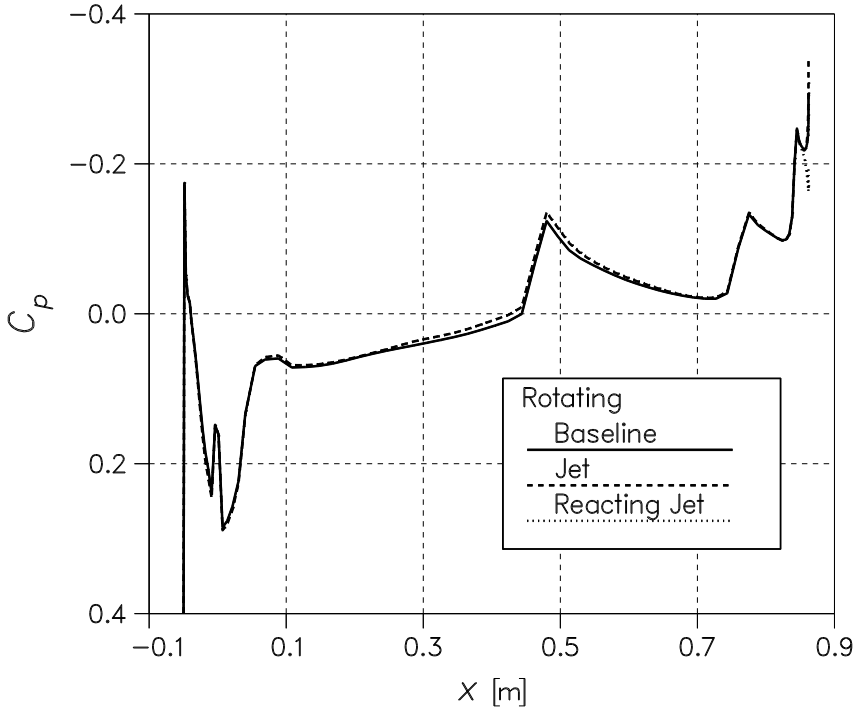

Fig. 5.24: Pressure coefficient distribution on the surface of the projectile. $Ma_\infty = 1.2$, $Re_D = 1.4 \cdot 10^6$, $\alpha = 0°$, $I = 0.0122$ and $\mathbf{\Omega} = 18\,000$ rpm.

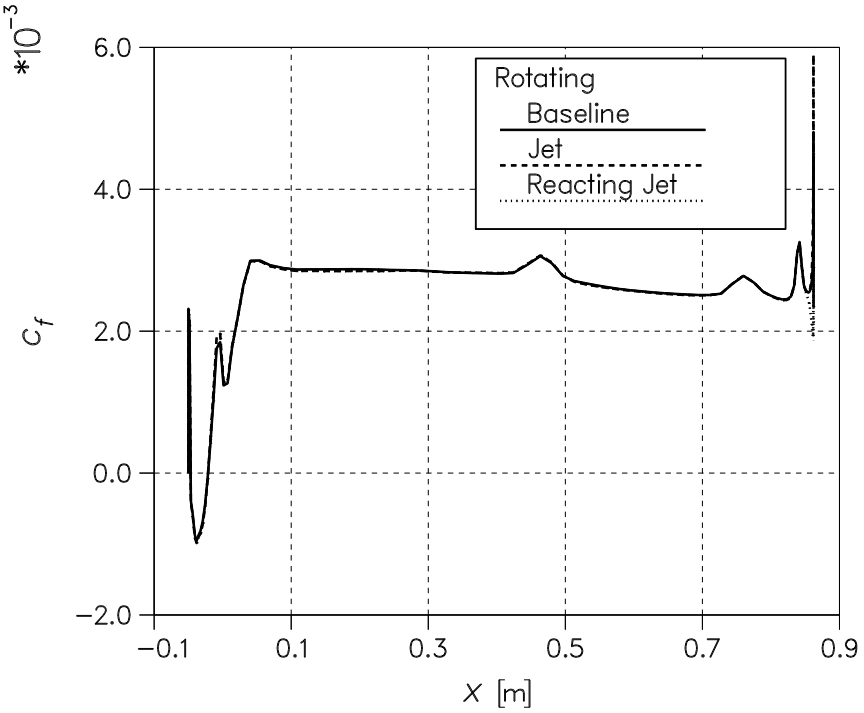

Fig. 5.25: Skin-friction coefficient c_f on the surface of the projectile. $Ma_\infty = 1.2$, $Re_D = 1.4 \cdot 10^6$, $\alpha = 0°$, $I = 0.0122$ and $\mathbf{\Omega} = 18\,000$ rpm.

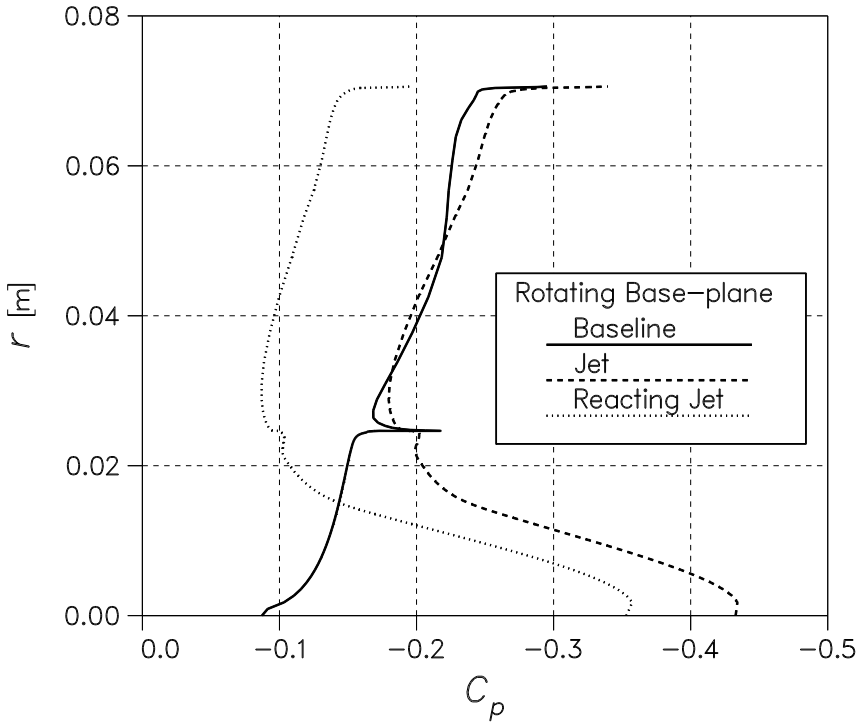

Fig. 5.26: Pressure coefficient distribution on the surface of the base of the projectile and at the base plane in the exit of the nozzle. $Ma_\infty = 1.2$, $Re_D = 1.4 \cdot 10^6$, $\alpha = 0°$, $I = 0.0122$ and $\mathbf{\Omega} = 18\,000$ rpm.

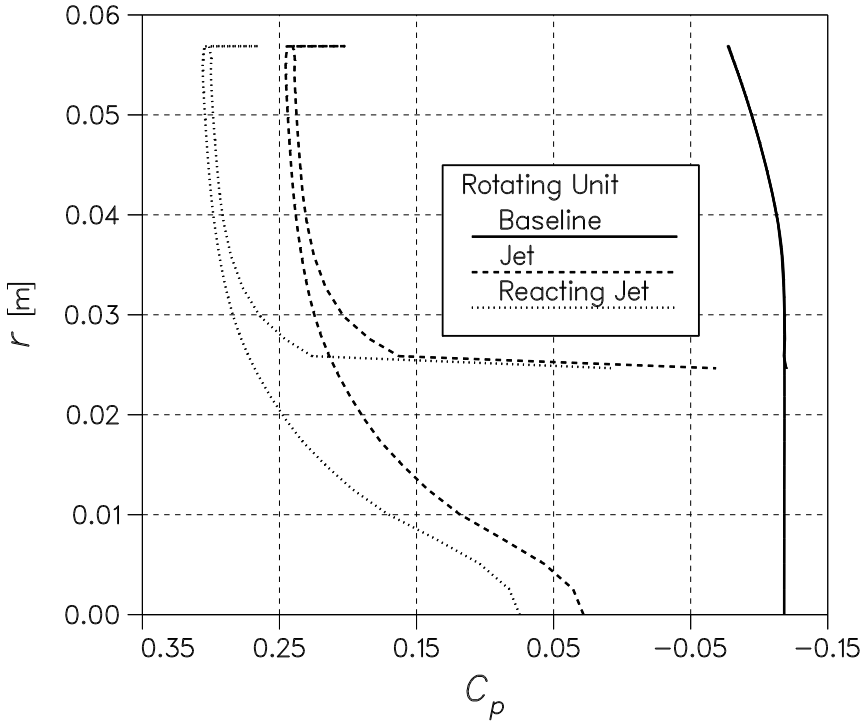

Fig. 5.27: Pressure coefficient distribution on the surface inside the base-bleed unit. $Ma_\infty = 1.2$, $Re_D = 1.4 \cdot 10^6$, $\alpha = 0°$, $I = 0.0122$ and $\mathbf{\Omega} = 18\,000$ rpm.

Figure 5.28 shows the axial velocity profiles at the base plane of the base-bleed nozzle exit. The velocities of the base-bleed cases are higher than those seen from the results of the non-rotating simulations.

Figure 5.29 shows the tangential velocity component at the base plane of the base-bleed nozzle exit, and Figure 5.30 shows the swirl angle of the flow at the same cross-section. The swirl angle is defined here by

$$\theta = \arctan\left(\frac{V_t}{u}\right) \tag{5.6}$$

where u is the axial velocity component. The angles higher than 90° are caused by the reverse flow

Figure 5.31 shows the Mach number distribution in the exit plane. The highest values in the non-reacting case are just below 1, which means the flow might be close to choking. The large swirl component of the velocity, however, makes the Mach number normal to the exit plane clearly below unity, which removes the problems of choked flow. Close to the centreline, however, θ is small, and the Mach number shown in Figure 5.31 is only slightly higher than the Mach number normal to the exit plane.

Figure 5.32 shows the Mach number distribution together with the streamlines near the rotating projectile without base bleed. The C_p-distribution is depicted in Figure 5.33 under the same circumstances. The scales of Ma and C_p are the same as employed in the figures describing the non-rotating projectile. In these and all the subsequent figures, the plotted streamlines are constrained to remain in the plane of visualization, so that the swirl velocity is suppressed when integrating the streamlines. Since the cases are axisymmetric, this causes no direct errors to the figures, but the streamlines are still false streamlines.

Figures 5.34 and 5.35 show the Mach number and C_p-distributions, respectively, for the rotating projectile with inert base bleed, and Figures 5.36 and 5.37 depict the Mach number and C_p-distributions for the rotating projectile with reacting base bleed, respectively. The radial pressure gradient inside the base-bleed unit caused by rotation is clearly seen from these figures.

Figures 5.35 and 5.37 show again how the main effect of the base combustion is to increase the pressure behind the base of the projectile. The streamlines show only some minor differences, but in comparison with the non-rotating flow cases, there are major differences. The recirculation zones are much shorter, and the jet spreading due to rotation is evident from the angle between the secondary recirculation region and the symmetry axis.

The temperature distributions for these cases shown in Figures 5.38 and 5.39 demonstrate the temperature increase caused by the base combustion. The reaction product mass fraction distribution, ϕ_{pr} for the rotating projectile is shown in Figure 5.40, and the corresponding reaction rate distribution is shown in Figure 5.41 using again a logarithmic scale. As with the non-rotating projectile, the highest temperatures occur in the secondary recirculation zone just behind the base-bleed nozzle exit. The temperature decrease occurs now in a shorter region than in the non-rotating simulations, which is a consequence of the shorter recirculation zones.

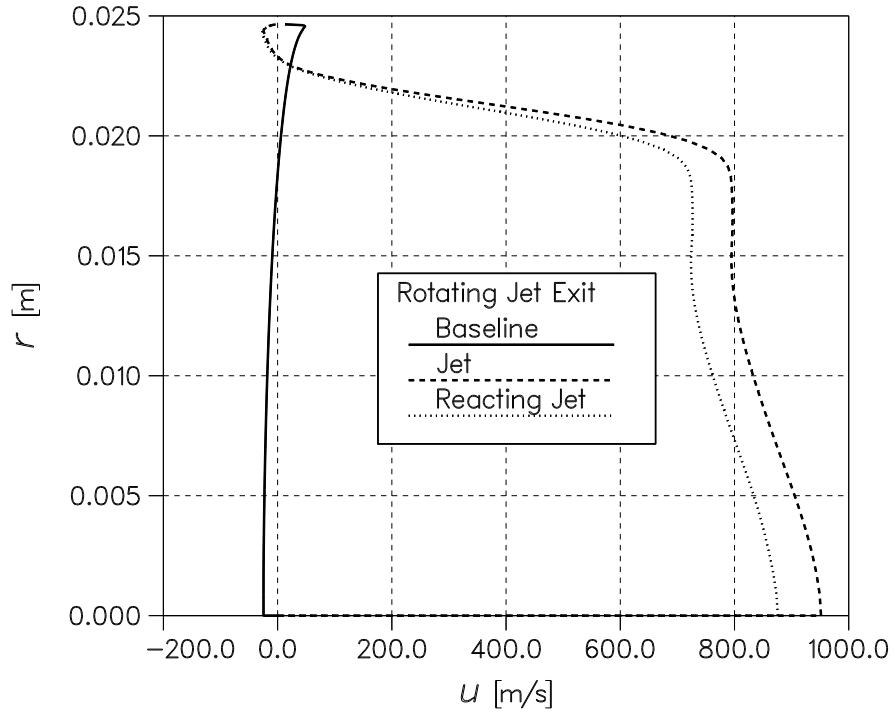

Fig. 5.28: Axial velocity distribution at the base plane in the exit of the nozzle. $Ma_\infty = 1.2$, $Re_D = 1.4 \cdot 10^6$, $\alpha = 0°$, $I = 0.0122$ and $\mathbf{\Omega} = 18\,000$ rpm.

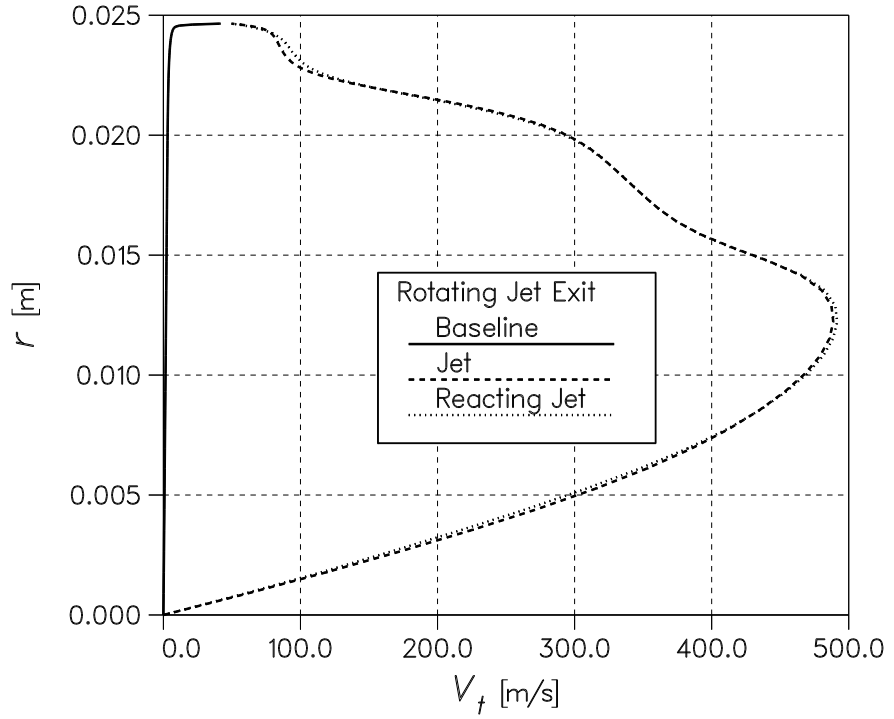

Fig. 5.29: Tangential velocity distribution at the base plane in the exit of the nozzle. $Ma_\infty = 1.2$, $Re_D = 1.4 \cdot 10^6$, $\alpha = 0°$, $I = 0.0122$ and $\mathbf{\Omega} = 18\,000$ rpm.

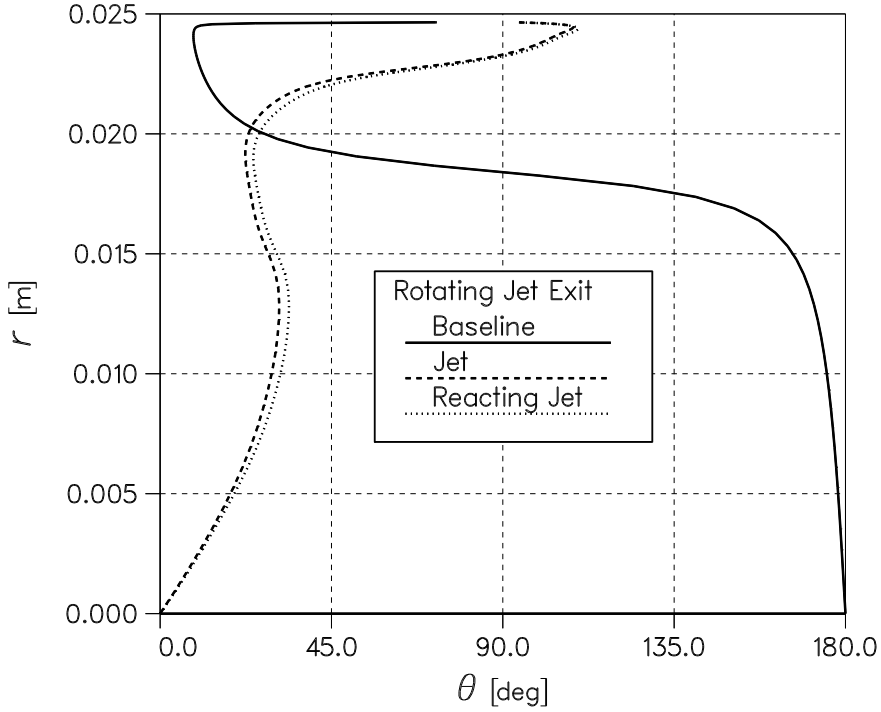

Fig. 5.30: Flow swirl angle θ at the base plane in the exit of the nozzle. $Ma_\infty = 1.2$, $Re_D = 1.4{\cdot}10^6$, $\alpha = 0°$, $I = 0.0122$ and $\mathbf{\Omega} = 18\,000$ rpm.

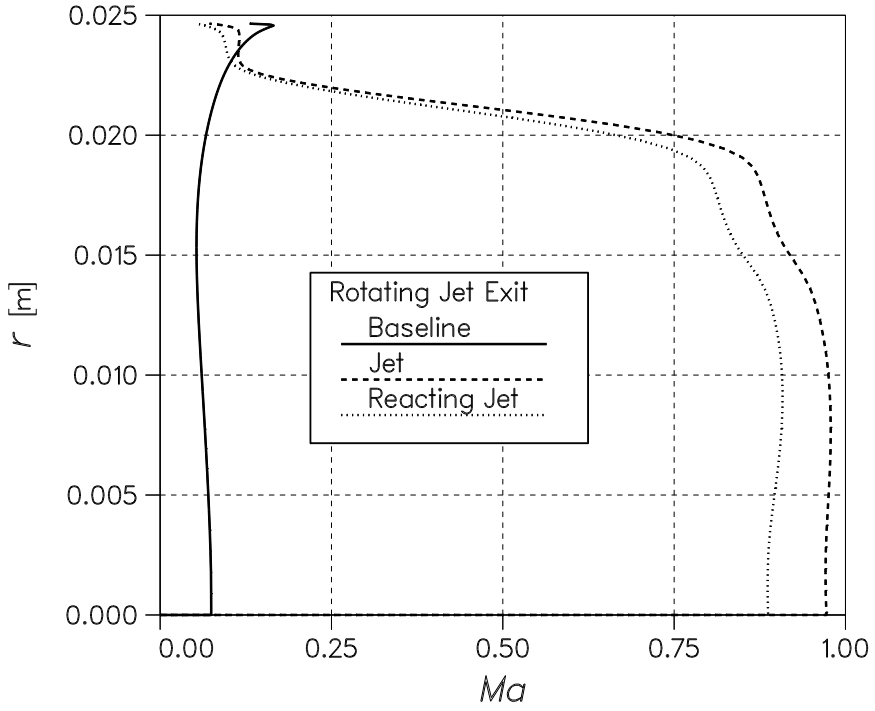

Fig. 5.31: Mach number distribution at the base plane in the exit of the nozzle. $Ma_\infty = 1.2$, $Re_D = 1.4 \cdot 10^6$, $\alpha = 0°$, $I = 0.0122$ and $\mathbf{\Omega} = 18\,000$ rpm.

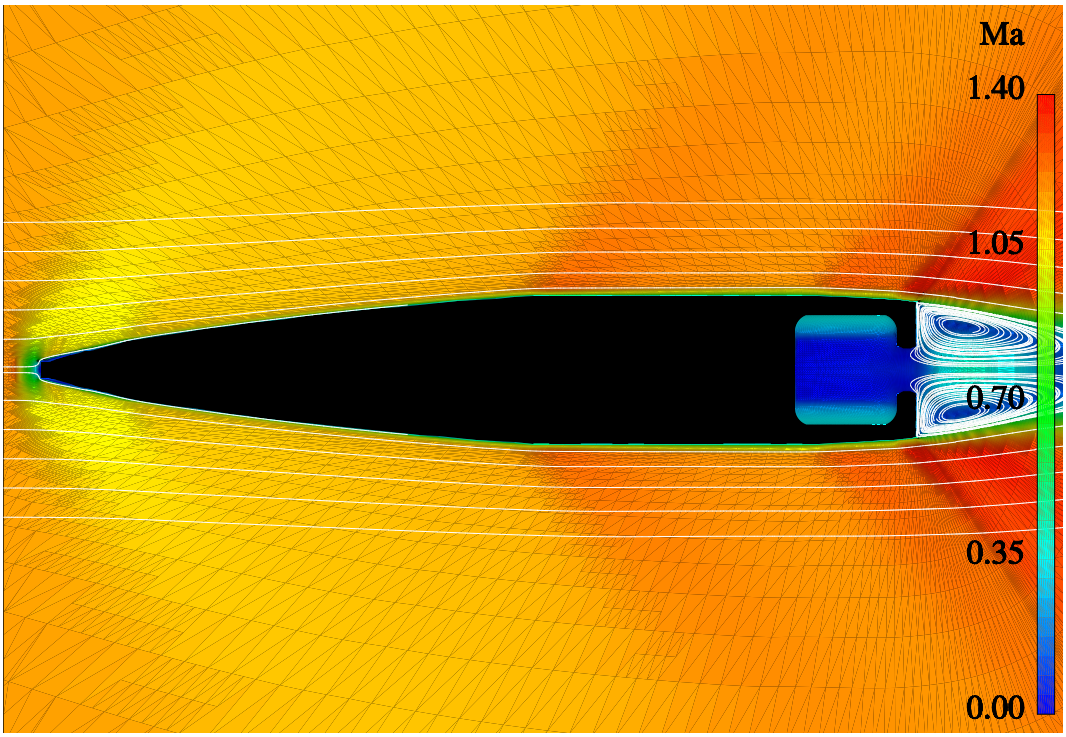

Fig. 5.32: The Mach number distribution and streamlines according to the rotating and inert flow field simulation without base bleed. $Ma_\infty = 1.2$, $Re_D = 1.4 \cdot 10^6$, $\alpha = 0°$, $I = 0$ and $\mathbf{\Omega} = 18\,000$ rpm.

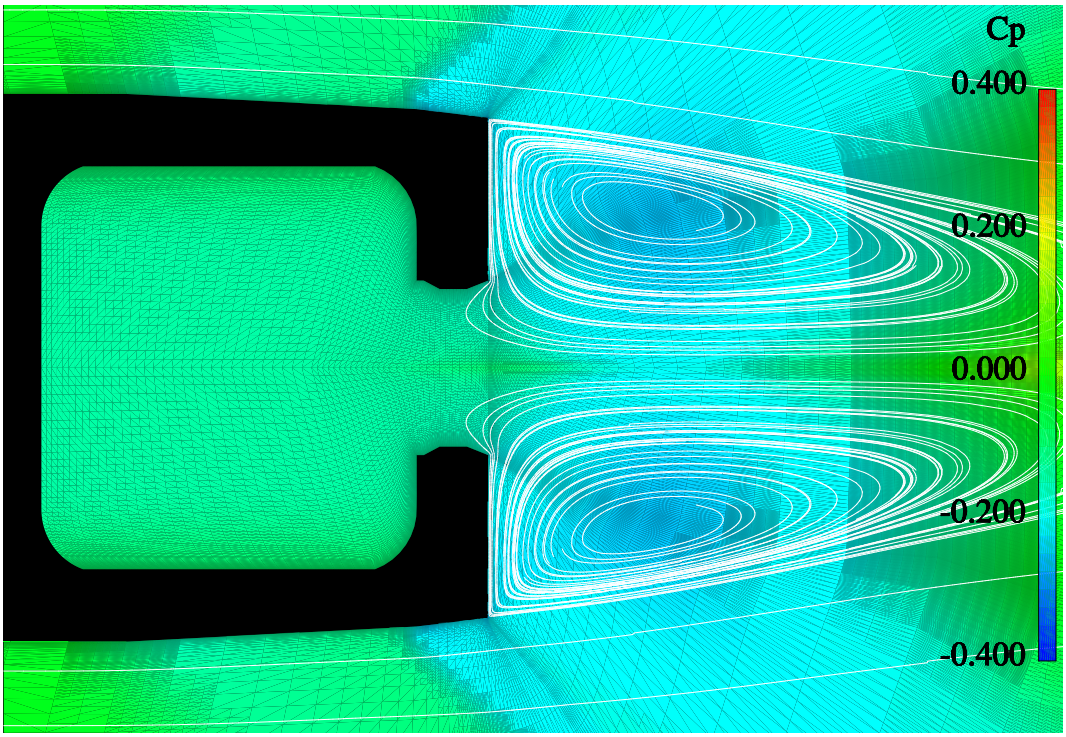

Fig. 5.33: The C_p distribution and streamlines according to the rotating and inert flow field simulation without base bleed. $Ma_\infty = 1.2$, $Re_D = 1.4 \cdot 10^6$, $\alpha = 0°$, $I = 0$ and $\mathbf{\Omega} = 18\,000$ rpm.

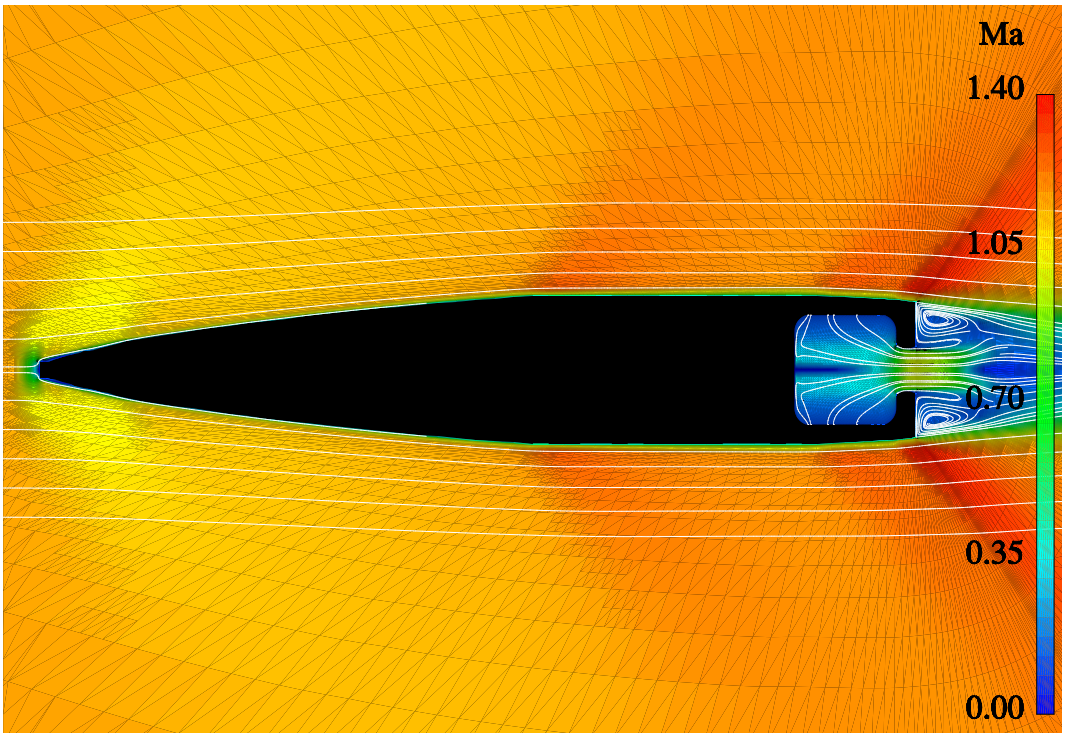

Fig. 5.34: The Mach number distribution and streamlines according to the rotating and inert flow field simulation. $Ma_\infty = 1.2$, $Re_D = 1.4 \cdot 10^6$, $\alpha = 0°$, $I = 0.0122$ and $\mathbf{\Omega} = 18\,000$ rpm.

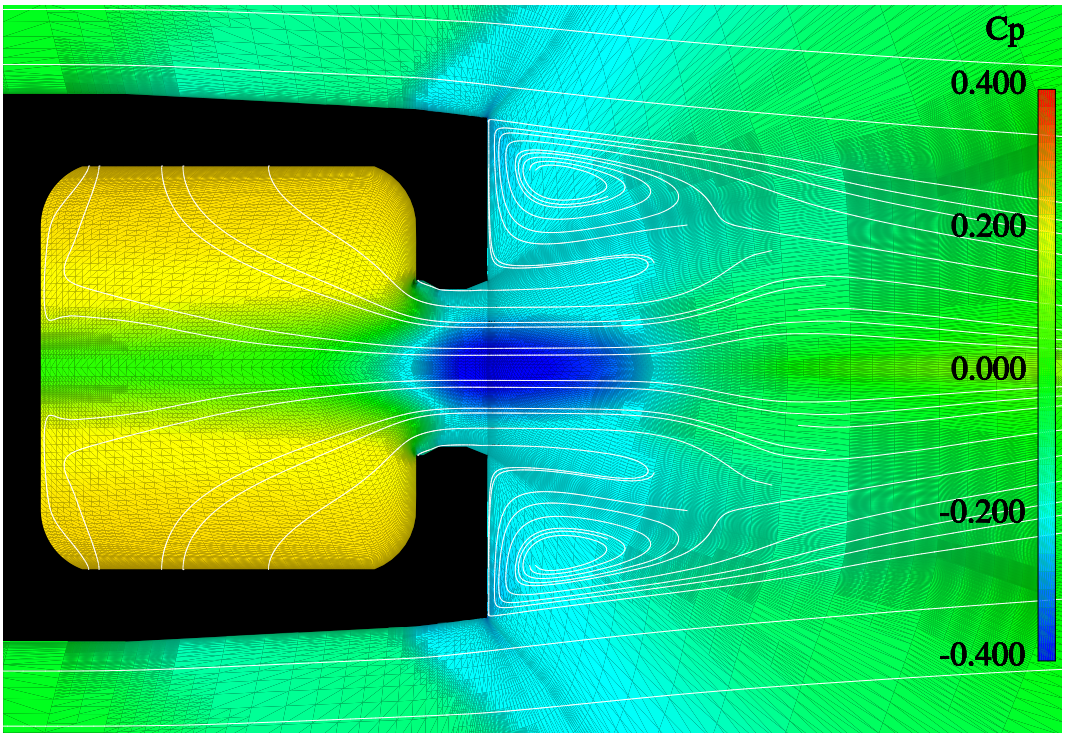

Fig. 5.35: The C_p distribution and streamlines according to the rotating and inert flow field simulation. $Ma_\infty = 1.2$, $Re_D = 1.4 \cdot 10^6$, $\alpha = 0°$, $I = 0.0122$ and $\mathbf{\Omega} = 18\,000$ rpm.

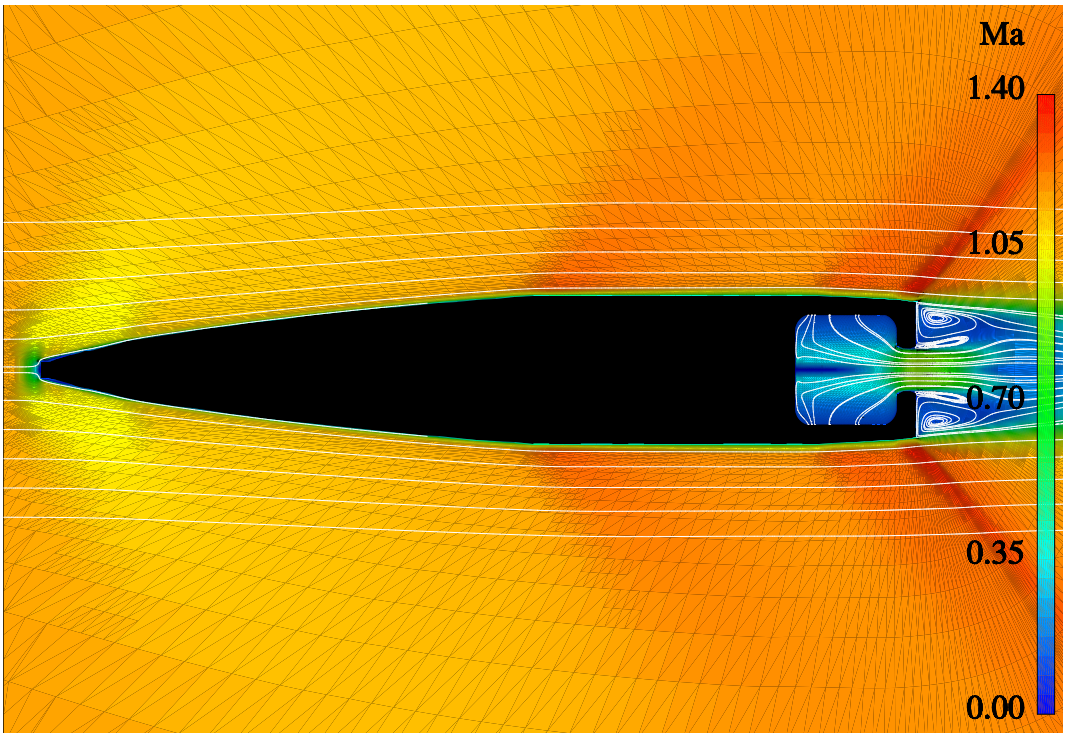

Fig. 5.36: The Mach number distribution and streamlines according to the rotating and reacting flow field simulation. $Ma_\infty = 1.2$, $Re_D = 1.4 \cdot 10^6$, $\alpha = 0°$, $I = 0.0122$ and $\mathbf{\Omega} = 18\,000$ rpm.

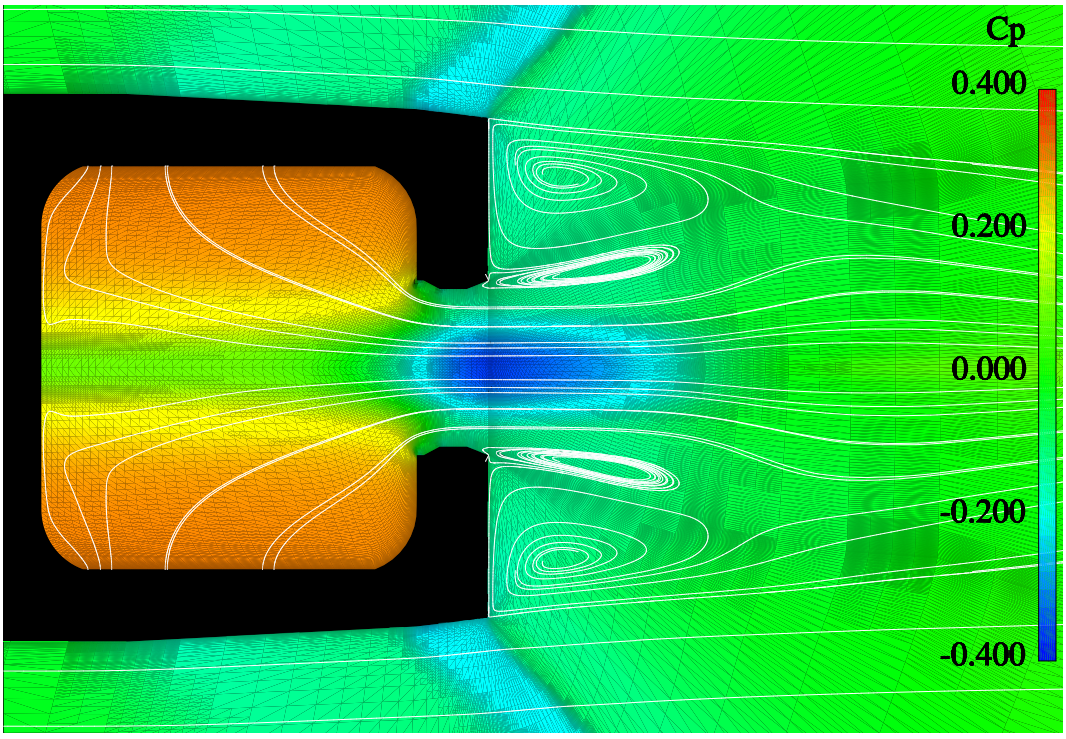

Fig. 5.37: The C_p distribution and streamlines according to the rotating and reacting flow field simulation. $Ma_\infty = 1.2$, $Re_D = 1.4 \cdot 10^6$, $\alpha = 0°$, $I = 0.0122$ and $\mathbf{\Omega} = 18\,000$ rpm.

The reaction rate is highest at the outer edge of the secondary recirculation zone, just as in the non-rotating flow case.

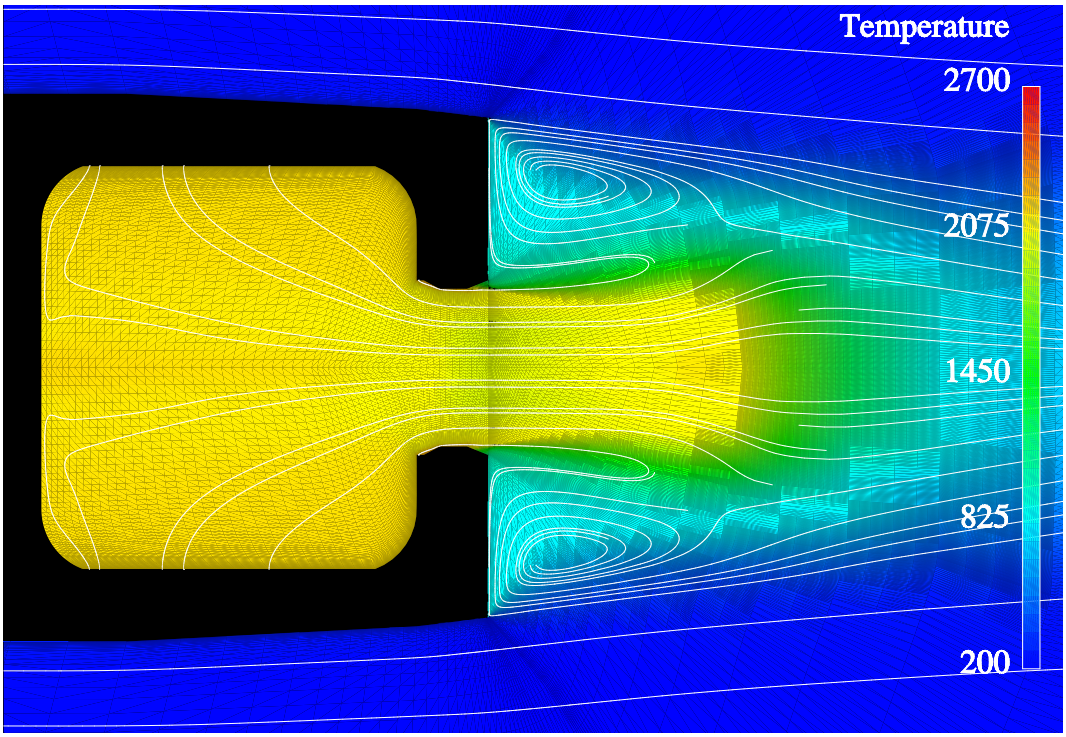

Fig. 5.38: The temperature distribution [K] and streamlines according to the rotating and inert flow field simulation. $Ma_\infty = 1.2$, $Re_D = 1.4 \cdot 10^6$, $\alpha = 0°$, $I = 0.0122$ and $\mathbf{\Omega} = 18\,000$ rpm.

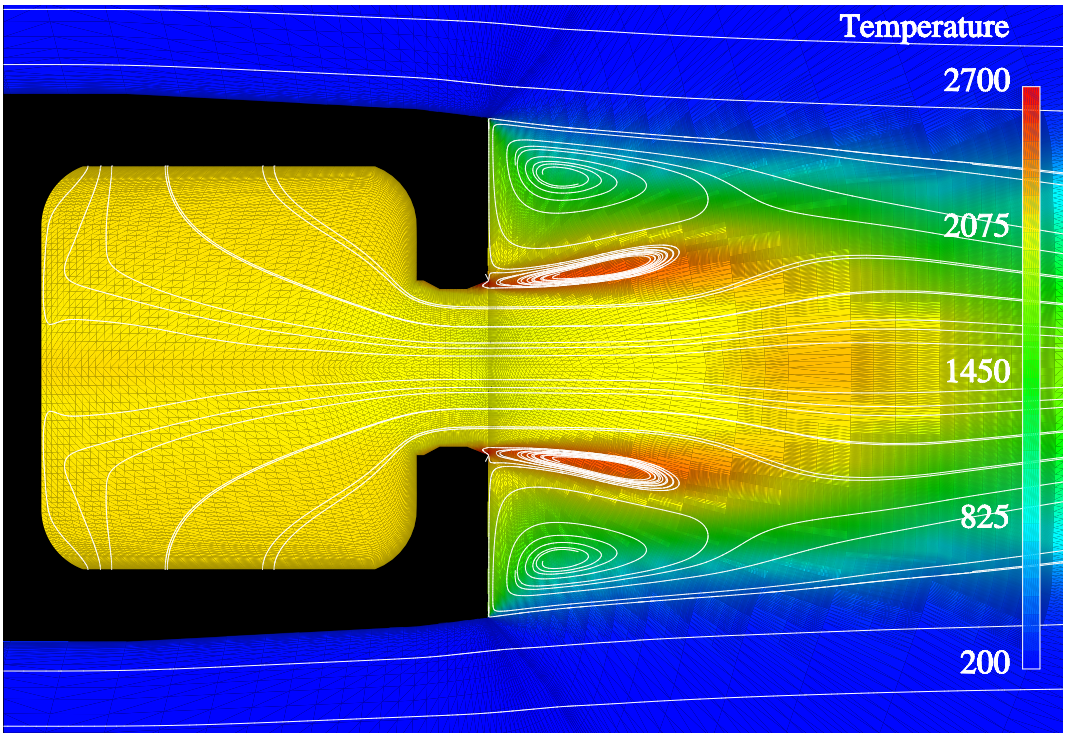

Fig. 5.39: The temperature distribution [K] and streamlines according to the rotating and reacting flow field simulation. $Ma_\infty = 1.2$, $Re_D = 1.4 \cdot 10^6$, $\alpha = 0°$, $I = 0.0122$ and $\mathbf{\Omega} = 18\,000$ rpm.

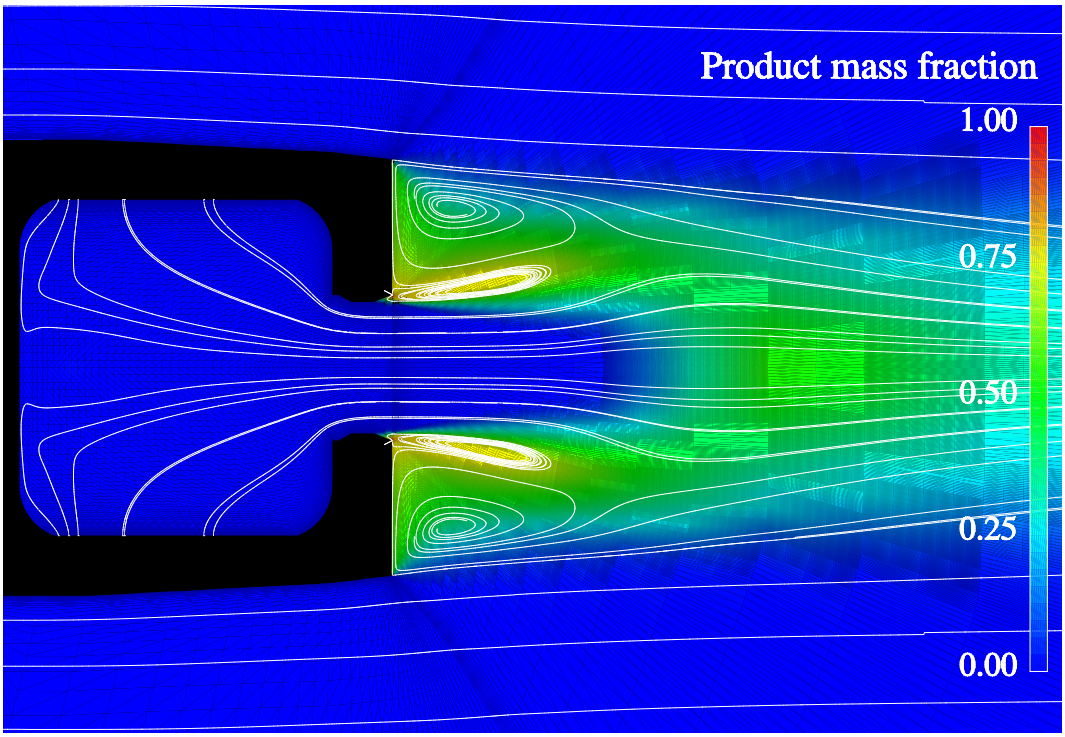

Fig. 5.40: The reaction product mass fraction ϕ_{pr} distribution and streamlines. $Ma_\infty = 1.2$, $Re_D = 1.4 \cdot 10^6$, $\alpha = 0°$, $I = 0.0122$ and $\boldsymbol{\Omega} = 18\,000$ rpm.

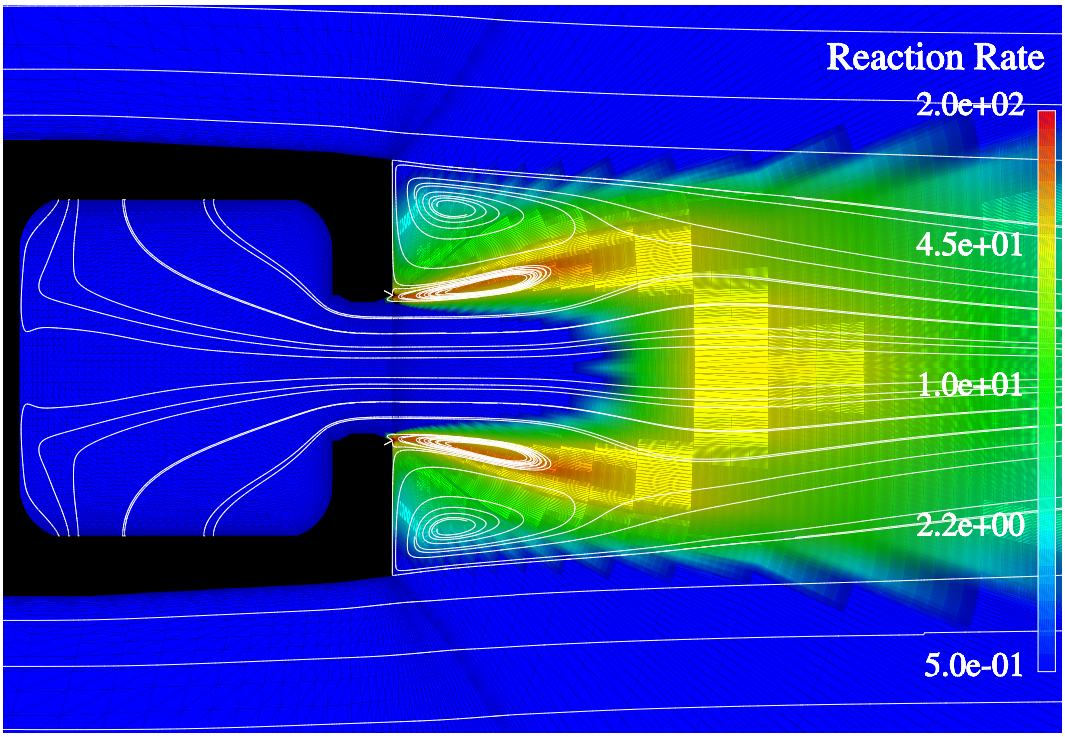

Fig. 5.41: The reaction rate Q_{pr} distribution [kg/(m^{3}s)] and streamlines. $Ma_\infty = 1.2$, $Re_D = 1.4 \cdot 10^6$, $\alpha = 0°$, $I = 0.0122$ and $\boldsymbol{\Omega} = 18\,000$ rpm.

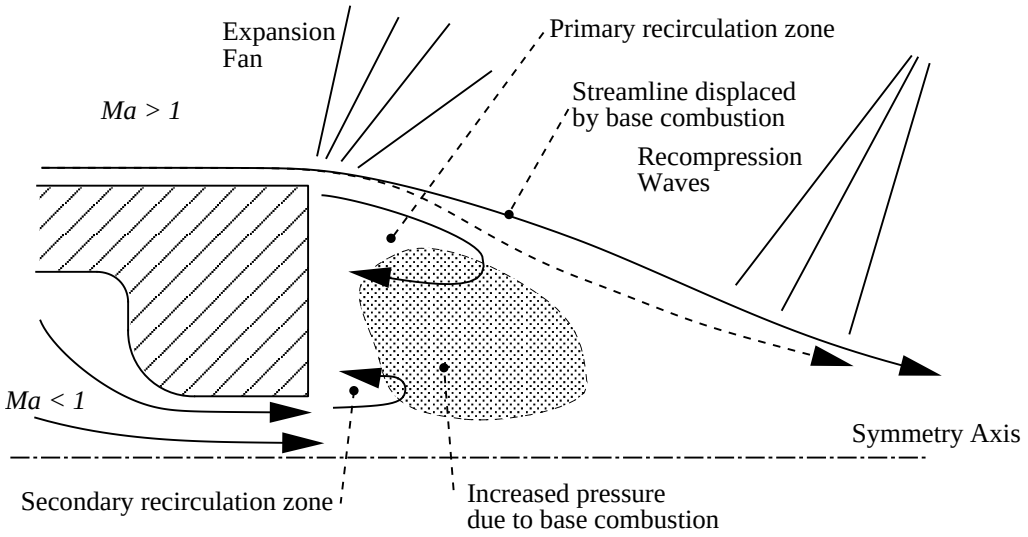

Fig. 5.42: The basic effects caused by base combustion on the flow field behind the base of a base-bleed projectile.

5.3 Discussion of the Results

The results presented demonstrate how the reactions caused by the fuel-rich propellant produce a significant reduction in the aerodynamic drag of a base-bleed projectile. This conclusion is supported by the experiments of Ding *et al.* [8], and the numerical simulations of Gibeling and Buggeln [12] and Nietubicz and Gibeling [13]. The excellent agreement with test firings obtained in the current work demonstrates that a simple reaction model is sufficient to produce the main effects of base combustion.

The essential factor leading to the advantages gained by utilizing a fuel-rich propellant is the location of where the final combustion takes place. The base combustion increases the pressure behind the base of the projectile, which decreases the base drag and slightly displaces the streamlines coming from upstream of the base corner. This situation is illustrated in Figure 5.42. By delaying a part of the combustion of the propellant the pressure outside the unit increases, which is seen as a direct decrease in the base drag. According to Figures 5.13 and 5.15, as well as Figures 5.35 and 5.37, this is precisely what happens, since the base combustion takes place in the recirculation zone right behind the base surface.

The validity of the predicted reaction rates cannot be directly evaluated due to the lack of a global reaction rate equation. However, since the combustion of carbon monoxide is one of the reactions present in the current problem, the global rate equation for the combustion of CO [28] could be used as a check for the figures obtained with the EBU model. Employing mass fraction values taken from the high reaction rate regions, an estimate for the rate of consumption of carbon monoxide $\mathrm{RR_{CO}}$ is obtained. Based on the rates obtained from reaction kinetics and the rates from the EBU model, we can define time-scales based on reaction kinetics t_{chem} and the EBU model t_{EBU} as

$$t_{\mathrm{chem}} = -\frac{\mathrm{RR_{CO}}}{\rho_{\mathrm{CO}}} \qquad t_{\mathrm{EBU}} = -\frac{Q_{\mathrm{fu}}}{\rho_{\mathrm{fu}}} \tag{5.7}$$

These figures give a crude estimate for the time required for the reactions to complete. With the data from the rotating projectile simulations with reacting base bleed, the time-scales defined by Eq. (5.7) obtained values of $t_{\mathrm{chem}} \approx 2 \cdot 10^{-4}$ s and $t_{\mathrm{EBU}} \approx 1 \cdot 10^{-4}$ s, respectively. Since these figures are of the same order of magnitude, there is hope that the EBU model does not dramatically overestimate the reaction rate anywhere in the flow field, which gives confidence to the whole solution.

For the flows with base bleed, rotation of the projectile introduces one fundamental difference. Because the bled gas has a tangential velocity component equal to the tangential velocity of the surface of the base-bleed unit, the flow out from the nozzle of the base-bleed unit has a large swirl angle. This is a consequence of the conservation of angular momentum, which, for a 2-D analysis ignoring viscosity, gives

$$V_t\, r = \text{constant} \tag{5.8}$$

where V_t is the tangential velocity and r is the distance to the axis of rotation. On the other hand, in a streamline-based coordinate system, the momentum equation normal to the streamline [31] states

$$\frac{\partial p}{\partial n} = \rho \frac{V^2}{R} \tag{5.9}$$

where R is the local radius of curvature of the streamline, and V is the velocity magnitude. Therefore, a radial pressure gradient is built up inside the base-bleed unit to maintain the balance in the radial direction. When the flow exits the unit, however, there is no mechanism to maintain a matching pressure gradient in the radial direction, and as a consequence, the jet is spread out in the radial direction very quickly. This, of course, has an effect on the properties of the flow field behind the base of the projectile.

The pressure gradient inside the unit has an effect on the detailed operation of the base-bleed unit, since the reaction rate of the propellant depends on the surface pressure. Based on Eq. (5.1) and the C_p values obtained from the simulations, the reaction rate of the propellant is underestimated by 10% with the non-rotating projectile, and by 15% with the rotating projectile. Therefore, for very detailed modelling, the boundary condition could be defined dynamically employing the known reaction rate of the propellant as a function of pressure from Eq. (5.1). This, however, is left for future work.

Rotation, on the other hand, does not seem to have too much of an influence on the integrated drag force of a projectile, but from a fluid dynamic point of view, it has a tremendous effect on the flow properties. The rotation-augmented mixing of the base-bleed jet changes the flow pattern behind the base of the projectile, and the details of the turbulence predictions are very different, but the changes in the pressure distribution are seen to be quite small.

All the present simulations share a weakness in that the time-averaged flow is assumed and forced to remain axially symmetric. This is probably a good assumption upstream of the base corner, but from that point on the wake flow is separated turbulent shear flow, which in reality is hardly axisymmetric. Fortunately, based on the good agreement with the test firings, it seems that this modelling constraint does not spoil the results.

As indicated by Table 5.1, three of the conducted simulations had to be carried out employing time-accurate time-integration. Only one of those three, however, produced a time-dependent solution — the rotating projectile with reactive base bleed. Fortunately, the amplitude of the oscillation of C_D was only 0.26% of the average value of C_D, and therefore, the results presented in this work are taken from the time of finishing the simulations.

The reason for the need to employ time-accurate time-integration in the two stationary cases is not completely clear. Ying *et al.* [64] reported similar behaviour when simulating multi-element airfoils under high-lift conditions, and they concluded that the oscillations seen in the "steady-state" simulations do not represent the true numerical simulations. In the present case, the oscillations seen in the "steady-state" simulations are probably caused by the employed convergence acceleration methods like local time-stepping and the multigrid scheme. They produce artificial unsteady phenomena, which are damped by the time-accurate scheme. On the other hand, time-accurate simulations with time-averaged equations are somewhat questionable, and contain some risks, as pointed out in Refs. [57, 64], and previously in this text.

6 Conclusions

The flow field near a supersonic base-bleed projectile was investigated in this work. In order to model the reactions associated with fuel-rich solid propellant combustion of the base-bleed unit, an eddy breakup model for the reactions was implemented into the employed solver, and tested with a suitable test case. The model was originally tuned for the $k-\epsilon$ model, and in this work it was also employed with the $k-\omega$ model. The $k-\omega$ realization was validated, but based on the conducted tests it is not possible to determine how the model should be fine-tuned. This is left for future work.

While simulating the flow field inside the base-bleed unit, the previous standard method of specifying the boundary conditions at an inlet had to be revisited. The enchanced method directly specifies the boundary flux instead of the boundary values, and thus stabilizes the employed solution method. Also, a generalized fast method of specifying the inviscid fluxes in the third computational direction allows the 3-D solver to be efficiently employed for 2-D and axisymmetric simulations. This facilitates a relatively fast validation against a purely 2-D solver.

The main new discovery of this work is the dramatic effect the chemical reactions have on the aerodynamic drag of a base-bleed projectile. The drag reduction is more than doubled by the final combustion of the partially burned fuel-rich propellant, and the drag predictions based on the simulations employing the reaction model agree extremely well with the radar measurements from test firings. The rotation, on the other hand, is seen to cause qualitatively large differences in the flow field, but those effects are hardly seen in the integrated drag force. Another conclusion from this work is that a simple reaction model like the eddy breakup model is sufficient to capture the main fluid dynamic effects of base combustion.

The details of the flow field at the exit of the base-bleed unit are hard, if not impossible, to measure under operational conditions, when the projectile rotates. The simulations of this work provide detailed information of the flow conditions in this region, thus facilitating further analysis of the flow physics. As it turned out in the simulations, the flow field in the exit nozzle of the base-bleed unit is unsteady, but the resulting amplitude of the drag oscillation is small in comparison with the mean value.

Bibliography

[1] Jubaraj Sahu, Charles J. Nietubicz, and Joseph L. Steger. Navier–Stokes Computations of Projectile Base Flow with and without Mass Injection. *AIAA Journal*, Vol. 23, No. 9, pp. 1348–1355, Sep 1985.

[2] Jubaraj Sahu and James E. Danberg. Navier–Stokes Computations of Transonic Flows with a Two-Equation Turbulence Model. *AIAA Journal*, Vol. 24, No. 11, pp. 1744–1751, Nov 1986.

[3] Jubaraj Sahu. Numerical Computations of Transonic Critical Aerodynamic Behavior. *AIAA Journal*, Vol. 28, No. 5, pp. 807–816, May 1990.

[4] Jubaraj Sahu and Charles J. Nietubicz. Application of Chimera Technique to Projectiles in Relative Motion. *Journal of Spacecraft and Rockets*, Vol. 32, No. 5, pp. 795–800, Sep-Oct 1995.

[5] Jubaraj Sahu and Karen R. Heavey. Numerical Investigation of Supersonic Base Flow with Base Bleed. *Journal of Spacecraft and Rockets*, Vol. 34, No. 1, pp. 62–69, Jan-Feb 1997.

[6] Michael J. Nusca. Numerical Simulation of Gas Dynamics and Combustion for 120-mm Ram Accelerator. In Michael J. Murphy and Joseph E. Backofen, editors, *Proceedings of the 14th International Symposium on Ballistics*, volume 1, pp. 261–272, Québec, Sep 1993. ISBN 0–9618156–9–8.

[7] Michael J. Nusca and David L. Kruczynski. Reacting Flow Simulation for a Large-Scale Ram Accelerator. *Journal of Propulsion and Power*, Vol. 12, No. 1, pp. 61–69, Jan-Feb 1996.

[8] Zesheng Ding, Shaosong Chen, Yafei Liu, Rong Luo, and Jingyuan Li. Wind Tunnel Study of Aerodynamic Characteristics of Base Combustion. *Journal of Propulsion and Power*, Vol. 8, No. 3, pp. 630–634, May-June 1992.

[9] Tarun Mathur and J. Craig Dutton. Base-Bleed Experiments with a Cylindrical Afterbody in Supersonic Flow. *Journal of Spacecraft and Rockets*, Vol. 33, No. 1, pp. 30–37, Jan-Feb 1996.

[10] Jan-Kaung Fu and Shen-Min Liang. Drag Reduction for Turbulent Flow over a Projectile: Part I. *Journal of Spacecraft and Rockets*, Vol. 31, No. 1, pp. 85–92, Jan-Feb 1994.

[11] J.C. Dutton, J.L. Herrin, M.J. Molezzi, T. Mathur, and K.M. Smith. Recent Progress on High-Speed Separated Base Flows. In *33rd Aerospace Sciences Meeting and Exhibit*, Reno, NV, Jan 1995. AIAA Paper 95-0472.

[12] Howard J. Gibeling and Richard C. Buggeln. Reacting Flow Models for Navier–Stokes Analysis of Projectile Base Combustion. In *27th Joint Propulsion Conference (AIAA / SAE / ASME / ASEE)*, Sacramento, CA, Jun 1991. AIAA Paper 91–2077.

[13] Charles J. Nietubicz and Howard J. Gibeling. Navier–Stokes Computations for a Reacting, M864 Base Bleed Projectile. In *31st Aerospace Sciences Meeting*, Reno, NV, Jan 1993. AIAA Paper 93–0504.

[14] Timo Siikonen and Jaakko Hoffren. Multigrid Solution Method for the Euler Equations. Report A-10, Helsinki University of Technology, Laboratory of Aerodynamics, 1989. ISBN 951–754–766–8.

[15] Timo Siikonen and Jaakko Hoffren. Solution of the Thin-Layer Navier–Stokes Equations for Laminar Transonic Flow. Report A-11, Helsinki University of Technology, Laboratory of Aerodynamics, 1989. ISBN 951–754–855–9.

[16] Jaakko Hoffren, Timo Siikonen, and Seppo Laine. Conservative Multiblock Navier–Stokes Solver for Arbitrarily Deforming Geometries. *Journal of Aircraft*, Vol. 32, No. 6, pp. 1342–1350, Nov-Dec 1995.

[17] Timo Siikonen. An Application of Roe's Flux-Difference Splitting for the $k - \epsilon$ Turbulence Model. *International Journal for Numerical Methods in Fluids*, Vol. 21, pp. 1017–1039, 1995.

[18] Petri Kaurinkoski and Antti Hellsten. Numerical Simulation of a Supersonic Base Bleed Projectile with Improved Turbulence Modelling. *Journal of Spacecraft and Rockets*, Vol. 35, No. 5, pp. 606–611, Sept-Oct 1998.

[19] Petri Kaurinkoski and Antti Hellsten. FINFLO: the Parallel Multi-Block Flow Solver. Report A-17, Helsinki University of Technology, Laboratory of Aerodynamics, 1998. ISBN 951–22–3940–X.

[20] Timo Sailaranta, Petri Kaurinkoski, Timo Siikonen, and Seppo Laine. Navier–Stokes Simulations for Finned Projectiles. In *Proceedings of the 14th International Symposium on Ballistics*, volume 1, pp. 627–636, Québec, Sep 1993. ISBN 0–9618156–9–8.

[21] Petri Kaurinkoski, Esa Salminen, and Timo Siikonen. Computation of Turbulent Flow over Finned Projectiles. In *1994 AIAA Atmospheric Flight Mechanics Conference*, pp. 378–387, Scottsdale, Arizona, Aug 1994. AIAA Paper 94-3502-CP.

[22] Petri Kaurinkoski. Computation of the Flow of Thermally Perfect Gas Past a Supersonic Projectile with Base Bleed. In *1996 AIAA Atmospheric Flight Mechanics Conference*, pp. 725–734, San Diego, California, Jul 1996. AIAA Paper 96-3451-CP.

[23] Bjørn F. Magnussen and Bjørn H. Hjertager. On Mathematical Modeling of Turbulent Combustion with Special Emphasis on Soot Formation and Combustion. In *16th Symposium (International) on Combustion*, pp. 719–729, Pittsburgh, Pennsylvania, Aug 1976. The Combustion Institute.

[24] D. Brian Spalding. Mixing and Chemical Reactions in Steady Confined Turbulent Flames. In *13th Symposium (International) on Combustion*, pp. 649–657, Pittsburgh, Pennsylvania, 1971. The Combustion Institute.

[25] P.A. Libby and F.A. Williams, editors. *Turbulent reacting flows*, volume 44 of *Topics in Applied Physics*. Springer-Verlag, Berlin, 1980.

[26] L.J.S. Bradbury, F. Durst, B.E. Launder, F.W. Schmidt, and J.H. Whitelaw, editors. *Turbulent Shear Flows 4*. Springer-Verlag, 1983.

[27] Kenneth K. Kuo. *Principles of Combustion*. John Wiley & Sons, Inc., New York, 1986. ISBN 0–471–62605–8.

[28] Lars Kjäldman. *Numerical Simulation of Combustion and Nitrogen Pollutants in Furnaces*. PhD thesis, Helsinki University of Technology, Technical Research Centre of Finland, Espoo, Dec 1993.

[29] S.M. Correa and A. Gulati. Measurements and Modelling of a Bluff Body Stabilized Flame. *Combustion and Flame*, Vol. 89, No. 2, pp. 195–213, May 1992.

[30] Inge R. Gran, Ivar S. Ertesvåg, and Bjørn F. Magnussen. Influence of Turbulence Modelling on Predictions of Turbulent Combustion. *AIAA Journal*, Vol. 35, No. 1, pp. 106–110, Jan 1997.

[31] John D. Anderson, Jr. *Hypersonic and High Temperature Gas Dynamics*. McGraw–Hill Book Co., New York, 1989. ISBN 0–07–001671–2.

[32] Hermann Schlichting. *Boundary Layer Theory*. McGraw–Hill Book Co., New York, 7th edition, 1979. ISBN 0–07–055334–3.

[33] Ching J. Chen. *Fundamentals of Turbulence Modeling*. Taylor & Francis, 1998. ISBN 1–56032–405–8.

[34] David C. Wilcox. *Turbulence Modeling for CFD*. DCW Industries, Inc., La Canada, 2 edition, 1998. ISBN 0–9636051–5–1.

[35] Frank M. White. *Viscous Fluid Flow*. McGraw–Hill Book Co., New York, 2nd edition, 1991. ISBN 0–07–069712–4.

[36] Kuei-Yuan Chien. Predictions of Channel and Boundary-Layer Flows with a Low-Reynods-Number Turbulence Model. *AIAA Journal*, Vol. 20, No. 1, pp. 33–38, Jan 1982.

[37] Florian R. Menter. Zonal Two Equation $k-\omega$ Turbulence Models for Aerodynamic Flows. In *24th AIAA Fluid Dynamics Conference*, Orlando, Florida, Jul 1993. AIAA Paper 93-2906-CP.

[38] Florian R. Menter. Two-Equation Eddy-Viscosity Turbulence Models for Engineering Applications. *AIAA Journal*, Vol. 32, pp. 1598–1605, Aug 1994.

[39] D.C Wilcox. Reassesment of the Scale-Determining Equation for Advanced Turbulence Models. *AIAA Journal*, Vol. 26, No. 11, pp. 1299–1310, November 1988.

[40] Antti Hellsten and Seppo Laine. Extension of the $k-\omega$ Shear-Stress Transport Turbulence Model for Rough-Wall Flows. *AIAA Journal*, Vol. 36, No. 9, pp. 1728–1729, Sep 1998.

[41] Antti Hellsten. On the Solid-Wall Boundary Condition of ω in the $k-\omega$-Type Turbulence Models. Report B-50, Helsinki University of Technology, Laboratory of Aerodynamics, 1998. ISBN 951–22–4005–X.

[42] Antti Hellsten. Some Improvements in Menter's $k-\omega$ SST Turbulence Model. In *29th AIAA Fluid Dynamics Conference*, Albuquerque, New Mexico, Jun 1998. AIAA Paper 98-2554-CP.

[43] M.A. Leschziner. Weaknesses of Eddy-Viscosity Models. In T. Craft, F.S. Lien, H. Iacovides, M.A. Leschziner, J.J. McGuirk, and G. Scheuerer, editors, *Turbulence Modelling for CFD Applications — Introductory*. UMIST Department of Mechanical Engineering, Manchester, Sep 1996.

[44] B.S. Baldwin and H. Lomax. Thin Layer Approximation and Algebraic Model for Separated Turbulent Flows, Jan 1978. AIAA Paper 78-257.

[45] H.W. Stock and W. Haase. Determination of Length Scales in Algebraic Turbulence Models for Navier–Stokes Methods. *AIAA Journal*, Vol. 27, No. 1, pp. 5–14, Jan 1989.

[46] Ottmar Knacke, Oswald Kubaschewski, and Klaus Hesselmann. *Thermochemical Properties of Inorganic Substances*. Springer-Verlag, Berlin, 2nd edition, 1991. ISBN 3–540–54014–8.

[47] P.L. Roe. Approximate Riemann Solvers, Parameter Vectors, and Difference Schemes. *Journal of Computational Physics*, Vol. 43, pp. 357–372, 1981.

[48] Timo Siikonen and Huachen Pan. Application of Roe's Method for the Simulation of Viscous Flow in Turbomachinery. In Ch. Hirsch et al., editor, *Proceedings of the first European Computational Fluid Dynamics Conference*, pp. 635–641, Brussels, Belgium, Sep 1992. Elsevier Science Publishers B.V.

[49] Eero-Matti Salonen. *Dynamiikka*. Otakustantamo, Espoo, 1980. ISBN 951-671-215-0, (In Finnish).

[50] Petri Kaurinkoski. *Numerical Determination of the Flow of an Arbitrary Mixture of Gases*. Licentiate's thesis, Helsinki University of Technology, Dec 1995.

[51] Timo Siikonen. A Three-Dimensional Multigrid Algorithm for the Euler and the Thin-Layer Navier–Stokes Equations. Report A-12, Helsinki University of Technology, Laboratory of Aerodynamics, 1991. ISBN 951–22–0601–3.

[52] Petri Kaurinkoski and Timo Siikonen. Calculation of Transonic Laminar and Turbulent Flow Past a Delta Wing. Report A-13, Helsinki University of Technology, Laboratory of Aerodynamics, 1992. ISBN 951–22–1273–0.

[53] C.K. Lombard, J. Bardina, E. Venkatapathy, and J. Oliger. Multi-Dimensional Formulation of CSCM — An Upwind Flux Difference Eigenvector Split Method for the Compressible Navier–Stokes Equations. In *6th AIAA Computational Fluid Dynamics Conference*, pp. 649–664, Danvers, Massachusetts, Jul 1983. AIAA Paper 83-1895-CP.

[54] Antony Jameson and Seokkwan Yoon. Multigrid Solution of the Euler Equations Using Implicit Schemes. *AIAA Journal*, Vol. 24, No. 11, pp. 1737–1743, 1986.

[55] Timo Siikonen, Jaakko Hoffren, and Seppo Laine. A Multigrid LU Factorization Scheme for the Thin-Layer Navier–Stokes Equations. In *Proceedings of the 17th ICAS Congress*, pp. 2023–2034, Stockholm, Sep 1990. ICAS Paper 90-6.10.3.

[56] Jaakko Hoffren. Time-Accurate Schemes for a Multi-Block Navier–Stokes Solver. Report A-14, Helsinki University of Technology, Laboratory of Aerodynamics, 1992. ISBN 951–22–1350–8.

[57] Petri Kaurinkoski, Petteri Heino, and Antti Hellsten. Implementation of a Time-Accurate Time-Integration Scheme to the FINFLO Flow Solver. Report A-18, Helsinki University of Technology, 1999. ISBN 951–22–4550–7.

[58] P. Vähäkangas and T. Heininen. PVY-ruudin palolämpötilan määrittäminen HSC-ohjelmalla, (Determination of the Flame Temperature of the Base Bleed Propellant using the HSC-program). Technical Report 1570/Hi II, Puolustusvoimien Tutkimuskeskus, (Defence Forces Research Institute of Technology), Ylöjärvi, Sep 1995. (In Finnish, unpublished, classified).

[59] P. Vähäkangas and T. Heininen. PVY-ruudin palokaasujen sekoittuminen ilmaan, (Mixing of the Exhaust Gases of the Base Bleed Unit with Air). Technical Report 683/Hi II, Puolustusvoimien Tutkimuskeskus, (Defence Forces Research Institute of Technology), Ylöjärvi, Apr 1996. (In Finnish, unpublished, classified).

[60] R.W. Bilger. *Turbulent Flows with Nonpremixed Reactants*, volume 44 of *Topics In Applied Physics*, chapter 3, pp. 65–113. Springer-Verlag, Heidelberg, Germany, 1980.

[61] S.M. Correa and S.B. Pope. Comparison of a Monte Carlo PDF/Finite-Volume Mean Flow Model with Bluff–Body Raman Data. In *24th Symposium (International) on Combustion*, pp. 279–285, Pittsburgh, Pennsylvania, 1992. The Combustion Institute.

[62] Puolustusvoimien Materiaalilaitoksen Esikunta, (Defence Materiel Establishment of the Finnish Defence Forces). *Koeammuntapöytäkirja 197/98, (Notes on Testfiring 197/98)*, Nov 1998. (In Finnish, unpublished, classified).

[63] Paavo Raerinne and Tapio Heininen. TPE-pohjaisen PVY-ruudin ominaisuuksia, (Properties of the TPE-Based Base Bleed Propellant). Technical report, Puolustusvoimien Tutkimuskeskus, (Defence Forces Research Institute of Technology), Ylöjärvi, Oct 1998. 1114/8.2/D/I, (In Finnish, unpublished, classified).

[64] Susan X. Ying, Frank W. Spaid, Catherine B. McGinley, and Christopher L. Rumsey. Investigation of Confluent Boundary Layers in High-Lift Flows. In *16th AIAA Applied Aerodynamics Conference*, Albuquerque, New Mexico, Jun 1998. AIAA Paper 98-2622.